Volume holographic pupils in ray, wave, statistical optics, and Wigner space

by

Se Baek Oh

Submitted to the Department of Mechanical Engineering
in partial fulfillment of the requirements for the degree of

Doctor of Philosophy

at the

MASSACHUSETTS INSTITUTE OF TECHNOLOGY

February 2009

Author ....
Department of Mechanical Engineering
January 9, 2009

Certified by ....
George Barbastathis
Associate Professor
Thesis Supervisor

Accepted by ....
David E. Hardt
Chairman, Department Committee on Graduate Students

Volume holographic pupils in ray, wave, statistical optics, and Wigner space

by

Se Baek Oh

Submitted to the Department of Mechanical Engineering
on January 9, 2009, in partial fulfillment of the
requirements for the degree of
Doctor of Philosophy

Abstract

This thesis explores various aspects of the volume holographic pupils to better understand and implement multi–dimensional imaging. A full description and applications of volume holographic pupils are presented in ray, wave, statistical optics, and Wigner space. Volume holograms have both a shift variant nature and multiplex capability, which can efficiently extract specific information of multi–dimensional objects by engineering imaging kernels with shift variant point spread functions and using post–processing.

Based on the k–sphere formulation, an efficient computation method of analyzing volume diffraction is developed. It is integrated with the ray tracing software ZEMAX® whose built–in analysis and optimization features provide a great versatility for analysis, design, and optimization of novel volume holographic imaging systems. For a plane wave reference hologram, the shape of the Bragg diffraction image is analyzed in detail, where the shape is a distorted ellipse.

The wave optics formulation of volume diffraction is revisited and further developed into statistical optics. The partially coherent response of a volume holographic imaging system is derived. Based on spatial coherence measurements, new passive binary depth detection is proposed, which is a special case of multi–dimensional imaging. Spatially incoherent two objects at two distinct depths are discriminated: focused objects in the foreground and defocused objects in the background. The passive detection is demonstrated for featureless uniform objects under quasi–monochromatic light by measuring mutual intensity with a volume holographic imager. By exploiting cross spectral density measurement, the passive binary depth detection is also demonstrated under white light illumination.

Finally, the Wigner distribution function for volume holographic pupils is introduced. The space–spatial frequency characteristics of volume holograms are analyzed with linear systems approach. Wigner representations of two volume holograms are examined: plane and spherical wave reference holograms. Then, various axial imaging systems, which measure the depth of objects from intensity images, are explored by the Wigner analysis. Two important conditions for axial imaging are established:

1) shift variant objects and 2) properly designed integration kernels. Based on these conditions, a shift variant imaging kernel is shown to be necessary for axial imaging.

Thesis Supervisor: George Barbastathis
Title: Associate Professor

Acknowledgments

My life at graduate school has been extraordinary; it took longer than I expected but it always has been fascinating, exciting, and enjoyable in many different ways. I have been fortunate to study at the best institutes with great colleagues and mentors. Not only my expertise on optics has been broadened and deepened but also I have learned many lessons and wisdom about life.

First and foremost, I would like to express my heartiest gratitude to my advisor Prof. George Barbastathis. He has taught many things: the importance of fundamental understanding of physics and the way of disassembling complicated problems without compromising. His deep insight, intuition on various subjects, and constant guidance have kept inspiring me. I really enjoyed all the discussions we had. I would also like to thank my thesis committee: Prof. Peter So, Prof. Ramesh Raskar, and Prof. Soohyun Kim at KAIST for their invaluable contribution to this work. Especially, Prof. Raskar introduced me interesting research in computer vision and I was very glad to work with him. Chapter 4 of this thesis could not have been done without his initial inspiration. Prof. Kim has always been a great support and shown me the passion for professional life.

I want to thank many people I have known and interacted at MIT, especially everyone in the 3D optical systems group: Pepe, Nick, Laura, Hyun Jin, Tony, Nader, Satoshi, Paul, Will, Wenyang, Kehan, Patrick, Lei, Aditya, and Martin. They helped me in all aspect of my academic life at MIT. I also want to thank many friends, specially members of KGSAME, friends at Westgate and TCC, and colleagues in MSD Lab at KAIST.

Most importantly, I would like to thank my family. My beloved wife, Sun Ok has been my best friend for years and my only lifelong companion. With her love, dedication, and sacrifice, I was able to finish my Ph.D. work. Also, I am very thankful for my first daughter, Allison Hyein, for her patience to wait till my thesis defense to see the world. Finally, I'd like to show my great appreciation to my parents, my brother, and parents in law for their constant love, support, and encouragement.

Contents

List of Figures

List of Tables

Chapter 1

Introduction

In the real world, three–dimensional scenes are observed through imaging systems. If the wavelength of light is considered, natural scenes should be described in 4–dimensional space. To obtain this multi–dimensional information, the imaging process should inevitably include multi–dimensional measurements. However, many traditional imaging systems such as photographic cameras, microscopes, and telescopes use two–dimensional detectors, where the measurements are limited in their dimensionality due to a space–bandwidth product.

To measure multi–dimensional information with imaging systems of limited dimensionality, one could use shift variant imaging kernels as well as multiplexing techniques. While a shift variant imaging kernel is considered to be undesirable in traditional imaging process, it may extract specific information of a scene more efficiently because system responses can be tuned to be more sensitive to some features of a scene. Typically, multiplexing is implemented by multiple imaging kernels operating in parallel (e.g., extra cameras or holograms recorded by multiple exposures), where individual imaging kernels are modified to yield different responses for specific features of a scene. Hence, engineering these two features, shift variant and multiplexed imaging, would be extremely useful for achieving multi–dimensional imaging.

Another motivation for using the shift variant/multiplexed imaging approach is rapidly growing computational power. As demonstrated in wavefront–coding systems [1], engineering point spread functions and using computational post–processing provide greater functionalities such as defocus tolerance to imaging processes. Although the wavefront–coding system does not exactly use shift variant/multiplexed imaging approach, it suggests that computation becomes an essential part of the imaging process and would be more effective in shift variant/multiplexed imaging because more controls on imaging systems are available. A similar effort of using computational approaches has been used in different research areas such as computational photography [2] and computational imaging [3, 4].

Volume Holographic Imaging(VHI), i.e., imaging incorporated with volume holograms, is a shift variant as well as multiplexed imaging method. VHI encodes the multi–dimensional information of objects through Bragg diffraction; the captured information is properly decoded with post–processing. Raw images from VHI systems are not identical to the ones from traditional imaging systems, but the processed final outputs may contain more information. Moreover, the characteristics of the shift variant response and multiplexing can be controlled in various ways: e.g., different recording geometry, wavelength, and exposure times, etc., hence VHI provides more flexibility in engineering system responses. VHI is a convenient and effective method to implement shift variance/multiplexed imaging and to explore the multi–dimensional imaging process. In this thesis, we present a sequence of analysis frameworks of VHI responses, demonstrate how to achieve passive depth ranging with volume holograms based on spatial coherence measurements, and establish a better understanding of the multi–dimensional imaging process with Wigner analysis.

1.1 Fundamentals of volume holographic imaging

1.1.1 Volume holograms

Volume holograms are thick gratings whose axial extent is much longer than for thin gratings. They exhibit Bragg diffraction [5], which is very different than diffraction from a thin grating. Photorefractive crystals such as $LiNbO_3$, $BaTiO_3$, BSO, BGO, KTN, and SBN are often used, while photopolymers or other materials also can be

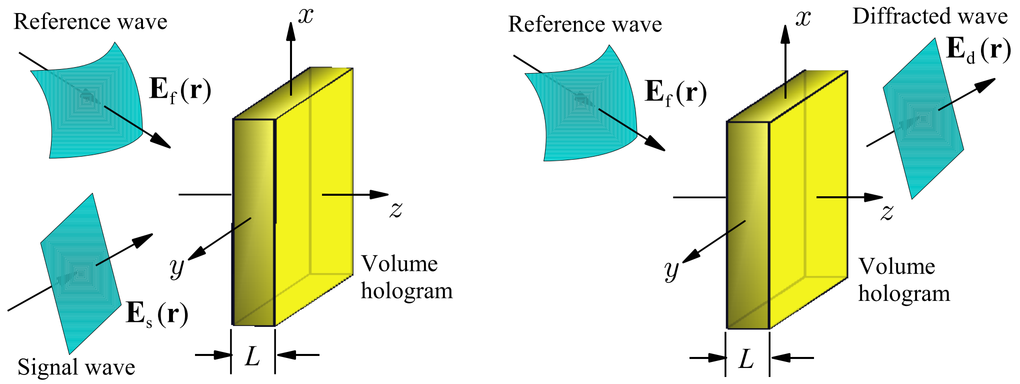

(a) recording

(b) probing

Figure 1-1: Recording and probing a volume hologram

used as long as a refractive index modulation can be introduced in them [6]. In photorefractive crystals, exposure to a modulated light wavefront in turn modulates the refractive index of the material. Generally, interference patterns from two or more mutually coherent light beams are constructed inside the material to create the refractive index modulation. This optical recoding method is relatively easy and flexible for changing the period of the phase modulation. By this recording process, the wavefront information of the interfered beams is stored as shown in Fig. 1-1(a). Typically, two–beam interference is used, where one beam is called a reference wave ($\mathbf{E}_\mathrm{r}$) and the other is called a signal wave ($\mathbf{E}_\mathrm{s}$). The refractive index modulation is proportional to

$$\Delta\epsilon(\mathbf{r}) \propto \mathbf{E}_\mathrm{f}^*(\mathbf{r})\mathbf{E}_\mathrm{s}(\mathbf{r}), \tag{1.1}$$

where $\mathbf{r}$ denotes the spatial coordinate [7]. After developing and fixing if necessary, the volume hologram becomes a *thick* phase grating.

The refractive index modulation generates volumetric diffraction when the volume hologram is exposed to a probe wavefront. If the probe wavefront is exactly identical to the reference wave, the diffraction efficiency reaches the maximum, where the entire probe wavefront satisfies the Bragg condition [5] as shown in Fig. 1-1(b). In the case of volume hologram recorded by the symmetric geometry as shown in 1-2(a), the Bragg condition states the relation between the period of the hologram, the wavelength, and

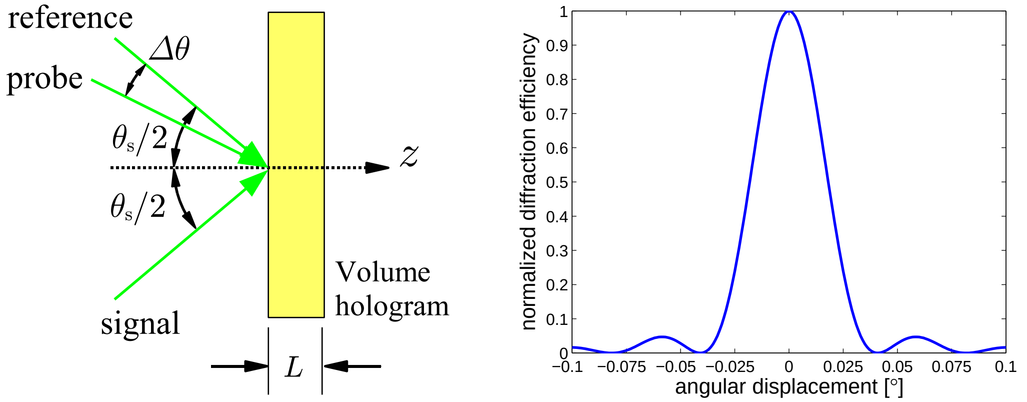

(a) Angular deviation of a probe beam

(b) Diffraction efficiency with respect to angle deviations

Figure 1-2: Angle Bragg selectivity. As $\Delta\theta$ deviates from θ, the Bragg diffraction varies as sinc^2 fashion. In (b), $\lambda = 488\,\mathrm{nm}$, $L = 1\,\mathrm{mm}$, and $\theta_\mathrm{s} = 40°$.

the angle of the reference/signal waves as

$$\Lambda = \frac{\lambda}{2L\sin(\theta_\mathrm{s}/2)}, \tag{1.2}$$

where Λ is the period of the refractive index modulation in the volume hologram, λ is the wavelength of the reference and signal waves, L is the thickness of the volume hologram, and θ_s is the angle between the reference and signal waves.

Volume holograms have enormous information storage/processing capacity. For this reason, they have been extensively applied to holographic data storage [8–11], optical interconnects [12], and artificial neural networks [13].

Angular selectivity

In the case of the plane wave reference hologram recorded by a symmetric geometry as shown in Fig. 1-2(a), if a probe wave deviates by $\Delta\theta$ with respect to the reference wave, then the diffraction efficiency changes as

$$\eta \sim \mathrm{sinc}^2\left(\frac{2L\Delta\theta\sin(\theta_\mathrm{s}/2)}{\lambda}\right), \tag{1.3}$$

where $\Delta\theta$ denotes the deviation angle of the probe beam with respect to θ_s. As the deviation increases, the Bragg diffraction decreases as shown in Fig. 1-2(b). At the first null of the sinc^2 function, the volume hologram does not diffract. This is called the angular Bragg selectivity, which is defined by

$$(\Delta\theta)_B = \frac{\lambda}{2L\sin(\theta_\mathrm{s}/2)}. \tag{1.4}$$

As the Bragg condition indicates, a similar relation occurs when the wavelength of a probe beam deviates from the wavelength of the reference wave. Hence, volume holograms strongly diffract by the specific probe beam that has a correct angle and wavelength relation.

Wavelength degeneracy

As the Bragg condition eq. (1.2) implies, the period of the refractive index modulation is determined by both the angle and wavelength. Deviation in either the angle or wavelength reduce the diffracted power, but if both angle and wavelength change in a way that satisfies the Bragg condition then the volume hologram still diffracts strongly. Equivalently, the identical interference period can be generated with different combinations of λ_f and θ_s as shown in Fig 1-3, which is termed wavelength degeneracy. Hence, light of different wavelengths can be Bragg matched simultaneously if they have the correct angles.

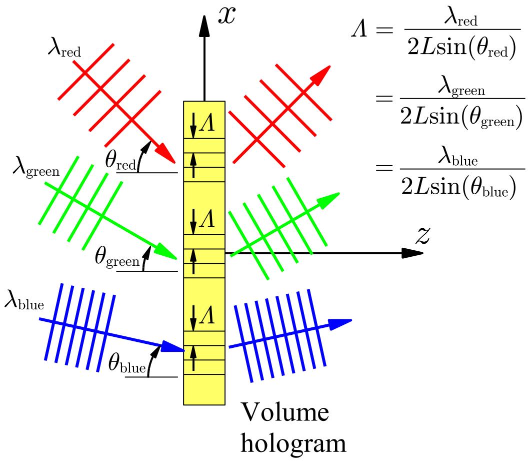

Figure 1-3: Wavelength degeneracy of a plane wave reference volume hologram

Multiplexing capability

Volume holograms exhibit multiplexing capability, in which multiple different wavefronts can be stored in a hologram. As shown in Fig. 1-4, during each exposure, different configurations can be used.

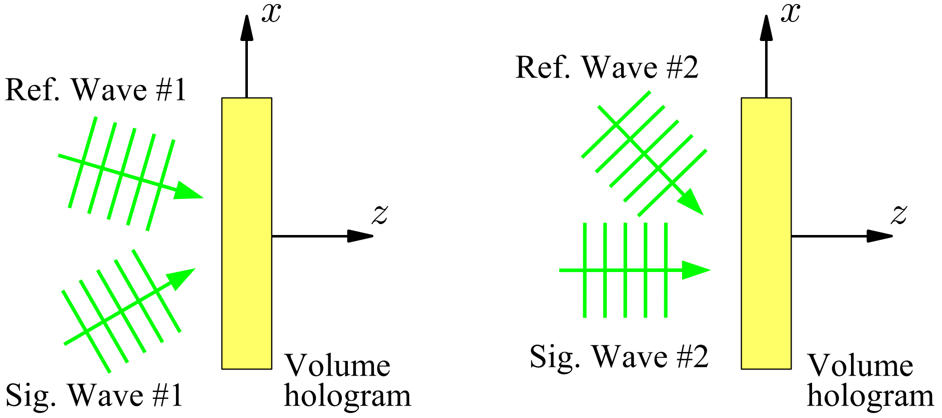

(a) first exposure (b) second exposure

Figure 1-4: Multiplexing of two volume holograms

To avoid crosstalk during the read out process, the angular separation between each configuration should be equal to integral multiples of the angular selectivity. The diffraction efficiency decreases as the number of multiplexed holograms increases as

$$\eta \propto \frac{(M\#)^2}{M^2}, \tag{1.5}$$

where $M\#$ (pronounced "M–number") depends on the properties of the holographic material and the optical system and M is the total number of multiplexed holograms. The typical values of $M\#$ are in the range of 0.1–10 [14].

1.1.2 Volume Holographic Imaging

Volume holographic imaging (VHI) is a newly developed multi-dimensional imaging technique utilizing wavefront information stored in volume holograms [7]. As shown in Fig. 1-5, VHI systems use the volume hologram as a 3D optical element. The strong shift variance and multiplexing capability produce special responses that conventional

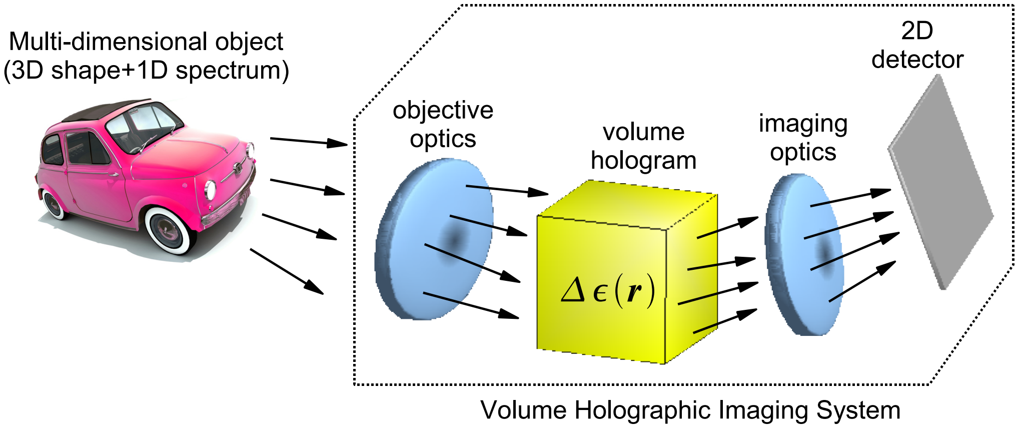

Figure 1-5: The concept of volume holographic imaging systems

imaging systems cannot easily achieve. The 3D spatial and spectral information is encoded by the Bragg selectivity and mapped onto photodetector arrays. Previous research has demonstrated that the responses of VHI systems can be engineered to achieve various novel imaging processes, which has found many applications [7, 15–25]. By utilizing strong angular/wavelength selectivity, depth selective and hyper–spectral imaging have been achieved [7, 16, 23]. Moreover, with multiplexed holograms, several imaging channels can be implemented simultaneously. This feature has been used for 3D imaging of fluorescent beads [17] and biological tissues [25]. In conjunction with conventional imaging platforms, various multi–dimensional imaging systems such as volume holographic telescopes and microscopes have been built and demonstrated [7, 15, 22].

To present the principle of the VHI, we explain how depth selective imaging is achieved in the 4–f VHI system reported in Ref. [7]. During the recording process, two mutually coherent plane waves construct interference fringes inside a volume hologram and create refractive index modulations. The reference wave is a collimated plane wave which originates from a point source, and the signal wave is also a plane wave but propagating with an angle of θ_s with respect to the optical axis as shown in Fig. 1-6(a). By attaching a collector lens and CCD camera behind the volume hologram, the whole system behaves as a depth selective imaging system for point objects. If a point object is located at the front focal plane of the system as shown

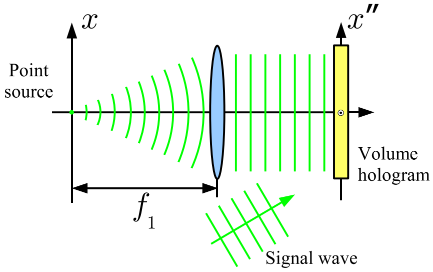

(a) Recording geometry

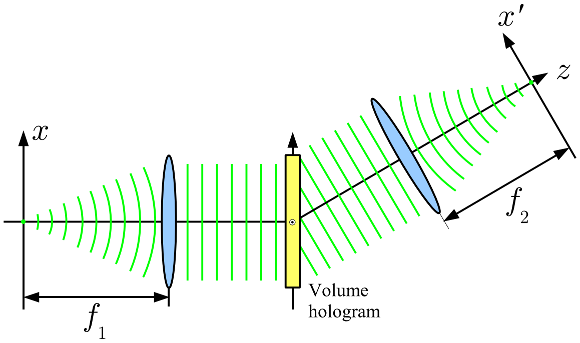

(b) Imaging of a focused point object

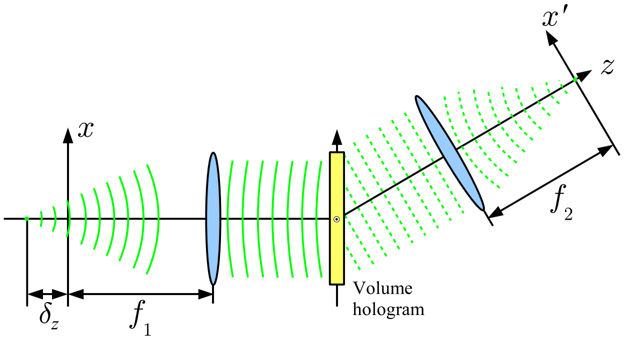

(c) Imaging of a defocused point object

Figure 1-6: Schematic of VHIs for depth selective imaging

in Fig. 1-6(b), then the wavefront from the point object is collimated by the lens and becomes completely identical to the reference wave, in which strong Bragg diffraction occurs. However, if the point object is defocused by δ_z as shown in Fig. 1-6(c), then the Bragg diffraction is significantly attenuated because the incoming wavefront on the volume hologram is not perfectly matched with the stored reference wave. Focused illumination emulates a point source on an object, the 3D profile is recovered with lateral and longitudinal scannings of either the system or the objects.

1.2 Outline of the thesis

This thesis explores different aspects of volume holographic pupils. In Chapter 2, two different frameworks of volumetric diffraction are presented: the k–sphere method and the Fourier optics method. The k–sphere method is a geometrical construction of the Bragg match/mismatch calculation. It is very simple and intuitive, which could be useful for analyzing even complicated volume holograms, e.g., holograms with shift variant grating vectors. To maximize the computation efficiency, the k–sphere method is integrated with the commercial ray tracing software suite ZEMAX®. This allows using various built–in analytical and optimization tools, which leads to better performance and efficient design of VHI systems. The k–sphere method is extended in 3D space and the Bragg diffraction images are examined in detail. Then, the Fourier optics formulation of volume diffraction is revisited. The difference of traditional and VHI systems are examined.

In Chapter 3, the previously derived VHI responses are further developed into statistical optics and the partially coherent response of VHI systems are analyzed. Then, a new passive depth detection method based on spatial coherence measurements is proposed. As the van Citter–Zernike theorem describes, for spatially incoherent light, the spatial coherence increases as propagation. An interferometric measurement system is cascaded to the volume holographic pupil. For quasi–monochromatic light, theoretical analysis and experimental verification are presented. To improve the depth resolving capability under broadband illumination, the cross spectral density measurements are implemented. Through a series of experiments, discrimination of uniform featureless objects at two different depths is demonstrated.

In Chapter 4, space–spatial frequency analysis, the Wigner distribution function is introduced for volume holograms and VHI systems. The basic concept and property of the Wigner distribution function are summarized. Using a linear systems approach, the Wigner representation of volume holograms and VHI systems are derived. Also the different behaviors of shift varian/invariant systems with defocus are investigated and two major conditions for implementing systems with axial imaging capability, i.e., ability to obtain depth information from captured images, are established.

In Chapter 5, this thesis is concluded by summarizing all topics. Advantages and limitations are discussed and future direction of research is presented.

Chapter 2

Volume diffraction framework for volume holographic pupils

In this chapter, two frameworks for volume diffraction are presented: ray and wave–optics formulations. The first one is called the k–sphere method, which computes the Bragg match/mismatch vector with geometrical constructions. The k–sphere method is implemented in the commercial ray tracing software suite ZEMAX®, which allows efficient simulation of volume diffraction. We examine the Bragg diffraction patterns on the image plane in more detail by using the k–sphere method .

The second framework for volume diffraction is based on Fourier optics analysis, which is reported in Ref. [26, 27]. The result is briefly revisited and discussed. This formulation will be extended into statistical optics in Chap. 3.

2.1 Geometrical construction for analysis of volume diffraction

2.1.1 Introduction

To design VHI systems, the Bragg diffraction from volume holograms should be analyzed. Analytical models of volume holograms have already been reported [7, 8, 27]. However, since they are based on wave optics, they are not straightforward for use in the design process. Also, if a volume hologram has shift variant imaging properties, analytical approaches become tedious and often fail to provide intuition. In this section, we describe a ray tracing implementation of volume hologram modeling. In modern optical system design, ray tracing software packages have become essential tools because they provide various analytical features and optimization routines, which makes the whole design process much more efficient and agile.

2.1.2 k–sphere formulation

A volume hologram is considered as a phase grating, but being significantly thicker than conventional diffraction gratings; it is subject to volumetric diffraction and shows strong wavefront selectivity when exposed to a probe beam. A mathematical model of volumetric diffraction has been derived from scalar diffraction theory and Born's first order approximation [14]. The k–sphere formulation is the geometrical representation of the previously derived model; it is often referred to the Ewald sphere and originates from a method used in crystallography and solid-state physics [28]. Figure 2-1 shows the concept of the k–sphere formulation. In this particular case, the volume hologram is assumed to be recorded by plane waves for simplicity.

The wavelengths of the recording and probe waves are denoted by λ_{f} and λ_{p}, respectively. Let $\mathbf{k}_{\mathrm{f}}$ and $\mathbf{k}_{\mathrm{s}}$ denote the reference and signal wavevectors, respectively ($|\mathbf{k}_{\mathrm{f}}| = |\mathbf{k}_{\mathrm{s}}| = 2\pi/\lambda_{\mathrm{f}}$), while $\mathbf{k}_{\mathrm{p}}$ denotes the probe wavevector ($|\mathbf{k}_{\mathrm{p}}| = 2\pi/\lambda_{\mathrm{p}}$). As shown in Fig. 2-1(a), the grating vector $\mathbf{K}_{\mathrm{g}}$ is obtained as

$$\mathbf{K}_{\mathrm{g}} = \mathbf{k}_{\mathrm{s}} - \mathbf{k}_{\mathrm{f}}. \tag{2.1}$$

To determine the diffracted field in the Bragg regime, the vector $\mathbf{k}_{\mathrm{p}} + \mathbf{K}_{\mathrm{g}}$ should be examined [8]. The direction of the wavevector $\mathbf{k}_{\mathrm{d}}$ of the diffracted field is specified by requiring that the lateral component of $\mathbf{k}_{\mathrm{d}}$ equals the lateral component of $\mathbf{k}_{\mathrm{p}} + \mathbf{K}_{\mathrm{g}}$, and that the tip of $\mathbf{k}_{\mathrm{d}}$ lies on the k–sphere (i.e., the condition for a propagating field);

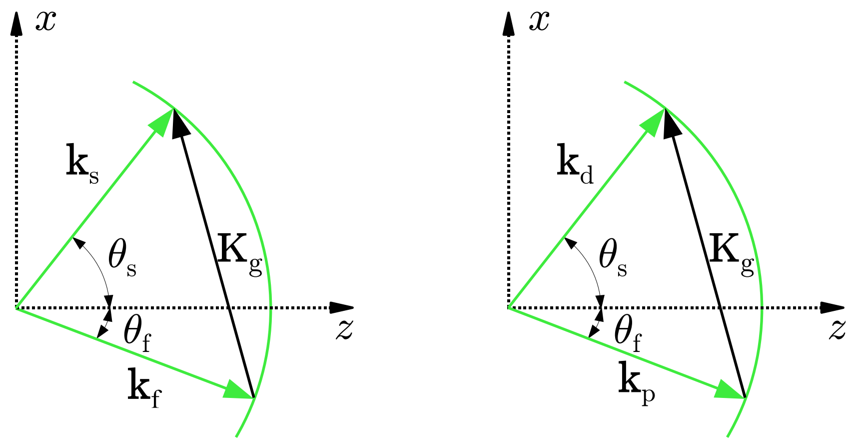

(a) Construction of the grating vector from the recording wave vectors

(b) Bragg matched reconstruction

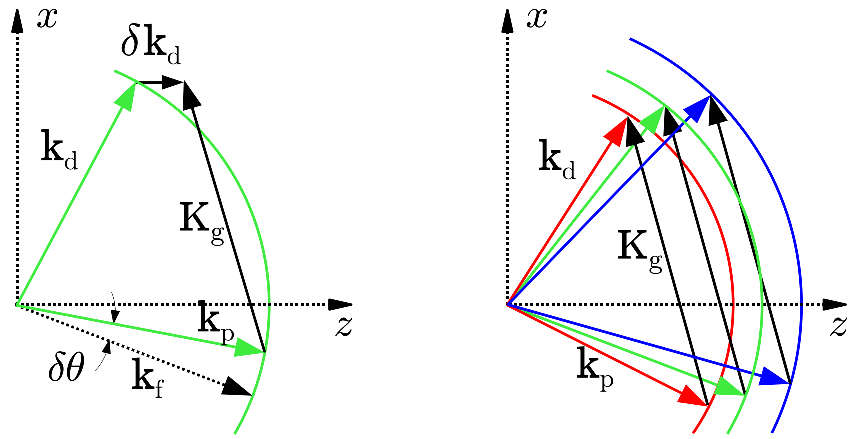

(c) Bragg mismatch

(d) Wavelength degeneracy

Figure 2-1: Geometric construction of volumetric diffraction using the k–sphere that is,

$$
\begin{aligned}
\mathbf{k}_{\mathrm{d}} \cdot \hat{\mathbf{x}} &= (\mathbf{k}_{\mathrm{p}} + \mathbf{K}_{\mathrm{g}}) \cdot \hat{\mathbf{x}}, & & (2.2)\\
\mathbf{k}_{\mathrm{d}} \cdot \hat{\mathbf{y}} &= (\mathbf{k}_{\mathrm{p}} + \mathbf{K}_{\mathrm{g}}) \cdot \hat{\mathbf{y}}, \qquad \text{and} & & (2.3)\\
|\mathbf{k}_{\mathrm{d}}| &= 2\pi/\lambda_{\mathrm{p}}. & & (2.4)
\end{aligned}
$$

These constraints are obtained assuming that the lateral size of the hologram is much larger than the hologram thickness. If $\mathbf{k}_{\mathrm{p}} + \mathbf{K}_{\mathrm{g}}$ satisfies the above conditions, then $\mathbf{k}_{\mathrm{d}} \equiv \mathbf{k}_{\mathrm{p}} + \mathbf{K}_{\mathrm{g}}$, and the probe is Bragg–matched as shown in Fig. 2-1(b). If the Bragg matching condition is not satisfied, $\mathbf{k}_{\mathrm{d}}$ is still obtained from eqs. (2.2)–(2.4) but the diffraction efficiency is decreased according to

$$\eta \propto \mathrm{sinc}^2\left(\frac{L(\mathbf{k}_{\mathrm{p}} + \mathbf{K}_{\mathrm{g}} - \mathbf{k}_{\mathrm{d}}) \cdot \hat{\mathbf{z}}}{2\pi}\right) = \mathrm{sinc}^2\left(\frac{L\delta\mathbf{k}_{\mathrm{d}} \cdot \hat{\mathbf{z}}}{2\pi}\right), \tag{2.5}$$

where L is the hologram thickness. The vector

$$\delta\mathbf{k}_{\mathrm{d}} \equiv \mathbf{k}_{\mathrm{p}} + \mathbf{K}_{\mathrm{g}} - \mathbf{k}_{\mathrm{d}} \tag{2.6}$$

is referred to as the Bragg mismatch vector; clearly, Bragg matching requires $\delta\mathbf{k}_{\mathrm{d}} = 0$, whereas if $\delta\mathbf{k}_{\mathrm{d}} \neq 0$ the diffraction efficiency is determined directly by the magnitude of $\delta\mathbf{k}_{\mathrm{d}}$ (Fig. 2-1(c)). It is evident from the geometrical construction that the Bragg condition can be fulfilled at an infinite number of combinations of probe beam wavevectors $\mathbf{k}_{\mathrm{p}}$ and probe wavelengths λ_{p}. The locus of the $\mathbf{k}_{\mathrm{p}}$ vector's tip as a function of λ_{p} constitutes the wavelength degeneracy curve of the volume hologram (Fig. 2-1(d)). It should be noted that the k–sphere formulation can be applied either to slanted ($\theta_{\mathrm{s}} \neq \theta_{\mathrm{f}}$) or unslanted holograms ($\theta_{\mathrm{s}} = \theta_{\mathrm{f}}$). Both reflection holograms ($|\theta_{\mathrm{s}} - \theta_{\mathrm{f}}| > 90°$) and transmission holograms ($|\theta_{\mathrm{s}} - \theta_{\mathrm{f}}| < 90°$) can be described by the k–sphere formulation.

Typically, for holograms recorded by non–plane waves, the k–sphere formulation is not frequently used, because the direction of the grating vector ($\mathbf{K}_{\mathrm{g}}$ in Fig. 2-1) is not uniquely defined. However, ray tracing softwares handle this situation efficiently through parallel processing. Once the local grating vector is defined where the incident ray hits the volume hologram, the diffracted ray can be computed by the k–sphere formulation. In our implementation described in the next section, two options are prepared to compute grating vectors: 1) holograms recorded by either plane waves or spherical waves and 2) holograms that have arbitrary grating vectors. In the first case, from descriptions of angle/position of a plane wave or point source, the grating vector is computed analytically, which is useful for a plane or spherical wave reference hologram. In the second case, the hologram is discretized into a grid and local grating vectors are assigned on the grid. Then, the implementation interpolates local grating vectors based on the assigned ones. A similar approach has been used to model non–plane wave reference holograms using coupled mode theory [29, 30].

Figure 2-2 shows various geometries of VHI systems with different volume hologram configurations. These figures are produced by ZEMAX® with our volume hologram model. Fig. 2-2(a), (b), and (c) use plane reference wave volume holograms, and Fig. 2-2(d), (e), and (f) have spherical wave reference volume holograms. Fig. 2-2(a), (b), and (d) have transmission holograms and Fig. 2-2(c), (e) and (f) have reflection holograms. Figure 2-2(a) uses an unslanted hologram and the rest use slanted ones. Both plane waves and spherical waves can be used for either the reference or signal wave as shown in Fig. 2-2(d), (e), and (f).

2.1.3 Implementation of the k–sphere formulation in ZEMAX®

In the k–sphere implementation with ZEMAX®, a User Defined Surface (UDS) was used. The UDS feature allows making users' own optical elements; one can even define special refraction, reflection, or diffraction laws. The UDS is represented by a *Microsoft Windows*® Dynamic Link Library (DLL), the file which contains functions invoked by ZEMAX® during design and simulation. Besides ZEMAX®, other commercial ray tracing software suites also provide customizable features; hence, this approach can be easily integrated in other software packages with proper minor modifications.

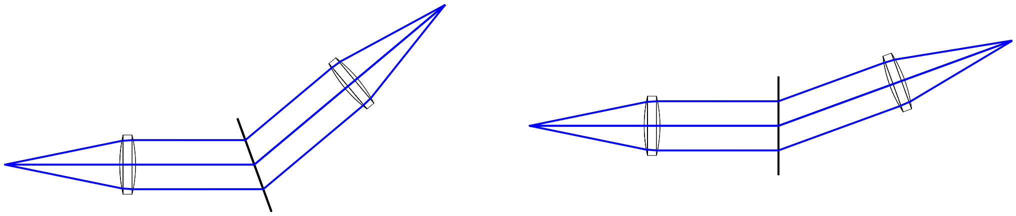

(a) Unslanted plane wave reference–plane wave signal transmission VH ($\theta_\mathrm{f} = \theta_\mathrm{s} = 20^\circ$)

(b) Slanted plane wave reference–plane wave signal transmission VH ($\theta_\mathrm{f} = 0^\circ, \theta_\mathrm{s} = 20^\circ$)

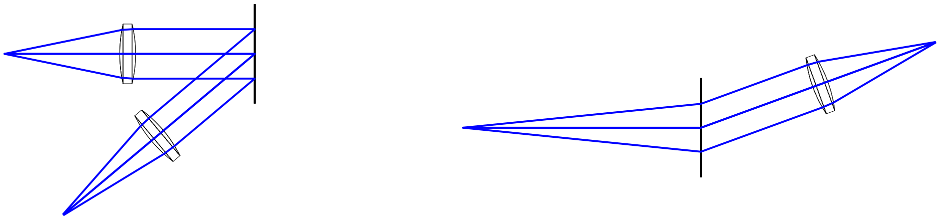

(c) Plane wave reference–plane wave signal reflection VH ($\theta_\mathrm{f} = 0^\circ, \theta_\mathrm{s} = 240^\circ$)

(d) Spherical wave reference–plane wave signal transmission VH ($d_\mathrm{f} = -60\,\mathrm{mm}$, $\theta_\mathrm{s} = 20^\circ$)

(e) Spherical wave reference–plane wave signal reflection VH ($d_\mathrm{f} = -60\,\mathrm{mm}$, $\theta_\mathrm{s} = 220^\circ$)

(f) Spherical wave reference–spherical wave signal reflection VH ($d_\mathrm{f} = -60\,\mathrm{mm}$, $d_\mathrm{s} = -60\,\mathrm{mm}$, $\theta_\mathrm{s} = 40^\circ$)

Figure 2-2: Layouts of several VHI systems with different volume hologram configurations. Images are produced by ZEMAX® with a realistic bi–convex lens (BK7, $f = 30$ mm). In (d), (e), and (f), d_f and d_s are distances from the volume hologram to point sources, which specify the origins of spherical wavefronts.

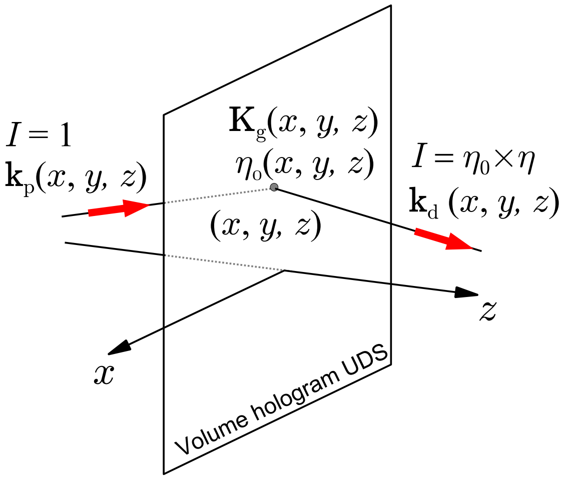

Figure 2-3: Schematic of volume hologram UDS implementation in ZEMAX®, where $\mathbf{K}_\mathrm{g}$ is the local grating vectors, η_0 is the local diffraction efficiency at (x, y, z), $\mathbf{k}_\mathrm{p}$ and $\mathbf{k}_\mathrm{d}$ are the k–vectors of the incident and diffracted ray, respectively. $\mathbf{k}_\mathrm{d}$ is computed by the k–sphere formulation. The intensity I of the diffracted ray is $\eta_0 \times \eta$, where η is computed by eq. (2.10).

Figure 2-3 describes how the ZEMAX® UDS computes Bragg diffraction. First, a volume hologram is considered as an infinitesimally thin surface. The thickness of the hologram is taken into account when the diffraction efficiency is computed. ZEMAX® chooses a single ray arriving on the hologram UDS. Then ZEMAX® computes the local grating vector $\mathbf{K}_\mathrm{g}$ and the k–vector of the incident ray by using direction cosines (l, m, n) and wavelength as

$$\mathbf{k}_\mathrm{p} = \begin{pmatrix} l \\ m \\ n \end{pmatrix} \frac{2\pi}{\lambda_\mathrm{p}}. \tag{2.7}$$

Using the geometrical relationships of the k–sphere, the diffracted ray vector $\mathbf{k}_\mathrm{d}$ and the Bragg mismatch vector $\delta\mathbf{k}_\mathrm{d}$ are identified to be

$$\mathbf{k}_\mathrm{d} = \begin{pmatrix} \mathbf{k}_{\mathrm{p},x} + \mathbf{K}_{\mathrm{g},x} \\ \mathbf{k}_{\mathrm{p},y} + \mathbf{K}_{\mathrm{g},y} \\ \sqrt{\left(\frac{2\pi}{\lambda_\mathrm{p}}\right)^2 - \left(\mathbf{k}_{\mathrm{p},x} + \mathbf{K}_{\mathrm{g},x}\right)^2 - \left(\mathbf{k}_{\mathrm{p},y} + \mathbf{K}_{\mathrm{g},y}\right)^2} \end{pmatrix} \tag{2.8}$$

and

$$\delta\mathbf{k}_{\mathrm{d}} = \mathbf{k}_{\mathrm{p}} + \mathbf{K}_{\mathrm{g}} - \mathbf{k}_{\mathrm{d}}. \tag{2.9}$$

The diffracted ray vector $\mathbf{k}_{\mathrm{d}}$ is normalized and the result is directly written into the ray data structure of diffracted rays.

The decrease of diffraction efficiency as a result of Bragg mismatch is taken into account by $\delta\mathbf{k}_{\mathrm{d}}$ in eq. (2.5). The normalized diffraction efficiency is equivalent to the relative transmittance of the surface for the given ray and the corresponding parameter of the data structure is `rel_surf_tran`, defined as

$$\texttt{rel\_surf\_tran} = \eta_0 \mathrm{sinc}^2\left(\frac{L\delta\mathbf{k}_{\mathrm{d}} \cdot \hat{\mathbf{z}}}{2\pi}\right), \tag{2.10}$$

where η_0 is the local diffraction efficiency. This feature allows the overall efficiency to be changed locally. Manufacturers typically provide hologram efficiency maps, hence the data can be substituted into $\eta_0(x, y)$. Note that $\mathbf{k}_{\mathrm{p}}, \mathbf{K}_{\mathrm{g}}, \mathbf{k}_{\mathrm{d}}$ and `rel_surf_tran` are computed for every ray being traced.

2.1.4 Examples

In this section, simulated results produced by ZEMAX® and our volume hologram model are presented. First the previously reported experimental data [7] are reproduced by simulation, then new directions of using ZEMAX® in VHI system design are addressed.

Depth selectivity

In the case of the VHI system with a plane wave reference hologram as shown in Fig. 2-2(a) and (b), maximum Bragg diffraction is achieved when the light from a point source is collimated and the resulting plane wave enters the volume hologram at the Bragg matched angle. If the point source leaves the front focal plane and moves along the optical axis, the wavefront entering the volume hologram is no longer a plane wave due to the defocus, causing attenuated Bragg diffraction. This example

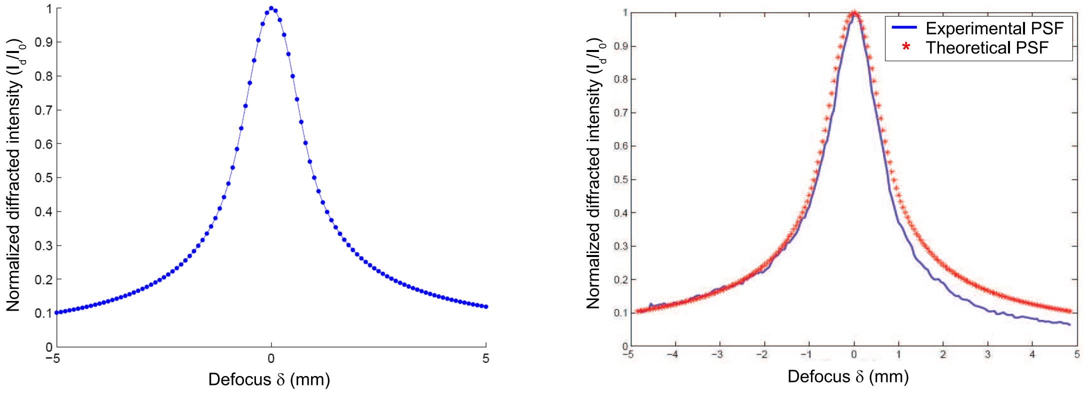

(a) Ray-tracing in ZEMAX®

(b) Analytical model and experiment (from Ref. [7])

Figure 2-4: Longitudinal PSF of a 4–f VHI system (*see text for parameters*)

demonstrates how the Bragg condition can be exploited to achieve depth selective imaging with volume holograms. We used a 4–f VHI system as shown in Fig. 2-2(b) (focal lengths $f_1 = f_2 = 50.2$mm) with a slanted volume hologram (radius $a = 3.5$mm, $\theta_{\mathrm{f}} = 0°$, $\theta_{\mathrm{s}} = 12°$, $L = 2$ mm) at the Fourier plane; the wavelength of recording and probe beam is 532 nm.

Figure 2-4(a) shows the ray-tracing simulated plot of the total diffracted intensity at the detector plane versus the defocus of the point source. The longitudinal PSF is defined [7] as the normalized diffraction efficiency with respect to defocus. Figure 2-4(b) shows an analytical simulation, overlayed with an experimental result [7] for the comparison showing good agreement.

Note that the asymmetry of the experimental longitudinal PSF in Fig. 2-4(b) is caused by vignetting due to the finite aperture stop. The ZEMAX® implementation in Fig. 2-4(a) includes the vignetting effect and produced the asymmetric longitudinal PSF.

Effect of geometrical aberrations in volumetric diffraction

An important advantage of the ray-tracing approach over analytical methods is that aberrations can be accounted for in a straightforward fashion. In the analytical model [7], the paraxial approximation and rotational symmetry were assumed for expressing

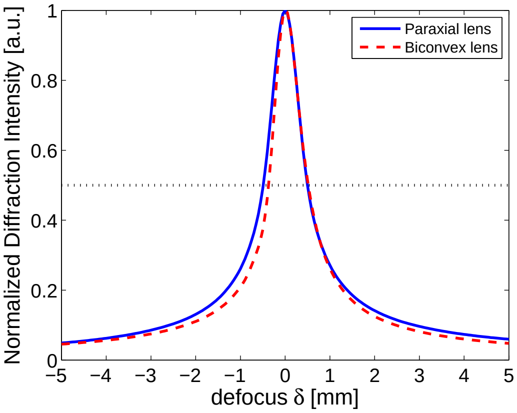

Figure 2-5: Longitudinal PSFs with a paraxial and aberrated lens, where $f_1 = 50.2\,\mathrm{mm}$, $L = 2\,\mathrm{mm}$, $\theta_\mathrm{s} = 23.1°$, $\lambda_\mathrm{f} = \lambda_\mathrm{p} = 532\,\mathrm{nm}$.

the wavefront inside the volume hologram; this prohibited aberrations other than spherical to be taken into account. Generally, one might expect that aberration reduces the Bragg diffraction efficiency and, consequently, the depth and wavelength selectivity of VHI systems is degraded. The ability to model aberration is essential for making full use of analysis and optimization tools in the design process.

Figure 2-5 presents a simple example showing the effect of aberration on the longitudinal PSF. In this case, two VHI systems with the ideal volume hologram represented by one $\mathbf{K}_\mathrm{g}$ vector are considered with two different objective lenses: 1) an ideal thin lens (which, observing the paraxial approximation, does not introduce any aberration in ZEMAX®), and 2) a realistic bi-convex lens made of BK7. The effective focal lengths of the two lenses are identical at a wavelength of 532 nm.

The aberrated lens yields slightly lower Bragg diffraction than the paraxial lens; unexpectedly, the FWHM(Full Width Half Maximum) of the longitudinal PSF is improved by 10% after the normalization. This implies that the depth resolution (defined as FWHM of the longitudinal PSF) can be engineered by managing aberrations, where the use of aberration potentially improves the depth characteristics.

Now another simple example is presented to demonstrate the capabilities of the ray tracing model in conjunction with the built-in analysis features of ZEMAX®. In the paraxial 4–f system, the first lens was replaced with an aberrated lens of constant focal length and various q factor (or shape factor), defined by

$$q = \frac{R_1 + R_2}{R_1 - R_2}, \tag{2.11}$$

where R_1 and R_2 are the radii of curvature of the front and back surfaces of the lens, respectively [31]. We conducted a simulation where both radii of curvature of the surfaces are changed while maintaining the focal length. It is well known that the severity of the spherical aberration is a function of q in this case. Fig. 2-6 shows three snapshots of the movie in Ref. [32], which shows the transformation of the first lens through different stages of a shape factor, a resulting diffraction pattern and a ray-fan diagram to quantify the severity of aberration.

Optimization example

As in any optical system, VHI requires careful optimization of all the optical elements in the system. In particular, the objective lens, which transforms the incoming wavefront to be matched to the volume hologram, is important as described in the previous example. This example demonstrates a simple optimization of a VHI system with respect to aberration. First, for both a regular 4–f system and VHI system, the optimization with the same merit function is run. Intuitively, the optimization would yield different results because both systems have somewhat different characteristics. Then we try to obtain similar results with different merit function, in which additional constraints are required for VHI system optimization.

The default merit function was used first, which minimizes the overall optical path length of the evaluated rays at 18 predefined points on the pupil plane. Both radii of curvature of the aberrated lens are selected as the parameters to be optimized. Column "DMF" (Default Merit Function) of Table 2.1 shows the result after $1,000$ iterations.

In this particular example, the point source is on the optical axis and thus spherical aberration is dominant. With a singlet, the minimum spherical aberration is achieved

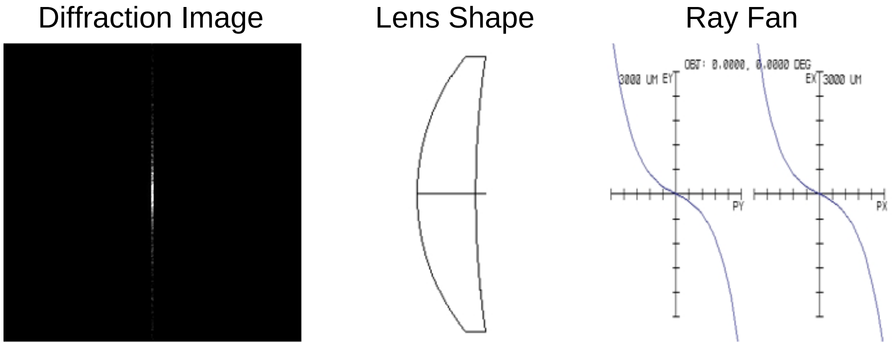

(a) $q = 1.5975$

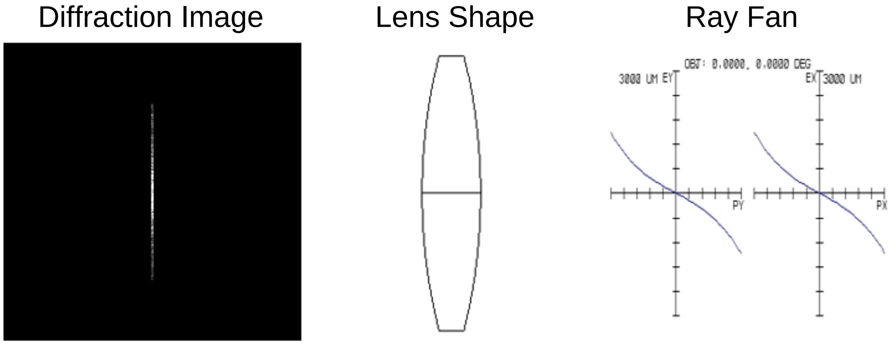

(b) $q = 0.0054$

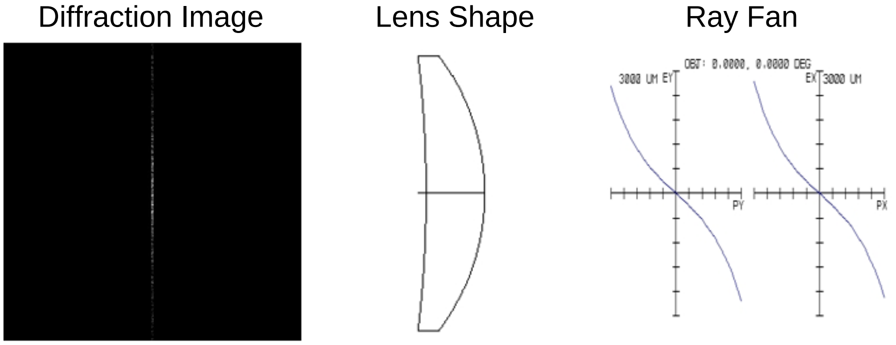

(c) $q = -1.4935$

Figure 2-6: Diffraction image, lens shape, and ray fan for various q–factors [32]

Parameters	4–f system		VHI system		
	Initial	DMF	Initial	DMF	DMF+IMAE
R_1 [mm]	30.5	123.892	30.5	34.416	68.815
R_2 [mm]	-30.5	-19.774	-30.5	-31.362	-21.910
Shape factor q [a.u.]	0	0.724	0	0.0464	0.5170
Merit function value [a.u.]	20.132	2.231	21.167	10.869	11.891
Diffraction efficiency [%]	–	–	3.566	23.746	33.264

Table 2.1: Optimization of the 4–f and VHI system using the default merit function. The last column is computed by the IMAE operand in the merit function.

when the shape factor is

$$q_{\text{min.SA}} = \frac{-2(n^2-1)}{n+2}, \tag{2.12}$$

where n is the refractive index of the lens [33]. For BK7 glass (n=1.5195 @532.8 nm), $q_{\text{min.SA}}$ is 0.7437. Note that in the regular 4–f system, the optimized shape factor (0.7240) is very close to $q_{\text{min.SA}}$, while the shape factor of the VHI system is only 0.0464. This is because of the merit function chosen; all rays diffracted by the hologram have the same weighting values with respect to the optimization goal. Note that the optimization results in different shape factors for the VHI systems.

Instead of using the default merit function, a more practical choice is to increase the intensity of the diffracted beams. Hence, the merit function was modified to give less weight to the rays attenuated due to Bragg mismatch. In ZEMAX®, this can be done by defining the merit function to maximize the IMAE operand, which measures the integrated intensity at the detector plane. The rightmost column labeled "DMF+IMAE" of Table 2.1 shows how the modified merit function leads to an improved overall diffraction efficiency of the VHI system. Note the optimized shape factor (0.5170) with IMAE operand is much closer to $q_{\text{min.SA}}$ than the value (0.0464) computed with the default merit function only.

2.1.5 Discussion

A ray tracing approach for the simulation and optimization of VHI systems has been described. The model for volumetric diffraction is based on the k–sphere formulation, whose applicability is verified by comparison with results of our previous model [8]. The ZEMAX® User Defined Surface was utilized to demonstrate how the model can be easily integrated into current commercial ray-tracing softwares. The k–sphere module integrated in ZEMAX® can simulate various volume holograms including reflection, transmission, slanted, and unslanted holograms. Moreover, the module computes the local grating vector analytically or numerically from given data, which allows simulating not only plane or spherical wave reference holograms but also holograms with arbitrary grating vectors. Using the local efficiency parameter η_0, we also account for absolute diffraction efficiency changes resulting from material properties or index variation. Through several examples, it is demonstrated how ray-tracing based analysis and optimization tools are used in conjunction with our model to assist in the design process of VHI systems. The implemented model is ready to simulate aberrations in VHI systems and it is shown that optimization tools can be applied to mitigate the effects of aberration or even benefit from them. This approach can be integrated with other ray tracing software packages.

2.2 k–sphere formulation in 3D space

In Fig. 2-1, $\mathbf{k}_\mathrm{f}$, $\mathbf{k}_\mathrm{s}$, $\mathbf{k}_\mathrm{p}$, $\mathbf{k}_\mathrm{d}$ and $\mathbf{K}_\mathrm{g}$ are in plane (x–z plane) vectors, and the k–sphere appears as a circle. In this section, we consider an out–of–plane $\mathbf{k}_\mathrm{p}$ whose y–component is not zero, extending the formulation into 3D space. The image of the Bragg diffraction probed by out–of–plane probe beams is particularly interesting. For spherical wave reference holograms, it has previously been observed that the Bragg diffraction image has a curvature [7, 34, 35]. Previously reported analytical methods [7, 8, 27] assume a paraxial approximation, which predict a straight–line Bragg diffraction image lying along the y–axis in the case of plane wave reference holograms. In this section, the k–sphere method is used in 3D space and the Bragg diffraction images are verified to have a curved shape even in the case of plane wave reference holograms. An analytical expression of the curvature is also derived.

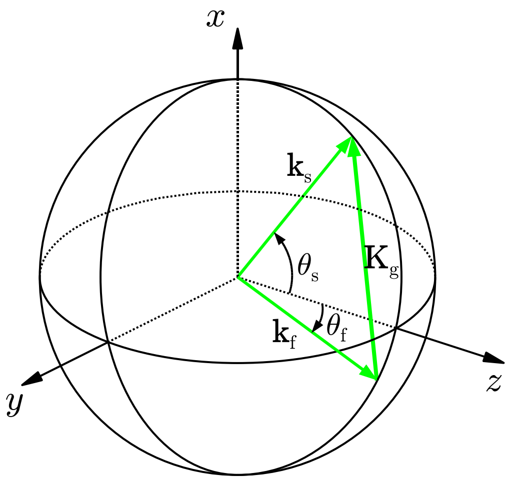

Figure 2-7: The k–sphere representation in 3D space, where the grating vector $\mathbf{K}_{\mathrm{g}}$ is constructed by $\mathbf{k}_{\mathrm{s}}$ and $\mathbf{k}_{\mathrm{f}}$.

2.2.1 Bragg diffraction from out–of–plane probe beams

As shown in Fig. 2-7, the plane wave reference hologram is considered, which is recorded by two mutually coherent waves whose k–vectors are $\mathbf{k}_{\mathrm{s}}$ and $\mathbf{k}_{\mathrm{f}}$ in 3D space. Both k–vectors are on the x–z plane, where their angles to the z axis are θ_{s} and θ_{f}, respectively. Note that $\theta_{\mathrm{f}} = -\theta_{\mathrm{s}}$ for an unslanted hologram.

Throughout this section, the geometry shown in Fig. 2-8 is considered, where the collector lens behind the volume hologram is perpendicular to $\mathbf{k}_{\mathrm{s}}$ and the Bragg matched beam is focused at $x' = y' = 0$ on the image plane.

Next out–of–plane $\mathbf{k}_{\mathrm{p}}$ and $\mathbf{k}_{\mathrm{d}}$ are considered, whose y–components are non–zero. Since the tip of the grating vector $\mathbf{K}_{\mathrm{g}}$ should be on the k–sphere to satisfy the Bragg condition, the only possible arrangement is that $\mathbf{K}_{\mathrm{g}}$ forms a cylinder and the tip of $\mathbf{k}_{\mathrm{p}}$ and $\mathbf{k}_{\mathrm{d}}$ are on the edges of the cylinder as shown in Fig. 2-9.

To find the Bragg diffraction images, two angles $\phi_{\mathrm{x}'}$ and $\phi_{\mathrm{y}'}$ are defined first, and later they are converted into the image plane coordinates x' and y', where $\phi_{\mathrm{x}'}$ is the angle between $\mathbf{k}_{\mathrm{d}}$ and the sagittal plane of the FT lens (the plane consisting of $\mathbf{k}_{\mathrm{s}}$ and the y–axis) and $\phi_{\mathrm{y}'}$ is the angle between $\mathbf{k}'_{\mathrm{d}}$ and the x–z plane as shown in Fig. 2-10, where $\mathbf{k}_{\mathrm{d}}$ is the Bragg matched diffracted beam and $\mathbf{k}'_{\mathrm{d}}$ is the projection of $\mathbf{k}_{\mathrm{d}}$ onto the sagittal plane (the y'–z' plane) of the collector lens.

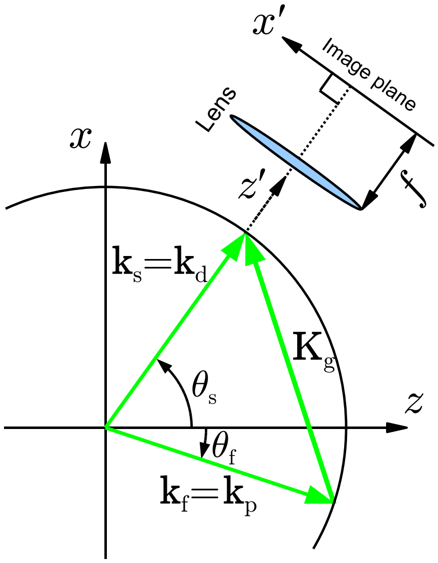

Figure 2-8: The geometry of the collector lens and image plane (side–view from y–axis)

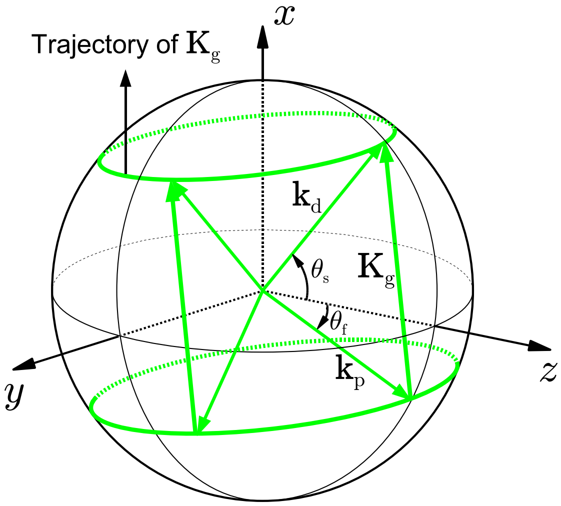

Figure 2-9: The trajectory of $\mathbf{K}_g$ that satisfies the Bragg condition

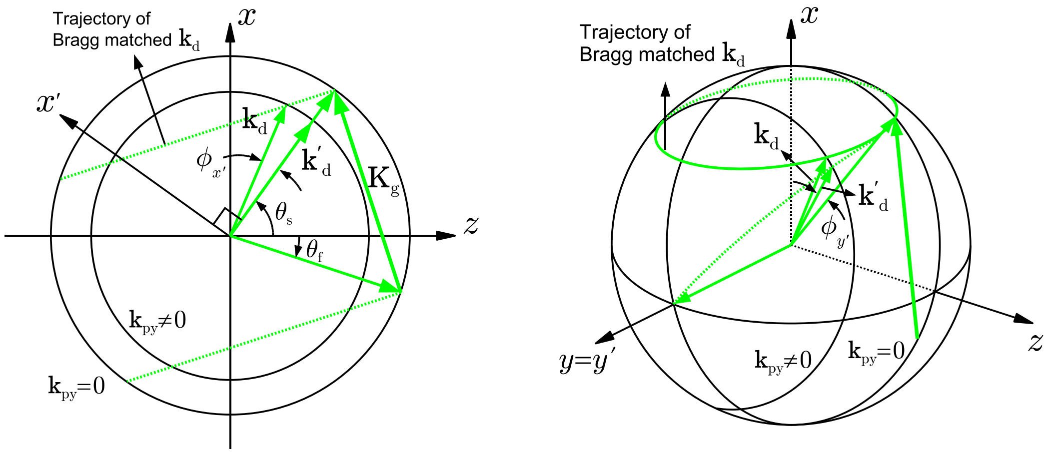

(a) side–view from the y-axis

(b) 3–D view

Figure 2-10: The definition of $\phi_{\mathrm{x}'}$ and $\phi_{\mathrm{y}'}$. The trajectory of $\mathbf{k}_\mathrm{d}$ as k_y increases.

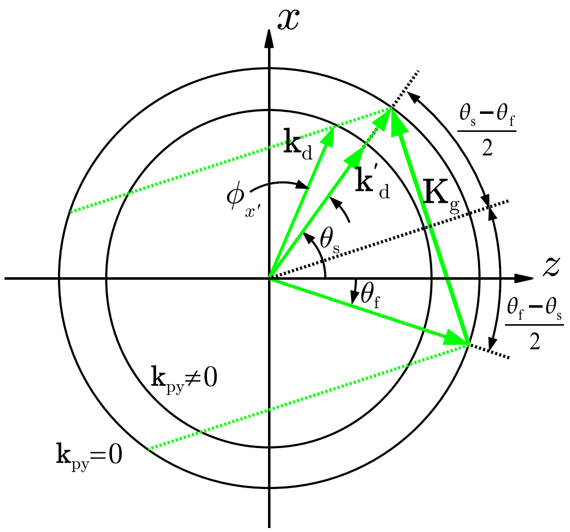

Figure 2-11: The geometrical representation of $\phi_{\mathrm{x}'}$

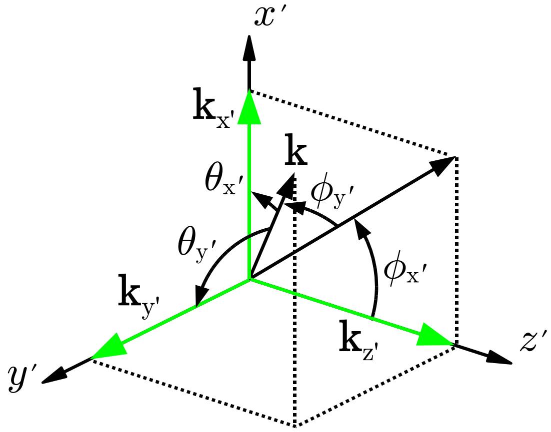

Figure 2-12: The coordinate transform from $\phi_{x'}$ and $\phi_{y'}$ to $\theta_{x'}$ and $\theta_{y'}$

From the geometry shown in Fig. 2-11, we obtain the relation between $\phi_{x'}$ and $\phi_{y'}$ which satisfies

$$\phi_{x'} = \sin^{-1}\left[\frac{\lambda_p \sin\left(\frac{\theta_s-\theta_f}{2}\right)}{\lambda_f \cos\left(\phi_{y'}\right)}\right] - \left(\frac{\theta_s-\theta_f}{2}\right). \tag{2.13}$$

Then $\phi_{x'}$ and $\phi_{y'}$ are converted to $\theta_{x'}$ and $\theta_{y'}$, where $\theta_{x'}$ and $\theta_{y'}$ are defined as the angles with respect to the x' and y' axes as shown in Fig. 2-12; $\theta_{x'}$ and $\theta_{y'}$ directly correspond to the x' and y' coordinates on the image plane. Then, we obtain

$$\sin\theta_{x'} = \cos\phi_{y'}\sin\phi_{x'}, \qquad \text{and} \tag{2.14}$$

$$\sin\theta_{y'} = \sin\phi_{y'}. \tag{2.15}$$

By using eqs. (2.13)– (2.15), the Bragg diffraction pattern on the image plane is computed. Figure 2-13 shows the trajectory of maximum intensity in the Bragg diffraction images with volume holograms of $\theta_f = -20°$ and $\theta_f = -40°$ for different values of θ_s. In the paraxial region where y' is small, the trajectory is almost a straight line. However, as y' increases, the Bragg diffraction images become more curved crescents.

Figure 2-14 shows the trajectory of the maximum intensity in the Bragg diffraction images for various unslanted holograms. Note that even an unslanted hologram with a constant $\mathbf{K}_g$ produces curved Bragg diffraction images while previous theoretical

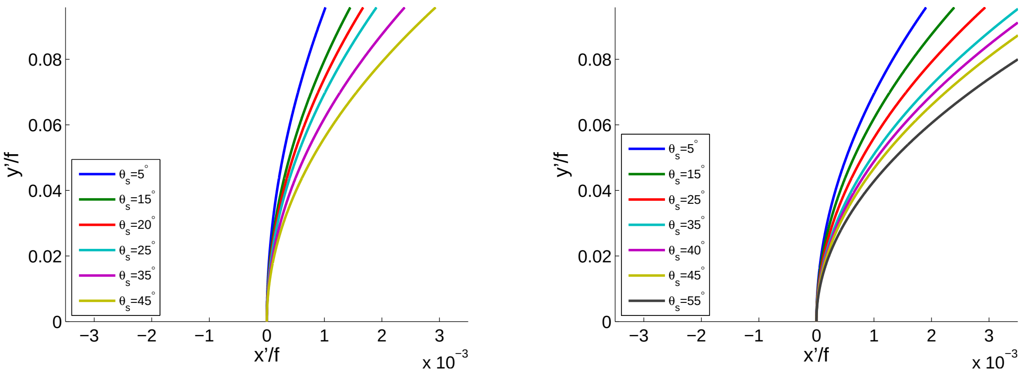

(a) $\theta_{\mathrm{f}} = -20°$ (b) $\theta_{\mathrm{f}} = -40°$

Figure 2-13: The trajectory of the maximum intensity of the Bragg diffraction on the image plane for various θ_{s} and θ_{f} when $\lambda_{\mathrm{p}} = \lambda_{\mathrm{f}}$

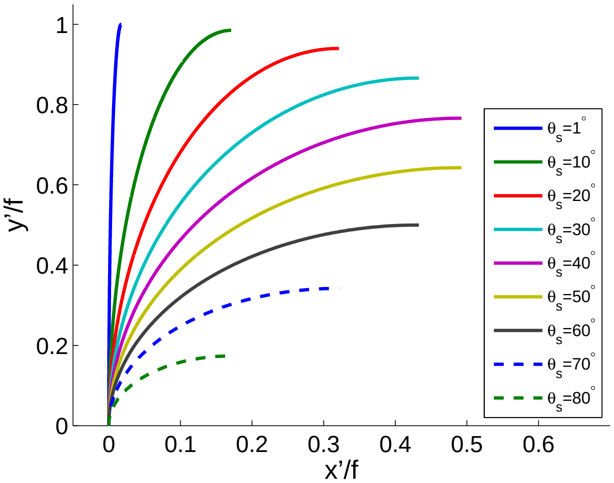

Figure 2-14: The trajectory of the maximum Bragg diffraction on the image plane of unslanted holograms ($\theta_{\mathrm{f}} = -\theta_{\mathrm{s}}$)

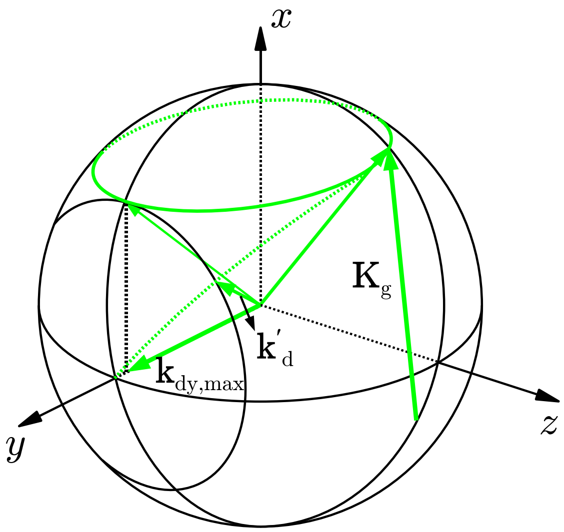

Figure 2-15: The maximum $\mathbf{k}_\mathrm{dy}$ of a Bragg matched diffracted beam

models predicted a straight line. There is also a cut–off in the trajectories which implies the existence of a maximum $\mathbf{k}_\mathrm{dy}$. Figure 2-15 shows the condition of the cut–off, where $\mathbf{k}_\mathrm{dy,max}$ decreases as θ_s increases.

In the reflection hologram ($\theta_\mathrm{s} = 90°$ and $\theta_\mathrm{f} = -90°$), $\mathbf{k}_\mathrm{dy,max}$ is zero as shown in Fig. 2-16. There is no other possible arrangement of $\mathbf{k}_\mathrm{d}$ except the one identical to $\mathbf{k}_\mathrm{s}$; even small deviation of k_py prohibits the Bragg diffraction and the angular selectivity is maximized.

The crescent shape of the Bragg diffraction image is also dependent on the wavelength of the probe beam. Different wavelengths create k–spheres of different radii as shown in Fig. 2-17. A probe beam with longer wavelength produces a k–sphere of a shorter radius, which produces more curved Bragg diffraction images. Similarly the probe beam with longer wavelength requires larger θ_f and θ_s for Bragg matching, and thus the crescent should be more curved as $\mathbf{k}_\mathrm{py}$ increases.

Figure 2-18 shows the trajectory of the maximum intensity in the Bragg diffraction images for three different wavelengths. Due to the wavelength degeneracy, the center of the crescent is shifted as shown in Fig. 2-18(a). For comparison, the crescents are shifted at the center in Fig. 2-18(b). Note that the longer wavelength produces more curved trajectories as expected.

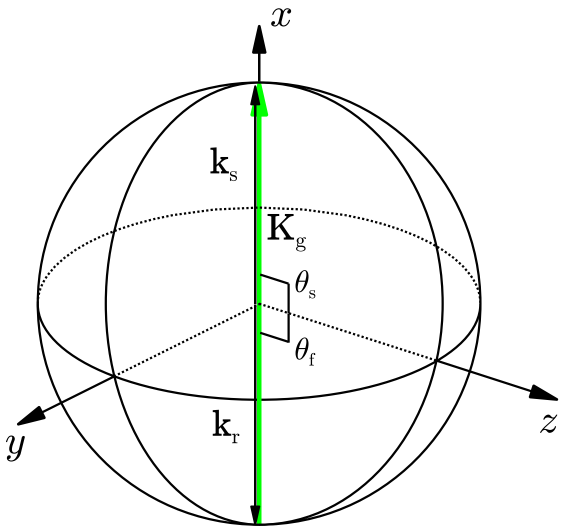

Figure 2-16: The k–sphere for an unslanted reflection hologram

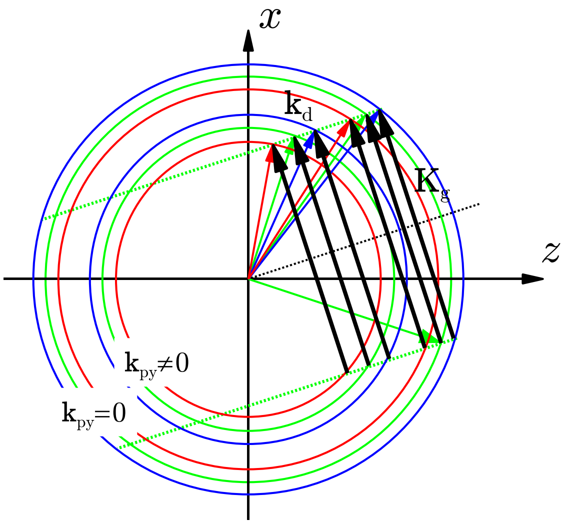

Figure 2-17: The k–spheres for three different wavelengths

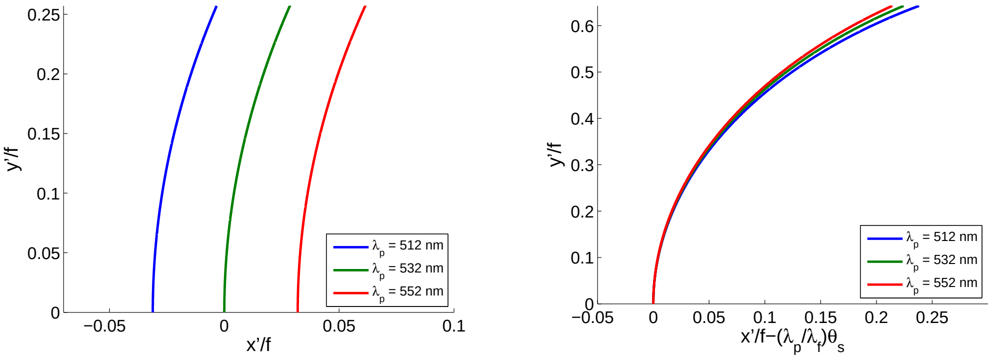

(a) trajectories on the image plane (b) shift compensated trajectories

Figure 2-18: The trajectories of the maximum intensity of Bragg diffraction at the image plane, where the wavelength of the reference beam is 532 nm. In (a), they appeared shifted due to the wavelength degeneracy. For each comparison of the curvatures, they are centered at the origin in (b). The hologram is an unslanted hologram with $\theta_s = -\theta_{\mathrm{f}} = 40°$.

2.2.2 Analytical solution of the k–sphere method for the curved Bragg diffraction images

In this section, the analytical solution of the curved Bragg diffraction images is derived. The geometry is identical to Fig. 2-7. The grating vector $\mathbf{K}_{\mathrm{g}}$ is written as

$$\mathbf{K}_{\mathrm{g}} = \mathbf{k}_{\mathrm{s}} - \mathbf{k}_{\mathrm{f}} = \frac{2\pi}{\lambda}\left[\hat{x}\left(\sin\theta_{\mathrm{s}} - \sin\theta_{\mathrm{f}}\right) + \hat{z}\left(\cos\theta_{\mathrm{s}} - \cos\theta_{\mathrm{f}}\right)\right], \tag{2.16}$$

and the wavevector of the probe beam is written as

$$\mathbf{k}_{\mathrm{p}} = \frac{2\pi}{\lambda}\left(\hat{x}\cos\alpha_x + \hat{y}\cos\alpha_y + \hat{z}\cos\alpha_z\right), \tag{2.17}$$

where α_x, α_y, and α_z are the direction cosines of $\mathbf{k}_{\mathrm{p}}$ with respect to the x, y, and z axes, respectively. The angles θ_{px} and θ_{py} are defined as

$$\cos\alpha_x \equiv \sin\theta_{\mathrm{px}}, \quad \text{and} \tag{2.18}$$

$$\cos\alpha_y \equiv \sin\theta_{\mathrm{py}}. \tag{2.19}$$

The wavevector components of the Bragg diffracted ray vector $\mathbf{k}_{\mathrm{d}}$ are

$$\begin{aligned} k_{\mathrm{dx}} &= \frac{2\pi}{\lambda}\left(\sin\theta_{\mathrm{s}} - \sin\theta_{\mathrm{f}} + \sin\theta_{\mathrm{px}}\right), && (2.20)\\ k_{\mathrm{dy}} &= \frac{2\pi}{\lambda}\sin\theta_{\mathrm{py}}, \qquad \text{and} && (2.21)\\ k_{\mathrm{dz}} &= \left(\frac{2\pi}{\lambda}\right)\left[1 - k_{\mathrm{dx}}^2 - k_{\mathrm{dy}}^2\right]^{1/2} \\ &= \left(\frac{2\pi}{\lambda}\right)\left[1 - \left(\sin\theta_{\mathrm{s}} - \sin\theta_{\mathrm{f}} + \sin\theta_{\mathrm{px}}\right)^2 - \sin^2\theta_{\mathrm{py}}\right]^{1/2}. && (2.22)\end{aligned}$$

Using the small angle approximation,

$$\begin{aligned} \theta_{\mathrm{py}} &= \theta'_{\mathrm{y}} && (2.23)\\ \theta_{\mathrm{px}} &= \theta_{\mathrm{f}} + \theta'_{\mathrm{x}}, && (2.24)\end{aligned}$$

where $\theta'_{\mathrm{x}} \ll 1$ and $\theta'_{\mathrm{y}} \ll 1$, we obtain

$$\begin{aligned} \sin\theta_{\mathrm{px}} &= \sin(\theta_{\mathrm{f}} + \theta'_{\mathrm{x}}) \approx \sin\theta_{\mathrm{f}} + \theta'_{\mathrm{x}}\cos\theta_{\mathrm{f}}, \quad \text{and} && (2.25)\\ \sin\theta_{\mathrm{py}} &\approx \theta'_{\mathrm{y}}. && (2.26)\end{aligned}$$

Then, k_{dz} is approximated as

$$\begin{aligned} k_{\mathrm{dz}} = \frac{2\pi}{\lambda}&\left[1 - \left(\sin\theta_{\mathrm{s}} - \sin\theta_{\mathrm{f}} + \sin\theta_{\mathrm{f}} + \theta'_{\mathrm{x}}\cos\theta_{\mathrm{f}}\right)^2 - \theta'^2_{\mathrm{y}}\right]^{1/2} \\ &= \frac{2\pi}{\lambda}\left[1 - \sin^2\theta_{\mathrm{s}} - \cos^2\theta_{\mathrm{f}}\theta'^2_{\mathrm{x}} - 2\sin\theta_{\mathrm{s}}\cos\theta_{\mathrm{f}}\theta'_{\mathrm{x}} - \theta'^2_{\mathrm{y}}\right]^{1/2} \\ &= \frac{2\pi}{\lambda}\left[\cos^2\theta_{\mathrm{s}} - 2\sin\theta_{\mathrm{s}}\cos\theta_{\mathrm{f}}\theta'_{\mathrm{x}} - \left(\cos^2\theta_{\mathrm{f}}\theta'^2_{\mathrm{x}} + \theta'^2_{\mathrm{y}}\right)\right]^{1/2} \\ &\approx \frac{2\pi}{\lambda}\cos\theta_{\mathrm{s}}\left[1 - 2\frac{\sin\theta_{\mathrm{s}}\cos\theta_{\mathrm{f}}}{\cos^2\theta_{\mathrm{s}}}\theta'_{\mathrm{x}} - \frac{\cos^2\theta_{\mathrm{f}}\theta'^2_{\mathrm{x}} + \theta'^2_{\mathrm{y}}}{\cos^2\theta_{\mathrm{s}}}\right]^{1/2}. \qquad (2.27)\end{aligned}$$

A Taylor series expansion can be applied to further simplify k_{dz}. A general form of eq. (2.27) is given by

$$f(\epsilon_1, \epsilon_2) = \sqrt{1 + \alpha_1\epsilon_1 + \beta_1\epsilon_1^2 + \beta_2\epsilon_2^2}. \qquad (2.28)$$

Using the Taylor series with respect to ϵ_1 and ϵ_2 expands eq. (2.28) as

$$f(\epsilon_1, \epsilon_2) \simeq f(0,0) + \frac{\partial f}{\partial \epsilon_1}\epsilon_1 + \frac{\partial f}{\partial \epsilon_2}\epsilon_2 + \frac{1}{2}\frac{\partial^2 f}{\partial \epsilon_1^2}\epsilon_1^2 + \frac{1}{2}\frac{\partial^2 f}{\partial \epsilon_2^2}\epsilon_2^2 + \frac{\partial^2 f}{\partial \epsilon_1 \partial \epsilon_2}\epsilon_1\epsilon_2 + \dots, \tag{2.29}$$

at $\epsilon_1 = \epsilon_2 = 0$, which is simplified to

$$f(\epsilon_1, \epsilon_2) \simeq 1 + \frac{\alpha_1}{2}\epsilon_1 + \frac{4\beta_1 - \alpha_1^2}{8}\epsilon_1^2 + \frac{\beta_2}{2}\epsilon_2^2. \tag{2.30}$$

Thus, for small θ'_x and θ'_y, eq. (2.27) is approximately written as

$$\begin{aligned} k_\mathrm{dz} &= \frac{2\pi}{\lambda}\cos\theta_\mathrm{s}\left[1 - 2\frac{\sin\theta_\mathrm{s}\cos\theta_\mathrm{f}}{\cos^2\theta_\mathrm{s}}\theta'_\mathrm{x} - \frac{\cos^2\theta_\mathrm{f}\theta'^2_\mathrm{x} + \theta'^2_\mathrm{y}}{\cos^2\theta_\mathrm{s}}\right] \\ &\simeq \frac{2\pi}{\lambda}\cos\theta_\mathrm{s}\left[1 - \frac{\sin\theta_\mathrm{s}\cos\theta_\mathrm{f}}{\cos^2\theta_\mathrm{s}}\theta'_\mathrm{x} - \frac{1}{2}\left(\frac{\cos^2\theta_\mathrm{f}}{\cos^2\theta_\mathrm{s}} + \frac{\sin^2\theta_\mathrm{s}\cos^2\theta_\mathrm{f}}{\cos^4\theta_\mathrm{s}}\right)\theta'^2_\mathrm{x} - \frac{1}{2}\frac{1}{\cos^2\theta_\mathrm{s}}\theta'^2_\mathrm{y}\right]. \end{aligned} \tag{2.31}$$

The Bragg mismatch vector is

$$\Delta k_\mathrm{dz} = \left(\frac{2\pi}{\lambda}\right)(\cos\theta_\mathrm{s} - \cos\theta_\mathrm{f} + \cos\alpha_z) - k_\mathrm{dz}. \tag{2.32}$$

By using the small angle approximation again, $\cos\alpha_z$ is simplified as

$$\begin{aligned} \cos\alpha_z &= \sqrt{1 - \sin^2\theta_\mathrm{px} - \sin^2\theta_\mathrm{py}} \simeq \sqrt{1 - (\sin\theta_\mathrm{f} + \theta'_\mathrm{x}\cos\theta_\mathrm{f})^2 - \theta'^2_\mathrm{y}} \\ &= \cos\theta_\mathrm{f}\sqrt{1 - \frac{2\sin\theta_\mathrm{f}\cos\theta_\mathrm{f}}{\cos^2\theta_\mathrm{f}}\theta'_\mathrm{x} - \left(\theta'^2_\mathrm{x} + \frac{1}{\cos^2\theta_\mathrm{f}}\theta'^2_\mathrm{y}\right)} \\ &\approx \cos\theta_\mathrm{f}\left[1 - \frac{\sin\theta_\mathrm{f}\cos\theta_\mathrm{f}}{\cos^2\theta_\mathrm{f}}\theta'_\mathrm{x} - \frac{1}{2}\left(1 + \frac{\sin^2\theta_\mathrm{f}}{\cos^2\theta_\mathrm{f}}\right)\theta'^2_\mathrm{x} - \frac{1}{2}\frac{\theta'^2_\mathrm{y}}{\cos^2\theta_\mathrm{f}}\right] \end{aligned} \tag{2.33}$$

Finally, the Bragg mismatch vector is written as

$$\begin{aligned} \Delta k_\mathrm{dz} = \left(\frac{2\pi}{\lambda}\right)\Bigg[&\left(\frac{\sin\theta_\mathrm{s}\cos\theta_\mathrm{f}}{\cos\theta_\mathrm{s}} - \sin\theta_\mathrm{f}\right)\theta'_\mathrm{x} + \frac{1}{2}\left(\frac{1}{\cos\theta_\mathrm{s}} - \frac{1}{\cos\theta_\mathrm{f}}\right)\theta'^2_\mathrm{y} \\ &+ \frac{1}{2}\left(\frac{\cos^2\theta_\mathrm{f}}{\cos\theta_\mathrm{s}} + \frac{\sin^2\theta_\mathrm{s}\cos^2\theta_\mathrm{f}}{\cos^3\theta_\mathrm{s}} - \cos\theta_\mathrm{f} - \frac{\sin^2\theta_\mathrm{f}}{\cos\theta_\mathrm{f}}\right)\theta'^2_\mathrm{x}\Bigg]. \end{aligned} \tag{2.34}$$

If $\Delta k_{\mathrm{dz}} = 0$, then the trajectory of θ'_{x} and θ'_{y} in eq. (2.34) represents the deviation angles of the probe beam that create the strongest Bragg diffraction, whose general form is a quadratic curve as

$$a\theta'^2_{\mathrm{x}} + 2b\theta'_{\mathrm{x}} + c\theta'^2_{\mathrm{y}} = 0, \tag{2.35}$$

where

$$\begin{aligned} a &= \frac{\cos^2\theta_{\mathrm{f}}}{\cos\theta_{\mathrm{s}}} + \frac{\sin^2\theta_{\mathrm{s}}\cos^2\theta_{\mathrm{f}}}{\cos^3\theta_{\mathrm{s}}} - \cos\theta_{\mathrm{f}} - \frac{\sin^2\theta_{\mathrm{f}}}{\cos\theta_{\mathrm{f}}} = \frac{\cos^2\theta_{\mathrm{f}}}{\cos^3\theta_{\mathrm{s}}} - \frac{1}{\cos\theta_{\mathrm{f}}}, && (2.36)\\ b &= \frac{\sin\theta_{\mathrm{s}}\cos\theta_{\mathrm{f}}}{\cos\theta_{\mathrm{s}}} - \sin\theta_{\mathrm{f}} = \cos\theta_{\mathrm{f}}\tan\theta_{\mathrm{s}} - \sin\theta_{\mathrm{f}}, \quad \text{and} && (2.37)\\ c &= \frac{1}{\cos\theta_{\mathrm{s}}} - \frac{1}{\cos\theta_{\mathrm{f}}}. && (2.38) \end{aligned}$$

For $-\pi/2 < (\theta_{\mathrm{s}}, \theta_{\mathrm{f}}) < \pi/2$, the ratio of a and c never becomes negative as

$$\frac{a}{c} = \frac{\dfrac{\cos^2\theta_{\mathrm{f}}}{\cos^3\theta_{\mathrm{s}}} - \dfrac{1}{\cos\theta_{\mathrm{f}}}}{\dfrac{1}{\cos\theta_{\mathrm{s}}} - \dfrac{1}{\cos\theta_{\mathrm{f}}}} = \frac{\cos^2\theta_{\mathrm{f}} + \cos\theta_{\mathrm{f}}\cos\theta_{\mathrm{s}} + \cos^2\theta_{\mathrm{s}}}{\cos^2\theta_{\mathrm{s}}} \geq 0. \tag{2.39}$$

This result indicates that the trajectory of θ'_{x} and θ'_{y} is indeed an ellipse. Note that for unslanted holograms ($\theta_{\mathrm{f}} = -\theta_{\mathrm{s}}$), $a = 0$, $b = 2\tan\theta_{\mathrm{s}}$, and $c = 0$, which means that $\theta'_{\mathrm{x}} = 0$ for all θ'_{y}. Therefore the curve becomes a straight line along the y axis in the object space. Thus, in the case of unslanted volume hologram, the field of view, the object points that produce strong diffraction, forms a straight line.

To examine the Bragg diffraction pattern on the image plane, we compute k_{dx} and k_{dy} for given θ'_{x} and θ'_{y}. Since k_{dx} and k_{dy} are defined with respect to the x and y axes, they should be converted in the x' and z' coordinates. From the geometry shown in Fig. 2-19, we obtain the coordinate transform from (x, y) to (x', y') as

$$\begin{pmatrix} x' \\ z' \end{pmatrix} = \begin{pmatrix} \cos\theta_{\mathrm{s}} & -\sin\theta_{\mathrm{s}} \\ \sin\theta_{\mathrm{s}} & \cos\theta_{\mathrm{s}} \end{pmatrix} \begin{pmatrix} x \\ z \end{pmatrix}. \tag{2.40}$$

Using eqs. (2.40) and (2.34) with $\Delta k_{\mathrm{dz}} = 0$, we obtain the trajectory of the maximum

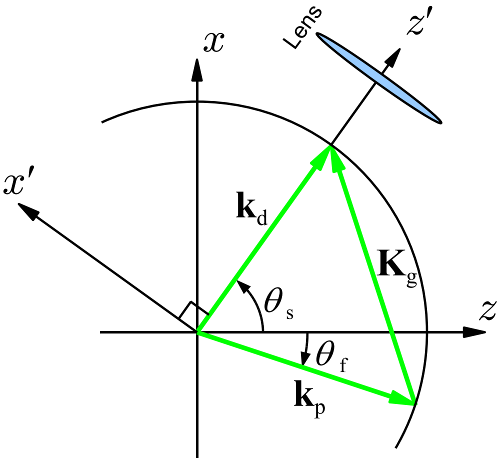

Figure 2-19: The coordinate transform from $\theta'_{\rm x}$ and $\theta'_{\rm y}$ to $\theta_{\rm x'}$ and $\theta_{\rm y'}$, where all angles are defined with respect to the x, y, x', and y' axes.

intensity of the Bragg diffraction on the image plane, which is a distorted ellipse.

Comparisons

In Fig. 2-20, the results from the k–sphere method and the analytical solution are plotted together for $\theta_{\rm f} = -20°$ and $\theta_{\rm f} = -40°$. As expected, the two results are in good agreement.

Figure 2-21(a) shows the curved Bragg diffraction images captured in experiments [36]; multiplexed holograms produced 5 diffraction images. The center curve is the diffraction image from a plane reference hologram. The simulated Bragg diffraction image with identical parameters as the experiments is plotted in Fig. 2-21(b).

2.2.3 Discussion

The shape of the Bragg diffraction images are examined in detail; the general form of the curved Bragg diffraction image is a distorted ellipse. Generally, as the angle between the reference and signal beams increases, the Bragg diffraction image becomes more curved. However, this formula only holds for the plane wave reference hologram. Again, for holograms with shift variant grating vectors, it is difficult to

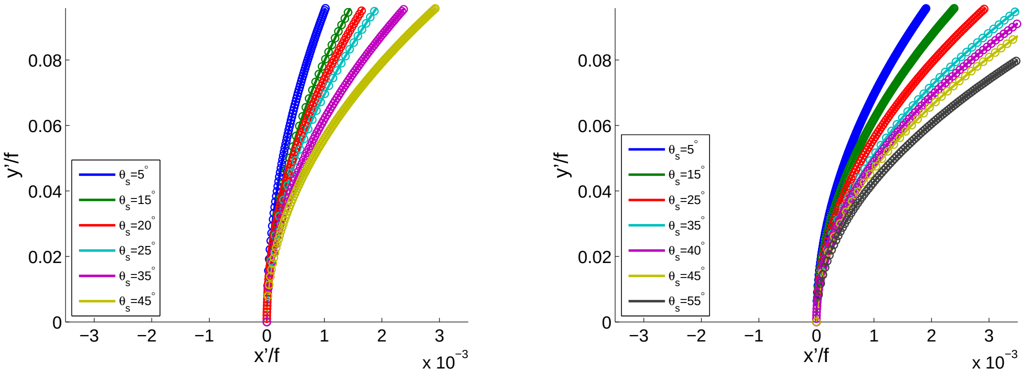

(a) $\theta_{\mathrm{f}} = -20°$

(b) $\theta_{\mathrm{f}} = -40°$

Figure 2-20: The comparison of the k–sphere method (solid line also shown in Fig. 2-13) and the analytic solution (circles) computed from eqs. (2.35) and (2.40). The colors of the lines represent different θ_{s}.

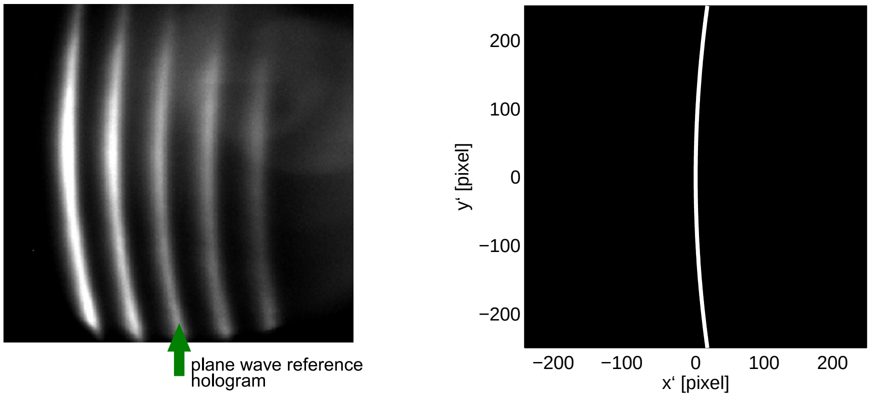

(a) Experimental images

(b) Simulation with the k–sphere

Figure 2-21: The crescent shape of the Bragg diffraction image. The experimental images are obtained from a multiplexed hologram. The curve at the center in (a) is the Bragg diffraction image of a plane reference wave hologram. ($\theta_{\mathrm{s}} = -\theta_{\mathrm{f}} = 34°$, L=2.11 mm, NA=0.55, f_2=20 mm, CCD pixel size is 16 μm, and total number of the pixels are 512×512 [36].)

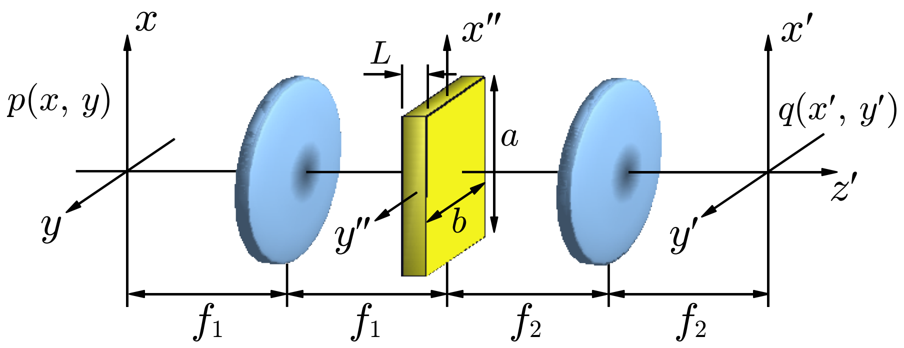

Figure 2-22: Geometry of a 4–f system. A volume hologram is inserted at the Fourier plane.

obtain analytical expressions of the Bragg diffraction images; the integrated k–sphere method with ZEMAX® handles this situation much more efficiently.

2.3 Wave optics formulation of volume holographic imaging systems

In this section, we revisit the scalar diffraction theory of VHI systems that are reported in Ref. [26, 27]. Due to the finite extent of the longitudinal dimension of volume holograms, the VHI systems have 3D pupils, which produces a strongly shift variant PSF. This result will be further developed in the context of statistical optics in Chap. 3.

2.3.1 3D pupil formulation

The geometry of the system under consideration is shown in Fig. 2-22. Two positive lenses construct a 4–f system in which two lenses share the same focal plane [5]. The shared focal plane is the Fourier plane of the system; the volume hologram is located at the Fourier plane. The input plane of the system is the front focal plane of the first lens, and the output plane is the back focal plane of the second lens. The focal lengths of the two lenses are f_1 and f_2. The goal of this section is to derive the transfer function between the input field $p(x, y)$ and output field $q(x', y')$. Since the volume hologram at the Fourier plane has a finite longitudinal extent, the volumetric field near the Fourier plane should be considered, which is computed as

$$P(x'', y'', z'') = \exp\left\{i2\pi\frac{z''}{\lambda_p}\right\} \iint p(x, y) \exp\left\{-i2\pi\frac{xx'' + yy''}{\lambda_p f_1}\right\} \times \exp\left\{-i\pi\frac{x^2 + y^2}{\lambda_p f_1^2} z''\right\} \mathrm{d}x\mathrm{d}y, \tag{2.41}$$

where λ_p is the wavelength of a probe beam. The refractive index of a volume hologram is defined as

$$\epsilon(x'', y'', z'') = \epsilon_0 \exp\left\{i\mathbf{K}_{\mathrm{g}} \cdot \mathbf{r}''\right\} s(x'', y'', z''), \tag{2.42}$$

where $\mathbf{r}'' \equiv (x'', y'', z'')$ is the Cartesian coordinate vector, ϵ_0 is the baseband of refractive index modulation which is assumed to be constant in this case, $\mathbf{K}_{\mathrm{g}}$ is a grating vector, and $s(x'', y'', z'')$ describes physical dimensions of the volume hologram [27].

According to the 1st-order Born approximation [8], the secondary scattering is small and these terms are ignored. Then the modulated refractive index is illuminated by $P(x'', y'', z'')$ as

$$g(x'', y'', z'') = \epsilon(x'', y'', z'')P(x'', y'', z'') \tag{2.43}$$

at each point (x'', y'', z'') inside the volume hologram. The output field is

$$g_b(x''', y''', z''') = \iiint_V g(x'', y'', z'')G(x''' - x'', y''' - y'', z''' - z'')\mathrm{d}x''\mathrm{d}y''\mathrm{d}z'', \tag{2.44}$$

where V indicates the region inside the volume hologram, $G(x, y, z)$ is the Green's function which describes a point scatterer, and (x''', y''', z''') are the Cartesian coordinate at an arbitrary plane behind the volume hologram. The most convenient choice for z''' is $z''' = f_2$ since a collector lens is located at the focal distance. The field at the output plane, the back focal plane of the collector lens, is given by the Fourier transform of the field $q(x''', y''', f_2)$ as

$$q(x', y') = \exp\left\{i\pi\frac{x'^2 + y'^2}{\lambda f_2}\right\} \iint \exp\left\{-i2\pi\frac{x'x''' + y'y'''}{\lambda f_2}\right\} g_b(x''', y''', f_2)\mathrm{d}x'''\mathrm{d}y'''. \tag{2.45}$$

By assuming that the paraxial approximation is valid and combining eq. (2.44) and (2.45), eq. (2.43) becomes

$$\begin{aligned} q(x', y') = \iint g(x'', y'', z'') \exp\left\{-i2\pi\frac{x'x'' + yy''}{\lambda_p f_2}\right\} \\ \times \exp\left\{-i2\pi\left(1 - \frac{x'^2 + y'^2}{2f_2^2}\right)\frac{z''}{\lambda_p}\right\}\mathrm{d}x''\mathrm{d}y''\mathrm{d}z''. \end{aligned} \tag{2.46}$$

Inserting eq. (2.41) into eq. (2.46), we obtain quintuple integrals. Interchanging the integration order and performing the triple integrals of dx'', dy'', and dz'', the output field is obtained as

$$\begin{aligned} q(x', y') &= \iint p(x, y)\mathrm{d}x\mathrm{d}y \\ &\times \left[\iiint \epsilon(x'', y'', z'') \exp\left\{-i\frac{2\pi}{\lambda_p}\left(\frac{x}{f_1} + \frac{x'}{f_2}\right)x''\right\} \exp\left\{-i\frac{2\pi}{\lambda_p}\left(\frac{y}{f_1} + \frac{y'}{f_2}\right)y''\right\}\right. \\ &\left.\times \exp\left\{-i\frac{\pi}{\lambda_p}\left(\frac{x^2 + y^2}{f_1^2} - \frac{x'^2 + y'^2}{f_2^2}\right)z''\right\}\mathrm{d}x''\mathrm{d}y''\mathrm{d}z''\right] \\ &= \iint p(x, y)\mathcal{E}\left[\frac{1}{\lambda_p}\left(\frac{x}{f_1} + \frac{x'}{f_2}\right), \frac{1}{\lambda_p}\left(\frac{y}{f_1} + \frac{y'}{f_2}\right), \frac{1}{\lambda_p}\left(\frac{x^2 + y^2}{2f_1^2} - \frac{x'^2 + y'^2}{2f_2^2}\right)\right]\mathrm{d}x\mathrm{d}y, \end{aligned} \tag{2.47}$$

where $\mathcal{E}(u, v, w)$ is the 3D spatial Fourier transform of the refractive index $\epsilon(x'', y'', z'')$. Equation (2.47) can be understood in terms of input-output relations as

$$q(x', y') = \iint p(x, y)h(x', y'; x, y)\mathrm{d}x\mathrm{d}y, \tag{2.48}$$

where $h(x', y'; x, y)$ is the shift variant impulse response.

Note that $\mathcal{E}\left[\frac{1}{\lambda_p}\left(\frac{x}{f_1} + \frac{x'}{f_2}\right), \frac{1}{\lambda_p}\left(\frac{y}{f_1} + \frac{y'}{f_2}\right), \frac{1}{\lambda_p}\left(\frac{x^2+y^2}{2f_1^2} - \frac{x'^2+y'^2}{2f_2^2}\right)\right]$ is a 2D manifold of

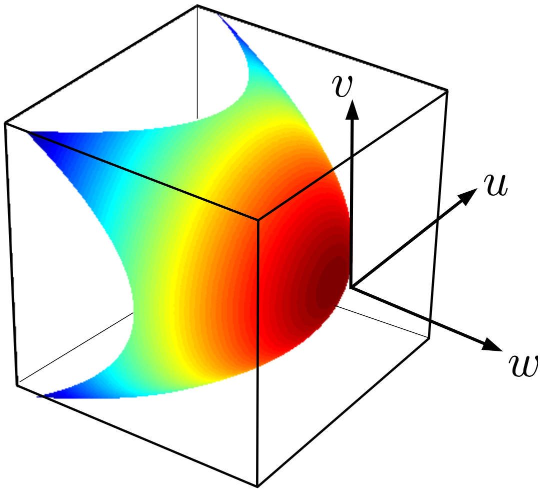

Figure 2-23: Shape of the 2D manifold of $\mathcal{E}(u, v, w)$

$\mathcal{E}(u, v, w)$, shown in Fig. 2-23. In traditional 4–f systems without volume holograms, the field PSF is the 2D Fourier transform of the 2D pupil function [5], whereas the PSF of the 4–f VHI system is the 2D manifold of the 3D Fourier transform of the 3D pupil function. This additional dimensionality introduces shift variance to systems.

2.3.2 Slab–shaped holograms

In practice, a slab–shaped hologram recorded by two plane waves is often used; it is interesting to examine in more detail. In this Section, the previously derived result is applied to the slab–shaped hologram and the point spread function is examined. The dimension of the hologram is $a \times b \times L$ depicted in Fig. 2-22. Denoting $E_{\mathrm{f}}(x'', y'', z'')$ and $E_{\mathrm{s}}(x'', y'', z'')$ as the reference and signal wave, respectively, where

$$E_{\mathrm{f}}(x'', y'', z'') = \exp\left\{-i\frac{2\pi}{\lambda_f}z''\right\}, \quad \text{and} \tag{2.49}$$

$$E_{\mathrm{s}}(x'', y'', z'') = \exp\left\{-i\frac{2\pi}{\lambda_f}\left(\theta_s x'' + \left[1 - \frac{\theta_s^2}{2}\right] z''\right)\right\}, \tag{2.50}$$

the 3D pupil function is computed as

$$\epsilon(x'', y'', z'') = \epsilon_0 \exp\left\{ i\frac{2\pi}{\lambda}\left(\theta_s x'' - \frac{\theta_s^2}{2} z''\right)\right\} \operatorname{rect}\left(\frac{x''}{a}\right) \operatorname{rect}\left(\frac{y''}{b}\right) \operatorname{rect}\left(\frac{z''}{L}\right), \tag{2.51}$$

and the 3D spatial Fourier transform of the 3D pupil is obtained as

$$\mathcal{E}(u, v, w) = \epsilon_0 abL \operatorname{sinc}\left\{ a\left(u - \frac{\theta_s}{\lambda_f}\right)\right\} \operatorname{sinc}\{bv\} \operatorname{sinc}\left\{ L\left(w + \frac{\theta_s^2}{2\lambda_f}\right)\right\}. \tag{2.52}$$

The output field is expressed as

$$\begin{aligned} q(x', y') = \epsilon_0 abL \iint p(x, y) \operatorname{sinc}\left\{ a\left(\frac{x}{\lambda_p f_1} + \frac{x'}{\lambda_p f_2} - \frac{\theta_s}{\lambda_f}\right)\right\} \operatorname{sinc}\left\{ \frac{b}{\lambda_p}\left(\frac{y}{f_1} + \frac{y'}{f_2}\right)\right\} \\ \times \operatorname{sinc}\left\{ \frac{L}{2}\left(\frac{x^2 + y^2}{\lambda_p f_1^2} - \frac{x'^2 + y'^2}{\lambda_p f_2^2} + \frac{\theta_s^2}{\lambda_f}\right)\right\} \mathrm{d}x\mathrm{d}y, \end{aligned} \tag{2.53}$$

where the shift variant impulse response is

$$\begin{aligned} h(x', y'; x, y) = \operatorname{sinc}\left\{ a\left(\frac{x}{\lambda_p f_1} + \frac{x'}{\lambda_p f_2} - \frac{\theta_s}{\lambda_f}\right)\right\} \operatorname{sinc}\left\{ b\left(\frac{y}{\lambda_p f_1} + \frac{y'}{\lambda_p f_2}\right)\right\} \\ \times \operatorname{sinc}\left\{ \frac{L}{2}\left(\frac{x^2 + y^2}{\lambda_p f_1^2} - \frac{x'^2 + y'^2}{\lambda_p f_2^2} + \frac{\theta_s^2}{\lambda_f}\right)\right\}. \end{aligned} \tag{2.54}$$

The first two sinc functions are caused by the rectangular aperture of the volume hologram, which indicates the Gaussian image point as in traditional imaging systems. The third sinc function results from the longitudinal extent of the volume hologram, which makes the system strongly shift variant.

2.3.3 Discussion

The general form of the point spread function of VHI system has been derived by using scalar diffraction theory. Specifically, the VHI system with a slab shape hologram is examined in detail. Since the pupil function of the VHI systems is a 3D function due to the volume hologram, the point spread function is the 3D Fourier transform of the pupil function, as expected. The PSF of the VHI system will be used in Chapter 3 and

4. Although this formulation represents the system characteristics in great detail, it is difficult to include the aberrations and to analyze volume holograms with complicated refractive index modulations. A more detailed analysis including OTF can be found in Ref. [27].

In terms of numerical computation of volume diffraction, this 3D Fourier transform method is more straightforward than the one used in Ref. [7, 14], in which the volume diffraction is computed by the Lommel function [37]. This Lommel function based approach is slow due to numerical integrations; pre–computed lookup tables and interpolation can speed up the computation time [38]. The 3D Fourier transform method described in this section requires huge computational resources to compute the 3D Fourier transform; it is implemented in Ref. [36].

2.4 Conclusion

Two frameworks of volume diffraction have been presented: the k–sphere and Fourier optics method. In Sec. 2.1, the k–sphere method was integrated into a ray tracing software, which allows the use of built–in analysis and optimization tools; this implementation brings great advantages and versatility to the design process. The most important feature is the capability to simulate shift variant volume holograms efficiently. The feasibility of the implemented method was demonstrated with three examples: calculating the longitudinal point spread function, exploiting the effect of aberrations, and optimizing an objective lens to obtain higher Bragg diffraction efficiency. Specifically, the effects of aberrations have not been considered in earlier research. They may be even positive, e.g., potentially improving the depth selectivity of VHI system, as demonstrated. Multiplexed holograms can be modeled with multi–configuration features in ZEMAX®, however, the crosstalk between holograms are not taken into account. To include absolute diffraction efficiency, more rigorous analysis such as coupled mode theory [39] should be included.

In Sec. 2.2, the k–sphere analysis has been extended in 3D space. Considering out–of–plane probe beams, curved Bragg diffraction images were observed. Analytical expression of the curved shape is presented, resulting a distorted ellipse, in general.

In Sec. 2.3, the scalar diffraction theory for volume diffractions in VHI systems was revisited. By including the effect of the finite longitudinal extent of the volume hologram, the general form of the field PSF was derived, which is the 3D Fourier transform of the 3D pupil. This result revealed the shift variant nature of the VHI system and will be further developed using statistical optics in Chap. 3 and in Wigner space in Chap. 4.

Chapter 3

Volume holographic imaging systems in statistical optics

This chapter extends the analysis of VHI systems into statistical optics. By using coherence theory, the partially coherent responses of VHI systems are derived. As an application of the partially coherent responses, a passive depth detection method is particularly interesting, which is a special case of multi–dimensional imaging. A new passive depth detection method based on spatial coherence is proposed by assuming spatially incoherent objects and binarizing the depth. Theoretical analysis and experimental verification for quasi–monochromatic, spatially incoherent light are presented. Later, the system is improved to be operated under broad illumination and its binary depth resolving capability for featureless white uniform objects is demonstrated.

3.1 Partially coherent response of VHI

3.1.1 Coherence function response of general VHI systems

The response of the volume holographic imaging system of Fig. 2-22 to partially coherent illumination is derived. The input plane is the front focal plane of the first lens, and the output plane is the back focal plane of the second lens. The input and output planes are represented by Cartesian coordinates (x, y) and (x', y'), respectively.

The imaging system of Fig. 2-22 is probed by a quasi–monochromatic, partially coherent field expressed in phasor notation as

$$P(x,y,t) = Re\left\{p(x,y)e^{-j\omega_{\mathrm{p}}t}\right\}, \tag{3.1}$$

where $p(x,y)$ is the complex amplitude and ω_p is the frequency of the field. We use lower cases for phasors and capitals for time–varying oscillatory signals. The mean probe wavelength is $\lambda_{\mathrm{p}} = 2\pi c/\omega_{\mathrm{p}}$.

Let $Q(x',y',t)$ denote the field at the output plane. The mutual coherence function of the input and output fields are, respectively, [40]:

$$\begin{aligned} \mathbf{\Gamma}_{\mathrm{P}}(x_1,y_1,x_2,y_2,\tau) &= \langle P(x_1,y_1,t+\tau)P^*(x_2,y_2,t)\rangle, \quad \text{and} && (3.2)\\ \mathbf{\Gamma}_{\mathrm{Q}}(x_1',y_1',x_2',y_2',\tau) &= \langle Q(x_1',y_1',t+\tau)Q^*(x_2',y_2',t)\rangle, && (3.3) \end{aligned}$$

where $\langle\ \rangle$ indicates ensemble average and τ denotes time delay. Using the ergodicity and quasi–monochromaticity assumptions, the coherence function is sufficiently described by the mutual intensity $\mathbf{J}$, defined as the mutual coherence at zero time delay:

$$\begin{aligned} \mathbf{J}_{\mathrm{p}}(x_1,y_1,x_2,y_2) &= \langle p(x_1,y_1)p^*(x_2,y_2)\rangle, \quad \text{and} && (3.4)\\ \mathbf{J}_{\mathrm{q}}(x_1',y_1',x_2',y_2') &= \langle q(x_1',y_1')q^*(x_2',y_2')\rangle. && (3.5) \end{aligned}$$

In the special case of spatially coherent input $p(x,y)$, the impulse response has been derived in Sec. 2.3.1 as

$$\begin{aligned} q(x',y') = \iint \mathrm{d}x\mathrm{d}y\ p(x,y) \\ \times\,\mathcal{E}\left[\frac{1}{\lambda_p}\left(\frac{x}{f_1}+\frac{x'}{f_2}\right), \frac{1}{\lambda_p}\left(\frac{y}{f_1}+\frac{y'}{f_2}\right), \frac{1}{\lambda_p}\left(\frac{x^2+y^2}{2f_1^2}-\frac{x'^2+y'^2}{2f_2^2}\right)\right], \end{aligned} \tag{3.6}$$

where $\mathcal{E}$ is the 3D Fourier transform of the 3D pupil function. Applying the mutual coherence function definition, we obtain

$$\begin{aligned}\mathbf{\Gamma}_{\mathrm{Q}}(x_1', y_1', x_2', y_2', \tau) = \iiiint & \mathrm{d}x_1\mathrm{d}x_2\mathrm{d}y_1\mathrm{d}y_2 \; \mathbf{\Gamma}_{\mathrm{P}}(x_1, y_1, x_2, y_2, \tau) \\ \times\, \mathcal{E}&\left[\frac{1}{\lambda_p}\left(\frac{x_1}{f_1}+\frac{x_1'}{f_2}\right), \frac{1}{\lambda_p}\left(\frac{y_1}{f_1}+\frac{y_1'}{f_2}\right), \frac{1}{\lambda_p}\left(\frac{x_1^2+y_1^2}{2f_1^2}-\frac{x_1'^2+y_1'^2}{2f_2^2}\right)\right] \\ \times\, \mathcal{E}^*&\left[\frac{1}{\lambda_p}\left(\frac{x_2}{f_1}+\frac{x_2'}{f_2}\right), \frac{1}{\lambda_p}\left(\frac{y_2}{f_1}+\frac{y_2'}{f_2}\right), \frac{1}{\lambda_p}\left(\frac{x_2^2+y_2^2}{2f_1^2}-\frac{x_2'^2+y_2'^2}{2f_2^2}\right)\right].\end{aligned} \tag{3.7}$$

By letting $\tau = 0$, the mutual intensity response is found as

$$\begin{aligned}\mathbf{J}_{\mathrm{q}}(x_1', y_1', x_2', y_2') = \iiiint & \mathrm{d}x_1\mathrm{d}x_2\mathrm{d}y_1\mathrm{d}y_2 \; \mathbf{J}_{\mathrm{p}}(x_1, y_1, x_2, y_2) \\ \times\, \mathcal{E}&\left[\frac{1}{\lambda_p}\left(\frac{x_1}{f_1}+\frac{x_1'}{f_2}\right), \frac{1}{\lambda_p}\left(\frac{y_1}{f_1}+\frac{y_1'}{f_2}\right), \frac{1}{\lambda_p}\left(\frac{x_1^2+y_1^2}{2f_1^2}-\frac{x_1'^2+y_1'^2}{2f_2^2}\right)\right] \\ \times\, \mathcal{E}^*&\left[\frac{1}{\lambda_p}\left(\frac{x_2}{f_1}+\frac{x_2'}{f_2}\right), \frac{1}{\lambda_p}\left(\frac{y_2}{f_1}+\frac{y_2'}{f_2}\right), \frac{1}{\lambda_p}\left(\frac{x_2^2+y_2^2}{2f_1^2}-\frac{x_2'^2+y_2'^2}{2f_2^2}\right)\right].\end{aligned} \tag{3.8}$$

The intensity distribution on the output plane can be found as eq. (3.14) by letting $x_2' = x_1' = x'$ and $y_2' = y_1' = y'$:

$$\begin{aligned}I_q(x', y') = \iiiint & \mathrm{d}x_1\mathrm{d}x_2\mathrm{d}y_1\mathrm{d}y_2 \; \mathbf{J}_{\mathrm{p}}(x_1, y_1, x_2, y_2) \\ \times\, \mathcal{E}&\left[\frac{1}{\lambda_p}\left(\frac{x_1}{f_1}+\frac{x'}{f_2}\right), \frac{1}{\lambda_p}\left(\frac{y_1}{f_1}+\frac{y'}{f_2}\right), \frac{1}{\lambda_p}\left(\frac{x_1^2+y_1^2}{2f_1^2}-\frac{x_1'^2+y'^2}{2f_2^2}\right)\right] \\ \times\, \mathcal{E}^*&\left[\frac{1}{\lambda_p}\left(\frac{x_2}{f_1}+\frac{x'}{f_2}\right), \frac{1}{\lambda_p}\left(\frac{y_2}{f_1}+\frac{y'}{f_2}\right), \frac{1}{\lambda_p}\left(\frac{x_2^2+y_2^2}{2f_1^2}-\frac{x'^2+y'^2}{2f_2^2}\right)\right].\end{aligned} \tag{3.9}$$

3.1.2 VHI system with a slab-shaped volume hologram

Next, we consider a slab–shaped hologram as in Sec. 2.3.2. The dimensions are $a \times b \times L$ and the hologram is recorded by two mutually coherent plane waves. The refractive index modulation in the paraxial approximation is

$$\epsilon(x'', y'', z'') = \epsilon_0 \exp\left\{ i\frac{2\pi}{\lambda_{\mathrm{f}}}\left(\theta_{\mathrm{s}}x'' - \frac{\theta_{\mathrm{s}}^2}{2}z''\right)\right\} \mathrm{rect}\left(\frac{x''}{a}\right) \mathrm{rect}\left(\frac{y''}{b}\right) \mathrm{rect}\left(\frac{z''}{L}\right), \tag{3.10}$$

where ϵ_0 is a constant, and (x'', y'', z'') are the Cartesian coordinates in the vicinity of the pupil. The response for a spatially coherent input $p(x, y)$ is given by

$$q(x', y') = \epsilon_0 abL \iint \mathrm{d}x\mathrm{d}y\ p(x, y)\mathrm{sinc}\left\{a\left(\frac{x}{\lambda_\mathrm{p} f_1} + \frac{x'}{\lambda_\mathrm{p} f_2} - \frac{\theta_\mathrm{s}}{\lambda_\mathrm{f}}\right)\right\}$$
$$\times\ \mathrm{sinc}\left\{\frac{b}{\lambda_\mathrm{p}}\left(\frac{y}{f_1} + \frac{y'}{f_2}\right)\right\} \mathrm{sinc}\left\{\frac{L}{2}\left(\frac{x^2 + y^2}{\lambda_\mathrm{p} f_1^2} - \frac{x'^2 + y'^2}{\lambda_\mathrm{p} f_2^2} + \frac{\theta_\mathrm{s}^2}{\lambda_\mathrm{f}}\right)\right\}. \quad (3.11)$$

Using the same procedure presented in Sec. 3.1.1, the transfer function of mutual coherence, mutual intensity, and intensity are obtained as follows:

$$\mathbf{\Gamma}_\mathrm{Q}(x_1', y_1', x_2', y_2', \tau) = \epsilon_0^2 (abL)^2 \iiiint \mathrm{d}x_1\mathrm{d}x_2\mathrm{d}y_1\mathrm{d}y_2\ \mathbf{\Gamma}_\mathrm{P}(x_1, y_1, x_2, y_2, \tau)$$
$$\times\ \mathrm{sinc}\left\{a\left(\frac{x_1}{\lambda_\mathrm{p} f_1} + \frac{x_1'}{\lambda_\mathrm{p} f_2} - \frac{\theta_\mathrm{s}}{\lambda_\mathrm{f}}\right)\right\} \mathrm{sinc}\left\{a\left(\frac{x_2}{\lambda_\mathrm{p} f_1} + \frac{x_2'}{\lambda_\mathrm{p} f_2} - \frac{\theta_\mathrm{s}}{\lambda_\mathrm{f}}\right)\right\}$$
$$\times\ \mathrm{sinc}\left\{b\left(\frac{y_1}{\lambda_\mathrm{p} f_1} + \frac{y_1'}{\lambda_\mathrm{p} f_2}\right)\right\} \mathrm{sinc}\left\{b\left(\frac{y_2}{\lambda_\mathrm{p} f_1} + \frac{x_2'}{\lambda_\mathrm{p} f_2}\right)\right\}$$
$$\times\ \mathrm{sinc}\left\{\frac{L}{2}\left(\frac{x_1^2 + y_1^2}{\lambda_\mathrm{p} f_1^2} - \frac{x_1'^2 + y_1'^2}{\lambda_\mathrm{p} f_2^2} + \frac{\theta_\mathrm{s}^2}{\lambda_\mathrm{f}}\right)\right\} \mathrm{sinc}\left\{\frac{L}{2}\left(\frac{x_2^2 + y_2^2}{\lambda_\mathrm{p} f_1^2} - \frac{x_2'^2 + y_2'^2}{\lambda_\mathrm{p} f_2^2} + \frac{\theta_\mathrm{s}^2}{\lambda_\mathrm{f}}\right)\right\},$$
$$(3.12)$$

$$\mathbf{J}_\mathrm{q}(x_1', y_1', x_2', y_2') = \epsilon_0^2 (abL)^2 \iiiint \mathrm{d}x_1\mathrm{d}x_2\mathrm{d}y_1\mathrm{d}y_2\ \mathbf{J}_\mathrm{p}(x_1, y_1, x_2, y_2)$$
$$\times\ \mathrm{sinc}\left\{a\left(\frac{x_1}{\lambda_\mathrm{p} f_1} + \frac{x_1'}{\lambda_\mathrm{p} f_2} - \frac{\theta_\mathrm{s}}{\lambda_\mathrm{f}}\right)\right\} \mathrm{sinc}\left\{a\left(\frac{x_2}{\lambda_\mathrm{p} f_1} + \frac{x_2'}{\lambda_\mathrm{p} f_2} - \frac{\theta_\mathrm{s}}{\lambda_\mathrm{f}}\right)\right\}$$
$$\times\ \mathrm{sinc}\left\{b\left(\frac{y_1}{\lambda_\mathrm{p} f_1} + \frac{y_1'}{\lambda_\mathrm{p} f_2}\right)\right\} \mathrm{sinc}\left\{b\left(\frac{y_2}{\lambda_\mathrm{p} f_1} + \frac{y_2'}{\lambda_\mathrm{p} f_2}\right)\right\}$$
$$\times\ \mathrm{sinc}\left\{\frac{L}{2}\left(\frac{x_1^2 + y_1^2}{\lambda_\mathrm{p} f_1^2} - \frac{x_1'^2 + y_1'^2}{\lambda_\mathrm{p} f_2^2} + \frac{\theta_\mathrm{s}^2}{\lambda_\mathrm{f}}\right)\right\} \mathrm{sinc}\left\{\frac{L}{2}\left(\frac{x_2^2 + y_2^2}{\lambda_\mathrm{p} f_1^2} - \frac{x_2'^2 + y_2'^2}{\lambda_\mathrm{p} f_2^2} + \frac{\theta_\mathrm{s}^2}{\lambda_\mathrm{f}}\right)\right\},$$
$$(3.13)$$

and

$$
\begin{aligned}
I_q(x',y') = \epsilon_0^2(abL)^2 & \iiiint \mathrm{d}x_1\mathrm{d}x_2\mathrm{d}y_1\mathrm{d}y_2\ \mathbf{J}_{\mathrm{p}}(x_1,y_1,x_2,y_2) \\
& \times \operatorname{sinc}\left\{a\left(\frac{x_1}{\lambda_{\mathrm{p}}f_1}+\frac{x'}{\lambda_{\mathrm{p}}f_2}-\frac{\theta_{\mathrm{s}}}{\lambda_{\mathrm{f}}}\right)\right\}\operatorname{sinc}\left\{a\left(\frac{x_2}{\lambda_{\mathrm{p}}f_1}+\frac{x'}{\lambda_{\mathrm{p}}f_2}-\frac{\theta_{\mathrm{s}}}{\lambda_{\mathrm{f}}}\right)\right\} \\
& \times \operatorname{sinc}\left\{b\left(\frac{y_1}{\lambda_{\mathrm{p}}f_1}+\frac{y'}{\lambda_{\mathrm{p}}f_2}\right)\right\}\operatorname{sinc}\left\{b\left(\frac{y_2}{\lambda_{\mathrm{p}}f_1}+\frac{y'}{\lambda_{\mathrm{p}}f_2}\right)\right\} \\
& \times \operatorname{sinc}\left\{\frac{L}{2}\left(\frac{x_1^2+y_1^2}{\lambda_{\mathrm{p}}f_1^2}-\frac{x'^2+y'^2}{\lambda_{\mathrm{p}}f_2^2}+\frac{\theta_{\mathrm{s}}^2}{\lambda_{\mathrm{f}}}\right)\right\}\operatorname{sinc}\left\{\frac{L}{2}\left(\frac{x_2^2+y_2^2}{\lambda_{\mathrm{p}}f_1^2}-\frac{x'^2+y'^2}{\lambda_{\mathrm{p}}f_2^2}+\frac{\theta_{\mathrm{s}}^2}{\lambda_{\mathrm{f}}}\right)\right\}.
\end{aligned}
\tag{3.14}
$$

In eqs. (3.13) and (3.14), the first four sinc functions correspond to the standard lateral point spread function of a finite–aperture hologram [5], whereas the last two sinc functions express the Bragg selectivity of the volume grating. The spatial coherence at the output plane can be computed with this formulation; i.e., for a given degree of coherence at the input plane, we can compute the spatial coherence at the output plane.

3.2 Passive binary depth detection system

As an application of the partially coherent response of the VHI system, passive depth imaging is particularly interesting, which is a special case of multi–dimensional imaging. By exploiting the volume holographic pupils and binarizing the imaging scenario, a passive binary depth detection system is implemented.

3.2.1 Introduction

Depth ranging is one of the primary applications in optical metrology, and it can be categorized as active or passive depending on the requirement of specifically modulated illumination [41]. In active methods, objects are illuminated by spatially or temporally modulated light, and depth information is obtained from decoding the reflected or scattered light. LIDAR [42], confocal microscopy [43], rainbow volume holographic profilometry [24], photometric stereo [44], and 3D photography using shadows [45] are representative examples of active methods. Active methods can easily achieve high resolution in depth, hence they are extensively being used in task based imaging such as product inspection; however, active imaging is less desirable in adversarial imaging scenarios (e.g., military reconnaissance).

Instead of using specific illumination, passive methods rely on changes of object features as a function of depth with respect to a known depth–dependent imaging kernel. Stereo vision or camera array systems use additional cameras to obtain different perspectives [46, 47]. Depth from focus/defocus monitors variations of blur in sharp edges [48, 49]. An alternative elegant approach is to use a phase mask implementing a depth–dependent OTF or PSF with *a priori*–known information about the target [50]. For passive methods in general, unless enough change of the object features occurs with depth, the detection is not guaranteed to have accurate results.

We have worked on volume holographic imaging during the past few years; a new multi–dimensional imaging technique which exploits angular/wavelength selectivity of volume holograms to achieve depth discrimination [7, 15–17, 23, 24, 51]. All our prior works were based on active methods detecting irradiance at the output plane using a standard array of photodetectors (e.g., a CCD camera). It was shown recently that extending the volume holographic imaging to passive (spatially incoherent illumination) provides no depth discrimination capability if classical detection is used [38].

In this section, a new method is implemented to resolve the limitation of passive depth measurements by cascading a spatial coherence measurement system after the volume holographic imager. Spatial coherence is measured by the cross–correlation of a random light field and it changes with light propagation distance and source size. Among many applications of spatial coherence to imaging, a notable one is coherence imaging [52–56], which is appropriate for passive 3D imaging. The idea is based on the van Cittert–Zernike theorem [57, 58], which states that the spatial coherence function is a 2D spatial Fourier transform of the intensity distribution of a quasi–monochromatic incoherent source. This is generalized to 3D by incorporating the quadratic phase function due to Fresnel propagation in the proof of the van Cittert–Zernike theorem [53, 55]. Therefore, measuring the 3D spatial coherence

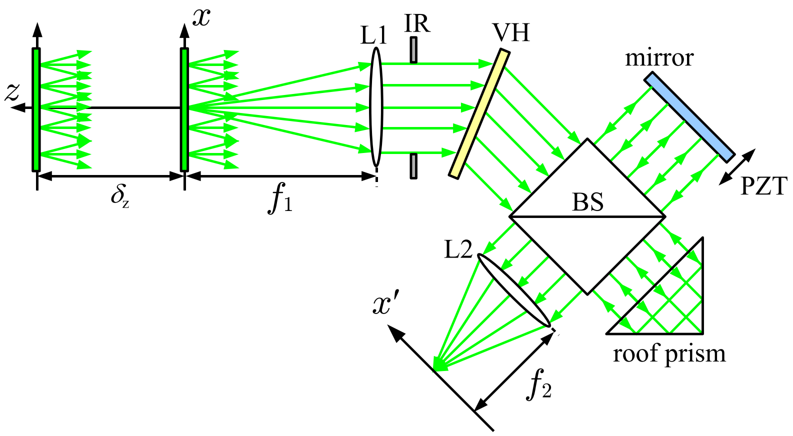

Figure 3-1: The schematic of the experimental setup. IR: variable iris, VH: volume hologram, L1,L2: lenses, M: mirror, RP: roof–prism, BS: beam splitter, PZT: piezo stage.

function allows purely passive 3D imaging. However, the applicability of this method in practice is limited due to the small fringe visibility of interference in coherence measurements [59].

To overcome the fringe visibility limitation, we propose to binarize the problem, i.e., detect whether the object is within the depth of field of the imaging system or not. Even though we sacrifice depth resolution with this approach, discrimination of two depths is still very useful for a variety of applications such as replacing blue screen matting [60–64]. By repeating a sequence of similar binary measurements, each with a different focal distance, one can in principle recover finer depth resolution, albeit with an increased acquisition time.

3.2.2 Passive Depth Detection by Spatial Coherence

In this section, it is explained how to discriminate two objects at different depths based on the previously derived coherence response of VHI systems. Interferometric measurement is necessary to utilize coherence nature of light and partially coherent response. To implement it, we cascaded a wavefront folding interferometer [56] to a VHI telescope as shown in Fig. 3-1. The volume holographic imager consists of an objective, collector and volume hologram. Bragg diffracted light is then directed to a wavefront folding interferometer, which has a planar mirror and roof prism to generate mirror–flip shear [56]. The shear is parallel to the Bragg selectivity direction. A piezo actuator is installed on the planar mirror to modulate the optical path difference.

The system of Fig. 3-1 measures the mutual intensity of the output field. $\mathbf{J}_{\mathrm{q}}$ is an indirect measurement of the desired quantity $\mathbf{J}_{\mathrm{p}}$, the mutual intensity of the input field, which carries depth information [53, 55]. According to eq. (3.13), the relationship between $\mathbf{J}_{\mathrm{q}}$ and $\mathbf{J}_{\mathrm{p}}$ is a convolution with narrowed sinc kernels, whose width is determined by the hologram dimensions a, b, and L. Despite the blur introduced to the measurement by the convolution, binary depth detection for extended objects is still possible based on the measurement of $\mathbf{J}_{\mathrm{p}}$.

Since the imaging scenario is binarized, there are only two depths. The foreground (FG) object is assumed to be located at the input plane, i.e., the focal plane of the objective lens (or near the focal plane, as long as it is within the depth of field). The background (BG) object is located at a distance δ_z away from the input plane, assumed to be larger than the depth of field, away from the input plane. We assume that both objects radiate quasi–monochromatic and spatially incoherent fields and their intensity I_0 is uniform.

For the FG object, by the definition of the incoherent source [40], the mutual intensity is written as

$$\mathbf{J}_{\mathrm{p,FG}}(x_1, y_1, x_2, y_2) = I_0 \delta(\Delta x, \Delta y), \tag{3.15}$$

where $\Delta x = x_2 - x_1$ and $\Delta y = y_2 - y_1$.

For the BG object, even though the object itself is spatially incoherent, the field at the input plane becomes partially coherent due to the propagation by δ_z according to the van Cittert–Zernike theorem [40]. Hence, the mutual intensity at the input plane is computed as

$$\mathbf{J}_{\mathrm{p,BG}}(x_1, y_1; x_2, y_2) = \frac{1}{(\lambda_{\mathrm{p}}\delta_z)^2} \exp\left\{-j\frac{2\pi}{\lambda_{\mathrm{p}}\delta_z}\left(x_2^2 + y_2^2 - x_1^2 - y_1^2\right)\right\} \\ \times \iint I_s(\xi, \eta) \exp\left\{-j\frac{2\pi}{\lambda_{\mathrm{p}}\delta_z}\left(\Delta x\xi + \Delta y\eta\right)\right\} \mathrm{d}\xi\mathrm{d}\eta, \quad (3.16)$$

where I_s is the intensity distribution of the BG object, and (ξ, η) are the spatial coordinates of the BG object. As eq. (3.16) indicates, at the input plane, the degree of coherence of the light from the BG object depends on the size of the BG object and the propagation distance δ_z. As the propagation distance increases, the degree of coherence is improved. Even though the infinitely extended source produces a completely incoherent field in principle, the effective maximum size of the BG object is determined by the NA of the system. Moreover, spatial frequencies outside the Bragg angular acceptance of the volume hologram are not diffracted and thus they do not contribute to the degree of coherence at the output plane. In practice, both the FG and BG objects may have non–uniform intensity distributions. In the volume holographic imaging system with quasi–monochromatic light, only a slit–like portion of the FG object is imaged due the Bragg selectivity [7]. The slit is oriented along the x–dimension, the same as the angular detuning of the roof prism in the interferometer (see Fig. 3-1). Thus, the intensity of the FG object can be considered locally uniform. However, for the BG object, a much larger area is imaged and if the intensity were non–uniform, it would increase the degree of coherence even further. Therefore, it is always true that the light arriving at the input plane from the BG object is more coherent than the FG object. The difference between the degree of coherence of the FG and BG fields is mapped to the degree of coherence at the output plane according to eq. (3.13). It follows that measuring spatial coherence at the output plane allows us to decide whether the object is at the FG or BG plane.

We now proceed to describe the operation of the cascaded wavefront folding interferometer in Fig. 3-1. The light diffracted by the volume holographic pupil is divided by the beam splitter. One of the split beams is reflected by the mirror and the other one is reflected by the roof–prism. The reflectivities of the mirror and the prism are assumed to be identical. If the output field coming from the mirror is denoted by $q(x', y')$ as in eq. (3.11), then the field returned by the prism is $q(-x', y')$ due to the spatial inversion (shear) by the prism. Hence, the intensity of the interference at the CCD is written as

$$\begin{aligned} I(x', y') &= |q(x', y')|^2 + |q(-x', y')|^2 + 2\mathrm{Re}\left\{q^*(x', y')q(-x', y')\right\} \\ &= |q(x', y')|^2 + |q(-x', y')|^2 + 2|\mathbf{J}_{\mathrm{q}}(x', y', -x', y')| \cos\left(\frac{2\pi}{\lambda_{\mathrm{p}}}d + \phi\right), \end{aligned} \tag{3.17}$$

where d is the optical path difference generated by the PZT actuator, and ϕ is the unknown phase of $\mathbf{J}_{\mathrm{q}}$. The fringe visibility is defined as

$$\mathcal{V}(x', y') = \frac{I_{\mathrm{max}}(x', y') - I_{\mathrm{min}}(x', y')}{I_{\mathrm{max}}(x', y') + I_{\mathrm{min}}(x', y')}, \tag{3.18}$$

where I_{max} and I_{min} are the maximum and minimum intensities, respectively. The complex coherence factor, or normalized mutual intensity, is

$$\mu(x', y', -x', y') = \frac{\mathbf{J}_{\mathrm{q}}(x', y', -x', y')}{|q(x', y')||q(-x', y')|}. \tag{3.19}$$

The magnitude of the complex coherence factor is equal to the fringe visibility [40]. Note that a CCD pixel at x' measures the spatial coherence between x' and $-x'$, which corresponds to a shear $\Delta x' = x' - (-x')$. As the CCD pixel distance away from the shearing center $x' = f_2\theta_{\mathrm{s}}$ increases, the visibility generally decreases. Near $\Delta x' = 0$, the field coherence is maximal, and larger intensity variations in intensity are observed as the PZT is dithered.

Figure 3-2 shows a raw image on the CCD camera (FastQcam 12–bit camera, Qcamera, Canada) and cross sections of the interference fringes along x' obtained experimentally for different longitudinal positions of the PZT. A slit–like image, approximately 70 pixels wide, is clearly observable in Fig. 3-2. This is due to the angular Bragg selectivity of the hologram. The slit is mostly invariant to PZT motion, except near the center where the field coherence is maximal, as noted earlier in the discus-

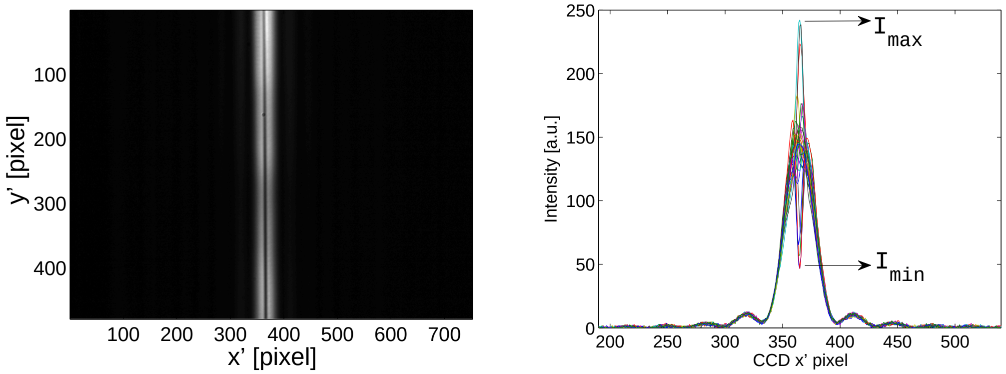

(a) CCD raw image at minimum peak intensity

(b) cross section of the intensity profile

Figure 3-2: Exemplary images from experiments. In (a), a raw image is plotted. In (b) 30 cross sections of the interference fringes along the x'–axis obtained from thirty corresponding longitudinal positions of the PZT actuator are plotted. Since the center part of the fringe is more spatially coherent, the interference fringes oscillate near the center but the oscillations die out away from the center where the field becomes incoherent.

sion of the result eq. (3.17). Ideally, the visibility at $\Delta x' = 0$ should be 1. However, because of the finite size of the CCD pixel [65, 66] and other practical reasons that will be described later, the visibility in experiments can be smaller than 1.

Next, the visibility of the interference fringes produced from the FG and BG objects is simulated. By using eqs. (3.15) and (3.16), eq. (3.13) was numerically integrated in MATLAB® and the visibility was computed, including the effect of vignetting of the system, finite CCD pixel size, and finite aperture size. Figure 3-3 shows the simulated visibility with various aperture sizes for a given CCD pixel size. The aperture dependence is explained because at the two extremes of vanishingly small and infinitely large aperture incoming fields become perfectly coherent and incoherent, respectively and, hence, cannot be discriminated; depth discrimination can be achieved only with partially coherent fields produced by an intermediate aperture. At the 25 mm aperture size and $\delta_z = 180$ mm, the visibility of the FG object is 0.4507 while the visibility of the BG object is 0.5221. The difference in visibility is 0.0714.

The dependence on pixel size is explained with the help of Fig. 3-4. A very small

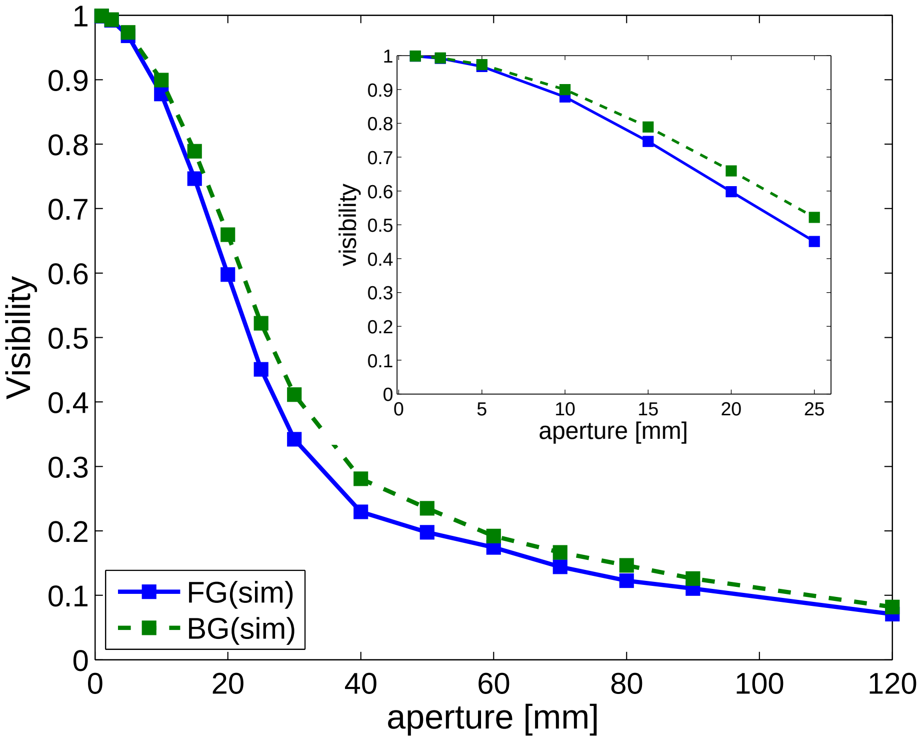

Figure 3-3: Simulation results of visibility and aperture size for the FG object (blue solid line) and the BG object (green dashed line), where $\delta_z = 150\,\text{mm}$, $\lambda = 532\,\text{nm}$, the CCD pixel size is $5 \times 5\,\mu\text{m}$, L=1.5 mm, $\theta_\text{s} = 30°$, and $f_1 = f_2 = 200\,\text{mm}$. *(Top right)* Zoom–in at small apertures.

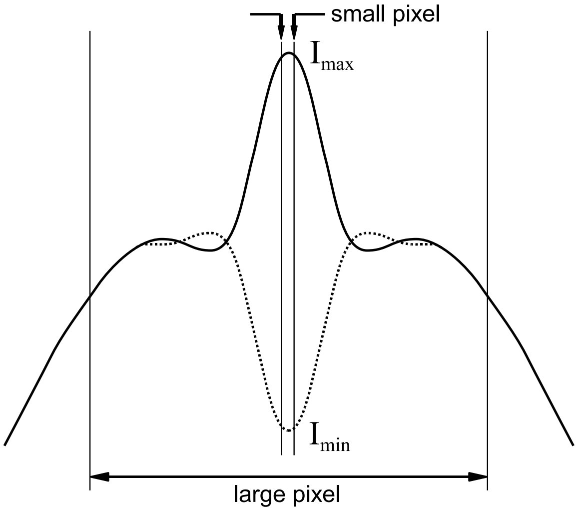

Figure 3-4: Zoom–in of Fig. 3-2. Discrimination ability is lost with pixels which are too small or too large.

pixel would sample only the coherent part of the field near $x' = 0$; on the other hand, the measurement with a very large pixel would be overwhelmed by the incoherent part of the field. An intermediate pixel size maximizes discrimination ability between FG and BG fields. The optimal CCD pixel size turns out to be approximately the lateral PSF of the imaging system preceding the interferometer, i.e., $\lambda f_2/a$, as one might have intuitively expected.

To verify the simulation result in our experiment, a rotational diffuser is placed at either the FG or the BG plane and illuminated by an expanded laser beam (a doubled Nd:YAG laser, $\bar{\lambda} = 532\,\text{nm}$). The fringe visibility for the two cases are compared, as shown in Fig. 3-5.

For the smallest aperture, the visibility is slightly larger than 0.8, while it is close to 1 in the simulations. The deviations between experiments and simulations are explained as follows: 1) Non–perfect optical surfaces of the beam splitter, planar mirror and prism, especially the vertex of the prism, generate wavefront distortion and degrade the visibility. 2) In practice, the reflectivity of the mirror and the prism are not identical. 3) Aberrations from the collector lens also result in lower visibility. These effects become more critical as the aperture increases.

In Fig. 3-5, the red dotted line is the experimental result with the laser only and

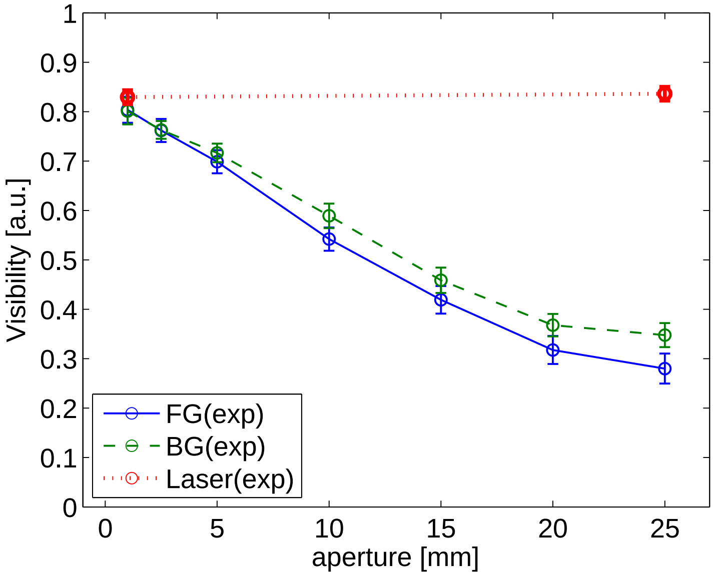

Figure 3-5: Experimental results of visibility and aperture size for the FG (blue solid line) and BG object (green dashed line), where $\delta_z = 180\,\mathrm{mm}$, $\lambda = 532\,\mathrm{nm}$, CCD pixel size of $5 \times 5\,\mu\mathrm{m}$. The red dotted line is the result with the laser only without using the rotational diffuser. Other parameters are identical to the simulation in Fig. 3-3.

without the rotating diffuser. This experiment indicates the maximum achievable visibility in the experimental setup, which is also approximately 0.8. Considering this offset, the experimental results are in good agreement with the simulations in Fig. 3-3. At the 25 mm aperture size, the visibility of the FG object is 0.2801 ± 0.0304 (mean ± standard deviation), while the visibility of the BG object is 0.3478 ± 0.0244. The visibility difference is 0.0677, while the relative difference is 19.47% at $\delta_z = 180\,\mathrm{mm}$.

To decide whether the imaged object is at the FG or BG plane according to our hypothesis, Bayesian estimation is performed [67], which minimizes the conditional decision error. Fig. 3-6 shows the histogram of the visibility of the experimental result at 25 mm aperture size in Fig. 3-5. The histograms plotted in Fig. 3-6 are assumed to be Gaussian probability density functions, and the optimum threshold $\mathcal{V}_{\mathrm{TH}}$ is computed. It is found to be 0.3175 with a false decision probability of 18%.

Next two objects are placed at the FG and BG planes simultaneously. The two objects were identical sheets of white, diffuse paper. A white light source with a band–pass filter (the center wavelength: 532 nm and bandwidth: 10 nm) was used to

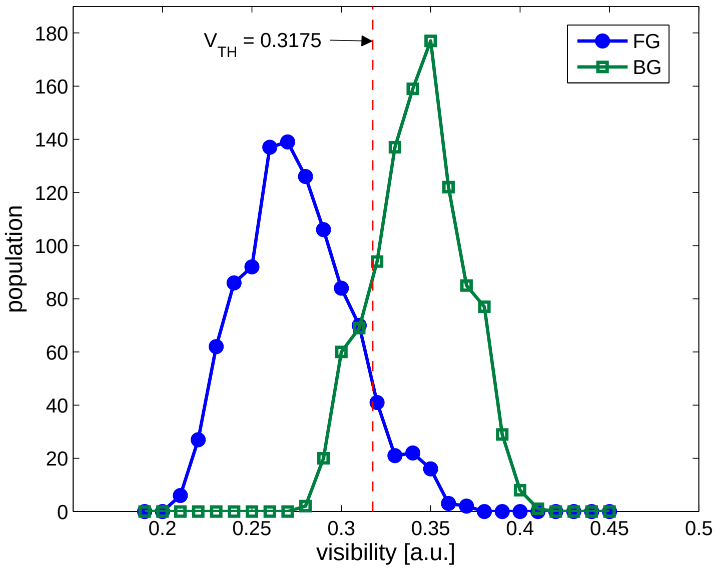

Figure 3-6: The histogram of the experimental result for the 25 mm aperture size of Fig. 3-5. The FG object (blue line with circles) and the BG object (green line with squares) are plotted together. The red dotted line indicates the best visibility threshold computed by Bayesian estimation.

avoid laser speckle. Due to the spatial–inversion of the roof–prism, the light reflected by the mirror and the roof–prism disperse in opposite directions at the image plane. The resulting spectral blur decreases the difference in visibility between the FG and BG, as expected.

Figure 3-7 shows the result of the experiment with both FG and BG objects. Figure 3-7(a) shows the raw image of the two objects. The upper part is the BG object and the bottom part is the FG object. The slit image is wider than the one with the laser due to the bandwidth of the light source. Since the incident intensities on both objects are controlled to be identical and uniform, the FG and BG object cannot be discriminated based on this image. Subsequently, the fringe visibility at $\Delta x' = 0$ along the y'–axis, which is marked by the red arrow, was measured and the intensity and the visibility are plotted in Fig. 3-7(b). The measured visibilities of the FG and BG object are 0.0899 ± 0.0084 and 0.1219 ± 0.0101, respectively. The visibility difference is 0.032 and the relative difference is about 26%.

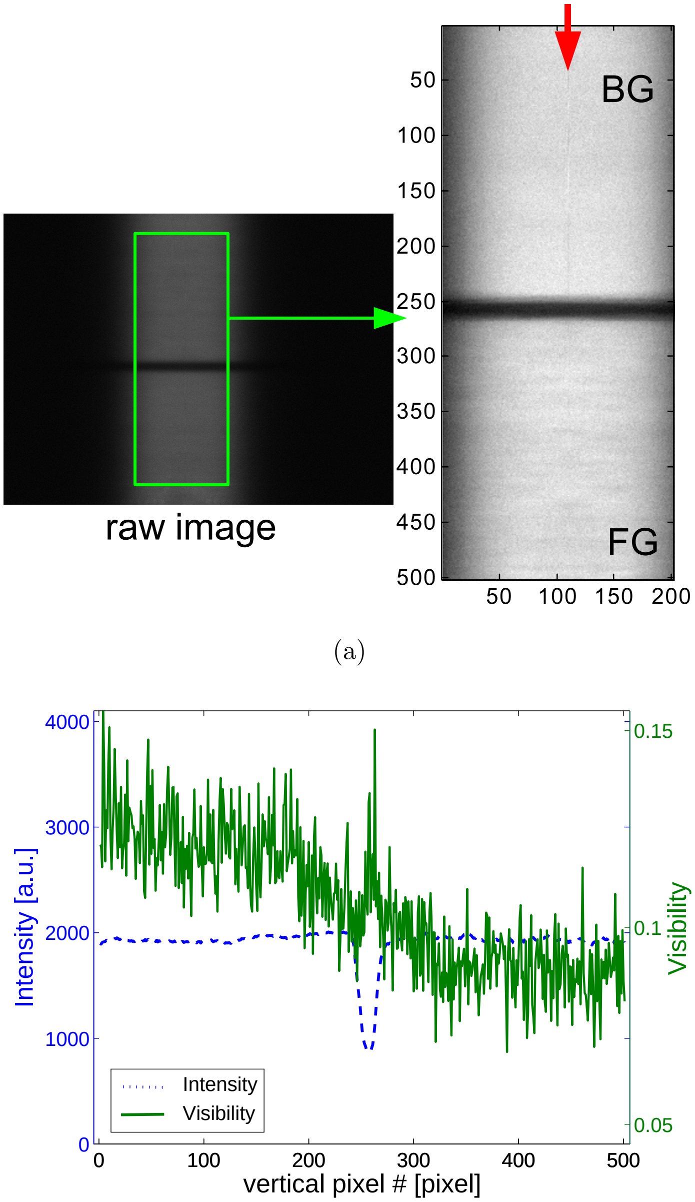

(a)

(b)

Figure 3-7: Experiment with the FG and BG object simultaneously present, where $f_1 = f_2 = 200$ mm, $L = 1$ mm, $\delta_z = 200$ mm, and $\theta_s = 30°$. (a) Raw image on the CCD camera (left) and zoom to the slit–like visible region (right). The red arrow indicates the location where fringe visibility is maximum. (b) Intensity profile (blue dashed line, left–axis) and visibility (green solid line, right–axis) of the two objects.

3.2.3 Discussion

While the proposed system is able to discriminate the FG and BG object as long as they are both quasi–monochromatic and spatially incoherent, it is limited by the fringe visibility change and narrow field of view.

For quasi–monochromatic light, the field of view is easily extended by mechanical scanning or by using multiplexed holograms with multiple interferometers. For broadband light, the wavelength degeneracy also can extend the field of view without any scanning or loss of light as in the rainbow volume holographic holographic profilometry [24], where unused portions of spectrum are utilized. Equivalently, the volume hologram imposes a dispersive virtual slit at the input plane and the wavelength which is Bragg matched varies as the lateral coordinate.

However, as the experiment in Fig. 3-7 shows, the wide spectral bandwidth of the illumination reduces the fringe visibility due to spectral blur, which is described in Fig. 3-8. At the input plane, the different wavelengths from different positions are Bragg matched by the volume hologram. These are traced separately through the mirror and prism path. At the output plane, the dispersed light is imaged; the dispersion directions are opposite with each other. No interference could be observed except near $\Delta x = 0$, where 532 nm light, corresponding to the optical axis, is located. Even near $\Delta x = 0$, the continuous spectrum smears, hence the visibility is severely reduced. This spectral blur needs to be compensated to extend the field of view by exploiting the wavelength degeneracy, as we show in the next section.

3.3 Binary depth detection with broadband illumination

In this section, the system configuration is modified to increase the field of view and compensate the spectral blur simultaneously. The wavelength degeneracy of the volume hologram is fully utilized to separate light spatially and spectrally.

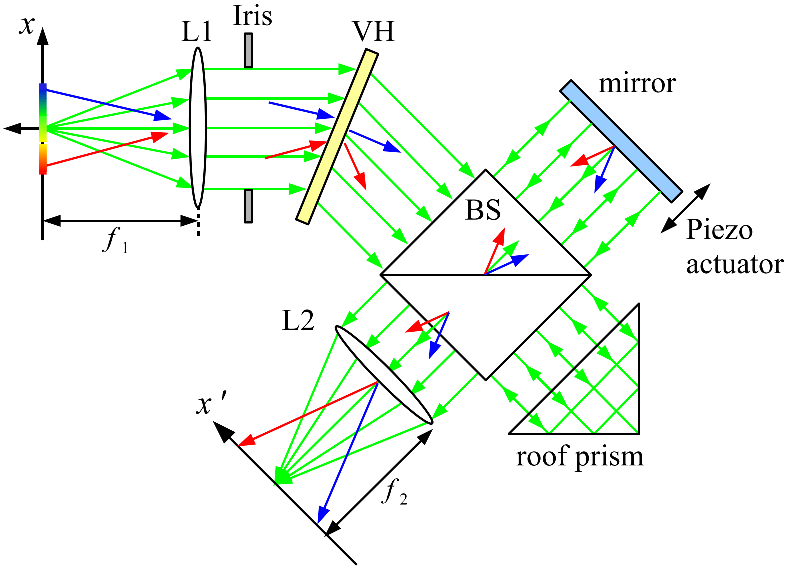

(a) Reflection from the mirror

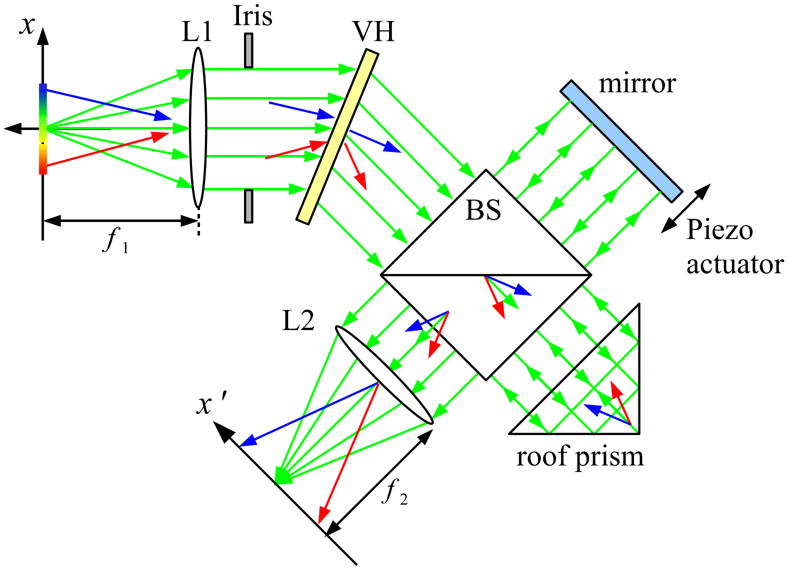

(b) Reflection from the prims

Figure 3-8: Illustration of the spectral blur. The dispersion directions of the split paths are opposite with each other at the image plane.

3.3.1 Spectral degree of coherence

The complex coherence factor, which is the normalized mutual intensity, is used to describe the spatial coherence of quasi–monochromatic light in the simulations and experiments. Now the concept of the spatial coherence should be extended in broadband light, in which the spatial coherence at different frequencies is introduced. Let $V(\mathbf{r}, t)$ denote the analytic signal, representing the fluctuating optical field at the space–time point $(\mathbf{r}, t)$ [68]. Then $V(\mathbf{r}, t)$ denotes a Fourier integral with respect to time:

$$V(\mathbf{r}, t) = \int_0^\infty \tilde{V}(\mathbf{r}, \nu) \mathrm{e}^{-i2\pi\nu t} \mathrm{d}\nu. \tag{3.20}$$

The cross spectral density $W(\mathbf{r}_1, \mathbf{r}_2, \nu)$ of the light disturbances at points $\mathbf{r}_1$ and $\mathbf{r}_2$ at frequency ν is defined by

$$\langle \tilde{V}^*(\mathbf{r}_1, \nu) \tilde{V}(\mathbf{r}_2, \nu') \rangle = W(\mathbf{r}_1, \mathbf{r}_2, \nu) \delta(\nu - \nu'), \tag{3.21}$$

where $\langle\ \rangle$ indicates ensemble average. Equation (3.21) indicates that the cross spectral density is a measure of the correlation between the spectral amplitudes of any particular frequency component of the light vibrations at the points $\mathbf{r}_1$ and $\mathbf{r}_2$. According to the generalized Wiener–Khintchine theorem [68], the mutual coherence and the cross spectral density are Fourier transform pairs:

$$\mathbf{\Gamma}(\mathbf{r}_1, \mathbf{r}_2, \tau) = \int_0^\infty W(\mathbf{r}_1, \mathbf{r}_2, \nu) \mathrm{e}^{-i2\pi\nu\tau} \mathrm{d}\nu, \tag{3.22}$$

$$W(\mathbf{r}_1, \mathbf{r}_2, \nu) = \int_{-\infty}^\infty \mathbf{\Gamma}(\mathbf{r}_1, \mathbf{r}_2, \tau) \mathrm{e}^{i2\pi\nu\tau} \mathrm{d}\tau. \tag{3.23}$$

In the special case when the two points $\mathbf{r}_1$ and $\mathbf{r}_2$ coincide, the cross spectral density becomes a function of the location of only one point and of the frequency, which represents the *spectral density* (the power spectrum) of the light:

$$S(\mathbf{r}, \nu) = W(\mathbf{r}, \mathbf{r}, \nu). \tag{3.24}$$

By using eqs. (3.22) and (3.23), we have

$$\mathbf{\Gamma}(\mathbf{r},\mathbf{r},\tau) = \int_0^\infty S(\mathbf{r},\nu)\mathrm{e}^{-i2\pi\nu\tau}\mathrm{d}\nu, \tag{3.25}$$

$$S(\mathbf{r},\nu) = \int_{-\infty}^\infty \mathbf{\Gamma}(\mathbf{r},\mathbf{r},\tau)\mathrm{e}^{i2\pi\nu\tau}\mathrm{d}\tau. \tag{3.26}$$

It is useful to normalize the cross spectral density by setting

$$\mu(\mathbf{r}_1,\mathbf{r}_2,\nu) = \frac{W(\mathbf{r}_1,\mathbf{r}_2,\nu)}{\left[W(\mathbf{r}_1,\mathbf{r}_1,\nu)\right]^{1/2}\left[W(\mathbf{r}_2,\mathbf{r}_2,\nu)\right]^{1/2}}. \tag{3.27}$$

Similar to the case of $\gamma(\mathbf{r}_1,\mathbf{r}_2,\tau)$, we have

$$0 \le |\mu(\mathbf{r}_1,\mathbf{r}_2,\nu)| \le 1 \tag{3.28}$$

for all values of the arguments $\mathbf{r}_1$, $\mathbf{r}_2$, and ν. We refer to $\mu(\mathbf{r}_1,\mathbf{r}_2,\nu)$ as the *spectral degree of coherence at frequency* ν of the light at the point $\mathbf{r}_1$ and $\mathbf{r}_2$ [68]. It is sometimes also referred to as the complex degree of spatial (or spectral) coherence at frequency ν [69–72].

3.3.2 Modified system configuration

As described in Sec. 3.2.3, multi–color operation is limited by field of view and spectral blur. In this section, the wavelength degeneracy of the volume hologram is exploited to solve these problems simultaneously.

First the field of view is examined; the lateral field of view is limited by the Bragg condition, which applies constraints to wavelengths and lateral positions (corresponding angle). For a given x coordinate, the Bragg matched wavelength is given by

$$\lambda_{\mathrm{p}} = \lambda_{\mathrm{f}}\frac{\sin\left(\theta_{\mathrm{s}}/2 - x/f_1\right)}{\sin(\theta_{\mathrm{s}}/2)}. \tag{3.29}$$

The lateral coordinates are encoded in wavelengths; decoding wavelength information from the cross spectral density allows us to recover the lateral information. This is a unique property of volume holograms. Note that the field of view is limited by the

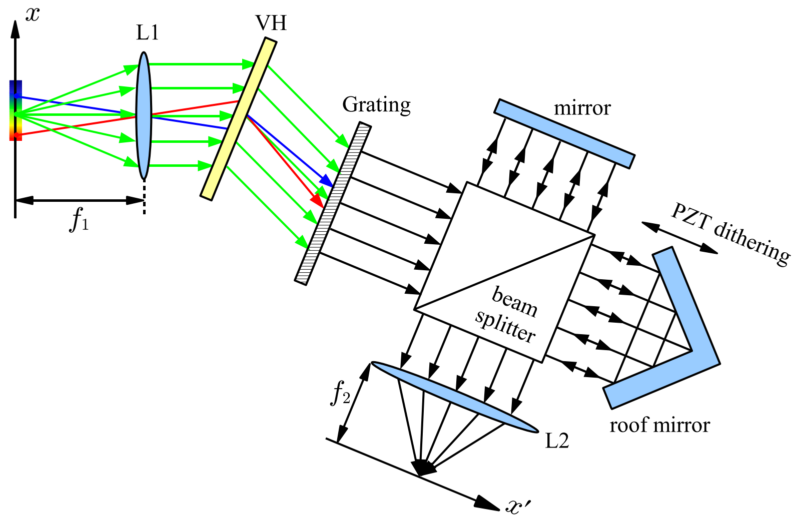

Figure 3-9: New system configuration for operation under broadband illumination. A diffraction grating just behind the volume hologram compensates the dispersion so that different wavelengths of light propagate in parallel. Scanning the OPD and taking the Fourier transform decodes the mixed spectral information which corresponds to the lateral information.

spectral bandwidth of the light. For example, if an extended object is illuminated by a narrow bandwidth, then the field of view is still limited.

To avoid spectral blur in the interferometer, all light should be normally incident on the interferometer regardless of wavelength. One solution is compensating the dispersion caused by the volume hologram; using a diffraction grating of the exactly opposite dispersion can cancel the dispersion induced by the volume hologram. Even though a portion of light is lost, a diffraction grating is inserted behind the volume hologram as shown in Fig. 3-9. The dispersion of the grating is easy to control by adjusting the grating pitch.

In this new system configuration, the dispersed Bragg diffraction from the volume hologram is re–diffracted by the grating, collimating the 1$^{\text{st}}$ order diffraction over the entire spectral bandwidth. The wavefront folding interferometer works identically as in the previous setup (Fig. 3-1), and the light is focused on the image plane. Equivalently, the function of the grating is to control the width of the rainbow shown in Fig. 3-8(a) and (b), as the wavefront folding interferometer still produces the desired flipping for all wavelengths. If the grating is perfectly matched with the

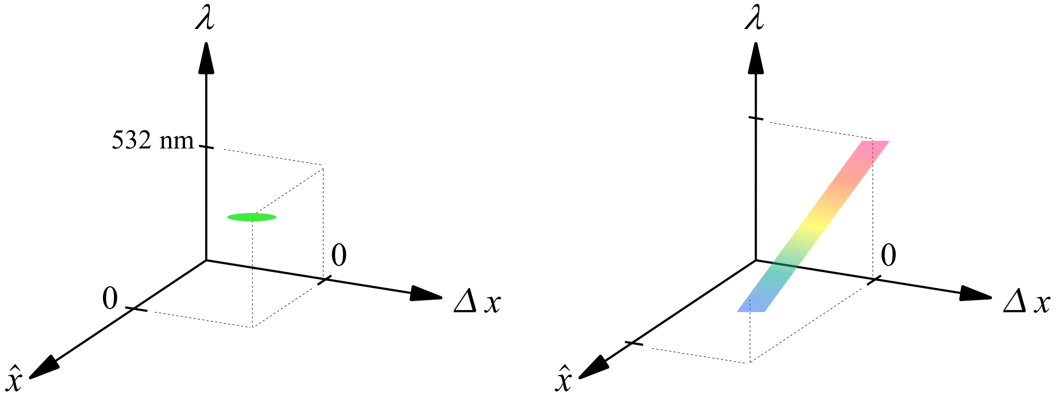

(a) quasi–monochromatic setup (b) broadband setup

Figure 3-10: Comparison of sampled spectral density. $W(\Delta x, \hat{x}, \lambda)$ is plotted instead of $W(x_1, x_2, \nu)$ which is measured in each system. Note that $\Delta x = x_1 - x_2$ and $\hat{x} = (x_1 + x_2)/2$.

volume hologram, the rainbows are shrunk down to the focus and all wavelengths are mixed. Note that, even though the recombined light at the focal line appears to be white, its color components originate from different locations at the object plane. The mutual coherence measured in the interferometer with optical path delay modulation gives the cross spectral density after a Fourier transform operation. The cross–spectral measurement is commonly used in Fourier spectroscopy [73].

In terms of the cross spectral density, the two systems are compared in Fig. 3-10: the one without the grating (Fig. 3-1) and the one with the grating (Fig. 3-9). As shown in Fig. 3-10(a), the quasi–monochromatic setup (the one without the grating), measures the spatial coherence only near $\hat{x} = 0$, $\Delta x = 0$, and $\lambda = 532$ nm. The broadband setup (with the grating) measures along a strip, which is confined near $\Delta x = 0$ but extended along λ and $\hat{x}$ as shown in Fig. 3-10(b). Again, the depth information of a scene is encoded in the Δx dimension of the cross spectral density. The lateral spatial information is carried in λ dimension, coupled with $\hat{x}$.

Next the specification of a diffraction grating that perfectly compensated the dispersion of the volume hologram is calculated. A diffraction grating is inserted behind the volume hologram as shown in Fig. 3-11. The dispersion of the volume

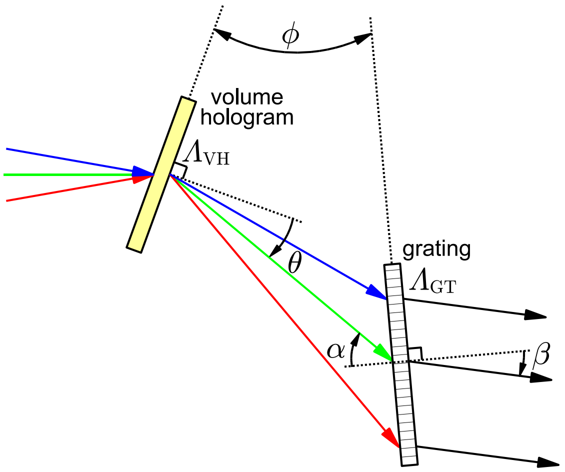

Figure 3-11: Geometry for perfect dispersion compensation between a volume hologram and diffraction grating, where Λ_{VH} and Λ_{GT} are the period of the volume hologram and the grating, respectively. θ is diffraction angle of the volume hologram, and α and β are the incident and diffraction angle to the grating. ϕ denotes the orientation difference of the volume hologram and the grating. Note that β should be identical over wavelength.

hologram and grating are given by [74]

$$\text{Volume hologram} \rightarrow \quad \lambda = 2\,(\Lambda_{VH})\sin(\alpha - \phi), \qquad \text{and} \tag{3.30}$$

$$\text{Grating} \rightarrow \quad \lambda = (\Lambda_{GT})\,(\sin\alpha + \sin\beta)\,. \tag{3.31}$$

Note that the diffraction angle θ of the volume hologram is replaced by $\alpha - \phi$ due to the geometry. To compensate for dispersion, the diffraction angle β should be constant regardless of λ and α. One obvious solution is $\phi = 0$, $\beta = 0$, and $2\Lambda_{VH} = \Lambda_{GT}$, which suggests that the grating and volume hologram are oriented parallel to each other and the direction of the diffracted light is perpendicular to the grating. If the two conditions are satisfied, for the volume hologram used in our experiments, the desired grating period is 1356 nm (equivalent to 737.46 grooves/mm).

As proposed, the wavelength degeneracy allows us to extend the field of view as well as to reduce the spectral blur. However, there are several limitations: 1) The spectral bandwidth must be broad enough to fill the entire field of view. 2) The spectral bandwidth of the FG and BG objects are assumed to be identical. If the two

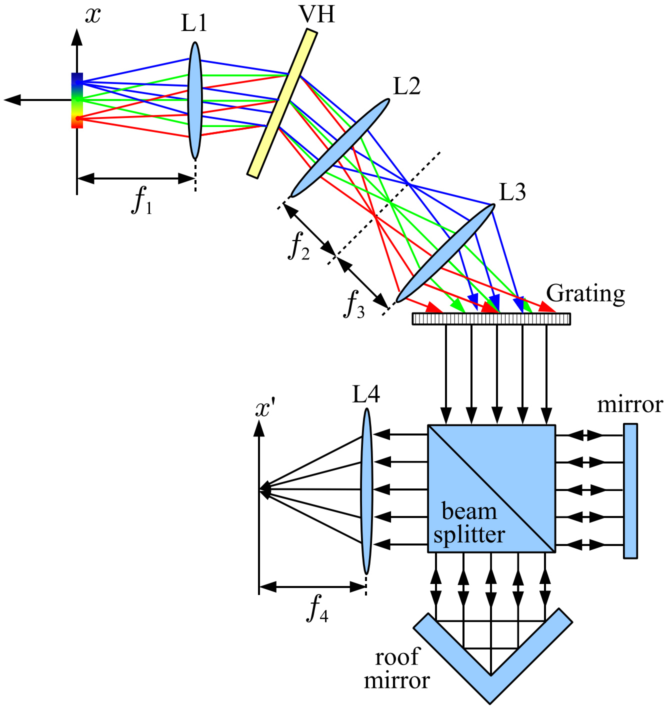

Figure 3-12: The volume holographic interferometer with a grating and telescope for dispersion matching; $f_1 = 200$ mm, $f_2 = 30$ mm, $f_3 = 38$ mm, $f_4 = 150$ mm, and $\Lambda_{GT} = 1/600$ mm.

objects at FG and BG have different spectral bandwidths, then the spectral bandwidths need be known. In the experiments described in Sec. 3.3.3, both the FG and BG objects are white and illuminated by two identical broadband sources; therefore, the field of view is maximized and the two objects are discriminated longitudinally as well as laterally.

3.3.3 Experiments

Although the diffraction grating whose dispersion is identically matched with the available volume hologram can be fabricated with conventional manufacturing techniques, an off the shelf diffraction grating (GT50–06V, pitch: 1/600 mm, Thorlab, NJ) was used for the proof of concept experiment. The actual experimental system is shown in Fig. 3-12. To match the dispersion, two additional lenses (L2, L3 in Fig. 3-12) were used. The third lens (L3) is a zoom lens (H6Z0812, Computar, Japan), whose focal length is adjustable to ensure the best dispersion matching. The disper-

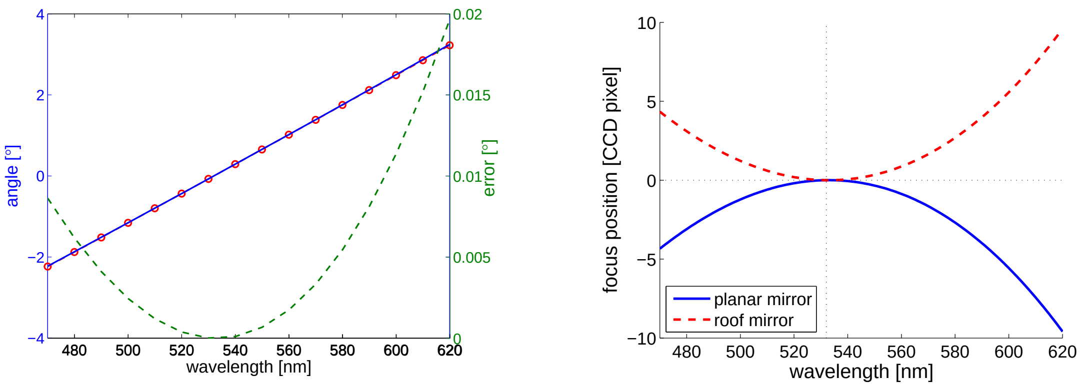

(a) dispersion errors

(b) lateral focus shift

Figure 3-13: Dispersion errors and lateral focus shift on the image plane. In (a), the blue line (left–axis) is the incident angle to the grating and the red circles (left–axis) are the dispersion of the grating over wavelength. The dispersion error (the difference between the incident angle and actual dispersion of the grating) is plotted with a dashed green line (right–axis). In (b), the lateral focus shift due to the dispersion error is plotted.

sion error is shown in Fig. 3-13. In Fig. 3-13(a), three lines are plotted: the incident angle to the grating from the third lens (L3), the desired incident angle whose diffraction angle is zero, and the difference between them. Note that the small error (green dashed line in Fig 3-13(a) indicates that the incident angle onto the interferometer varies slightly over wavelength, which produces a small lateral focal shift as shown in Fig. 3-13(b). Note that dispersion matching is improved by inserting the grating and two lenses. To avoid the material dispersion of the roof prism, we replaced it with a roof mirror (RM–10–05, PLX, NY). We also substituted the open–loop PZT stage with a feed–back controlled PZT (NF5DP20S and BPC201, Thorlab, NJ) to modulate the optical path difference precisely. During the measurement, the total scanned optical path length was 40 μm in 50 nm increments, corresponding to a wavelength resolution of 9.4 nm at 532 nm.

In the first experiment, depth discrimination was demonstrated as follows: two flat sheets of diffuse white paper were placed at FG and BG planes simultaneously. With two identical white light sources (250W Tungsten Quartz Lamp, CUDA, FL), the intensities on both objects were controlled to be as equal as possible. Figure 3-14 shows the result when the FG object is located in the upper region of the field of

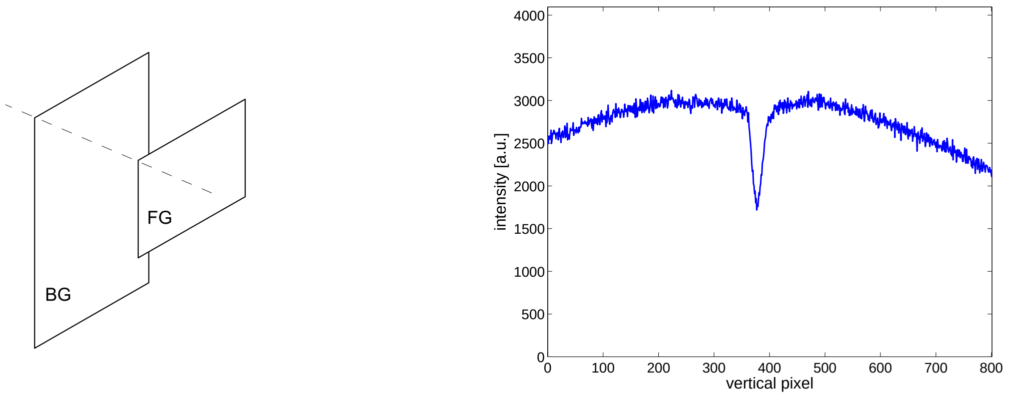

(a) Actual scene

(b) intensity profile

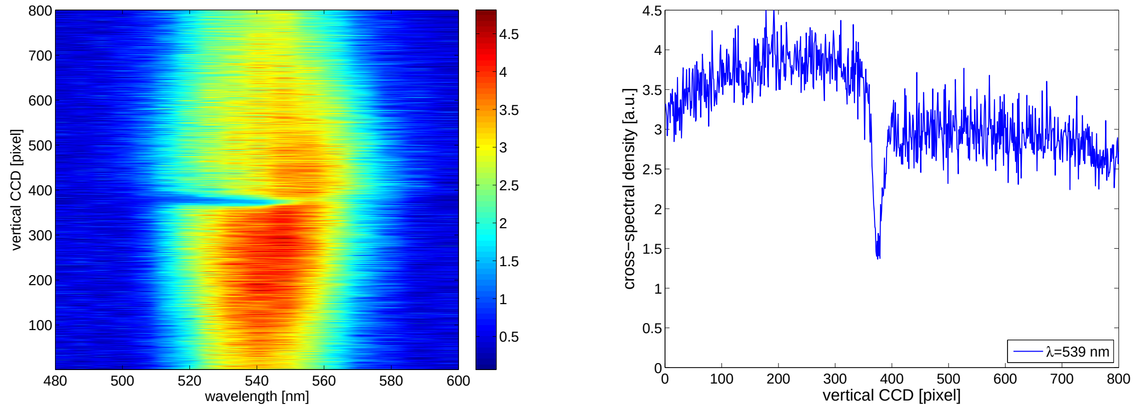

(c) cross spectral density

(d) cross–section of the cross spectral density

Figure 3-14: The experimental result when the FG object is located in the upper region and the BG object is in the lower region of the field of view.

view. As expected, the lower region, which corresponds to the BG object, yields higher cross spectral density values while the intensity on both objects are similar, shown in Fig. 3-14(b). The intensity profile is taken from the first frame; the optical path difference is far longer than the coherence length of the source. In the next experiment, the vertical position of the BG object was switched, i.e., the BG object was located in the lower region of the field of view, and the cross spectral density was measured again. As Fig. 3-15 shows, the cross spectral density is also switched vertically.

Next lateral discrimination capability was demonstrated. The situation was similar to the previous experiments except the FG object partially covers the lower region of the field of view as well as entire upper region of the field of view. The cross spectral

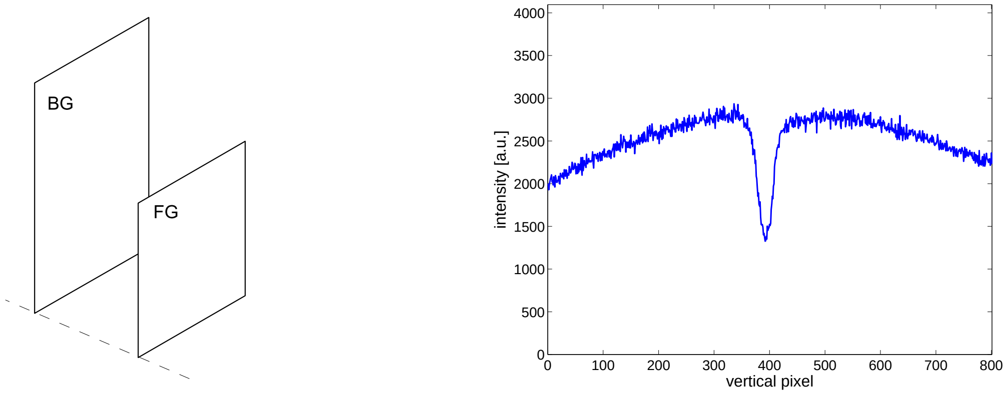

(a) Actual scene (b) intensity profile

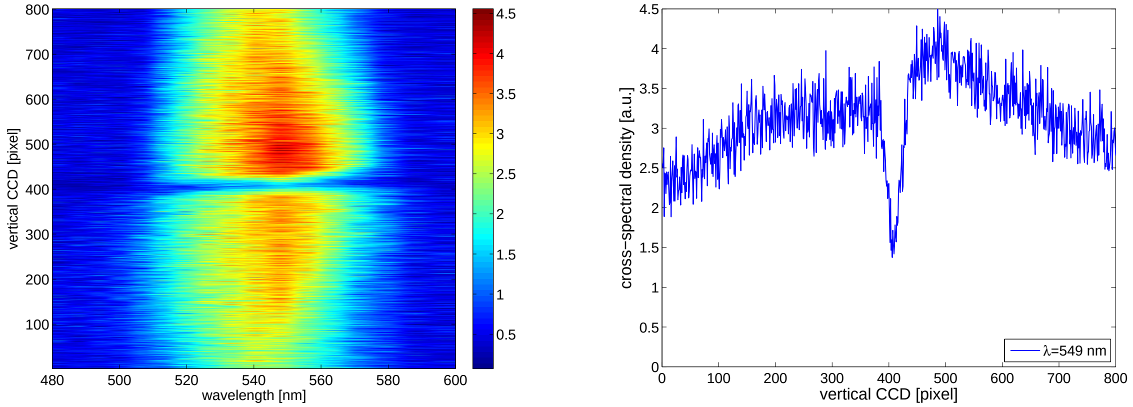

(c) cross spectral density (d) cross–section of the cross spectral density

Figure 3-15: The experimental result when the FG object is located in the lower region and the BG object is in the upper region of the field of view.

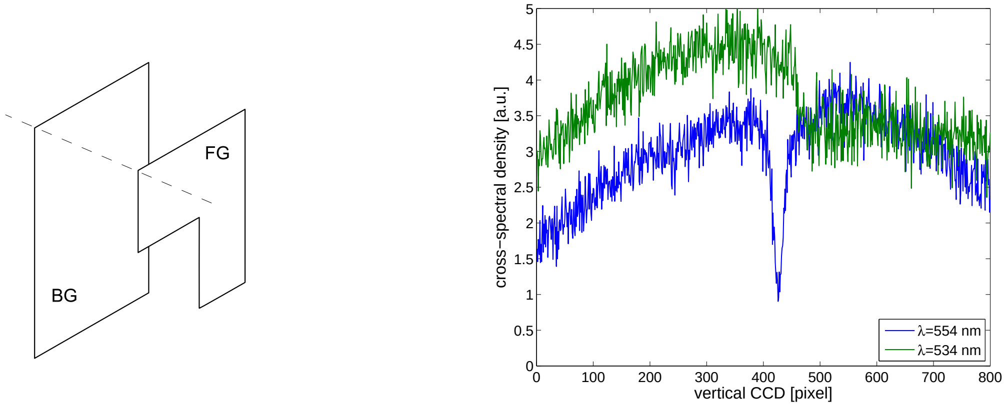

(a) Actual scene

(b) cross–section of (d)

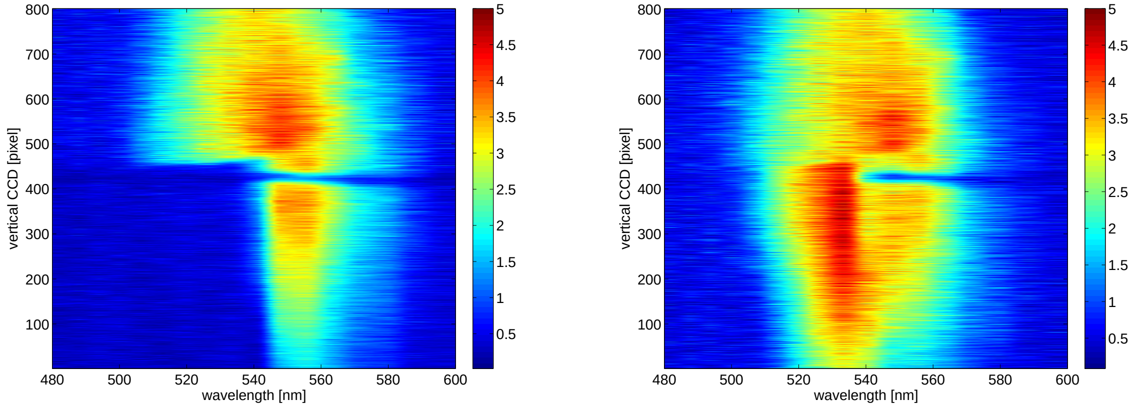

(c) BG lamp off

(d) BG lamp on

Figure 3-16: The measured cross spectral density when the two objects are overlapped laterally in the lower region of the field of view.

density measured in this situation is shown in Fig. 3-16. The lamp that illuminates the BG object was turned off, and the measured cross spectral density is shown in Fig. 3-16(c); an edge is shown clearly. The lamp was turned on and the cross spectral density was measured again, shown in Fig. 3-16(d). The same experiment was repeated with the flipped FG object; the result is shown in Fig. 3-18. As demonstrated, the cross spectral density encodes the defocus as well as lateral information.

Finally, a simple experiment was demonstrated to show the difference of regular intensity images and cross spectral density images measured by the proposed method. As shown in Fig. 3-18(a), one sheet of a white, diffuse paper was placed at the BG plane and another sheet of identical paper at the FG plane. The FG object had a small rectangular window, which the BG object can be seen through the window. Two

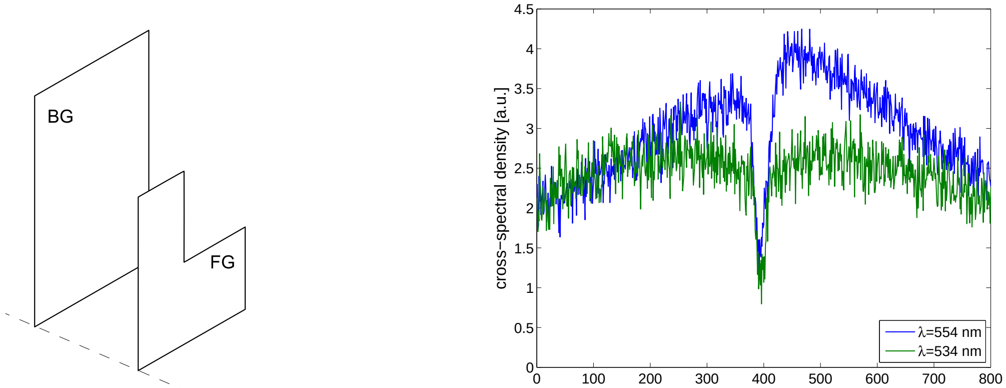

(a) Actual scene

(b) cross–section of (d)

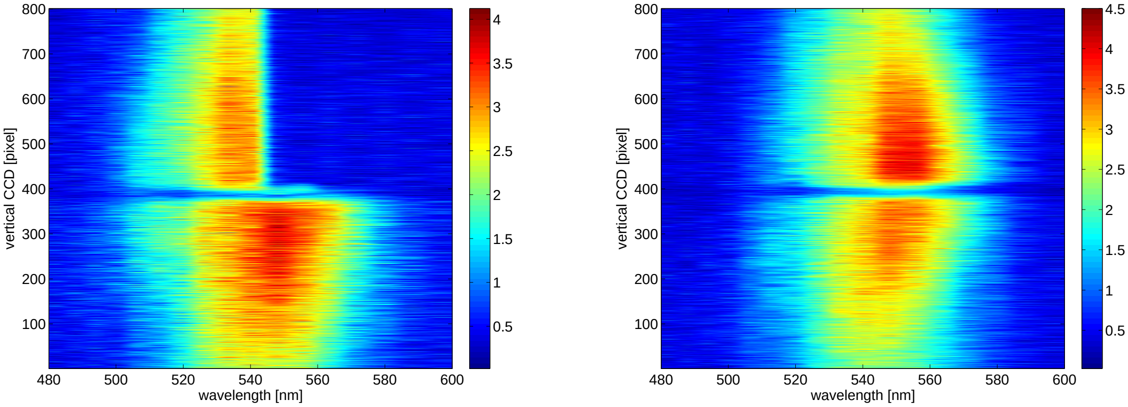

(c) BG lamp off

(d) BG lamp on

Figure 3-17: The measured cross spectral density when the two objects are overlapped laterally in the upper region of the field of view

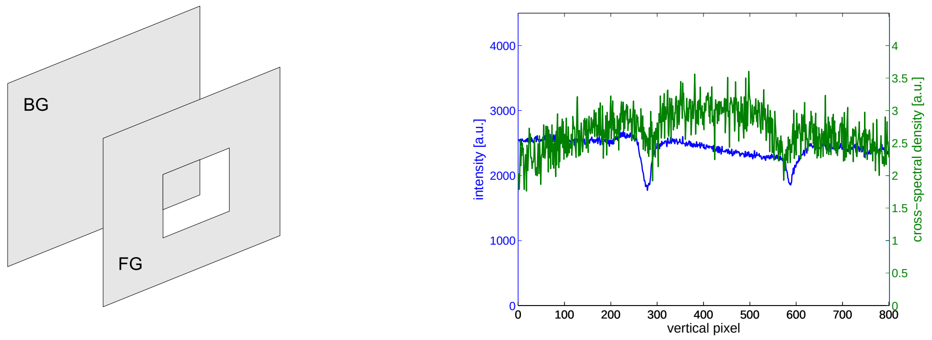

(a) Actual scene

(b) Vertical profile of intensity (blue, left–axis) in (f) and cross spectral density (green, right–axis) in (d)

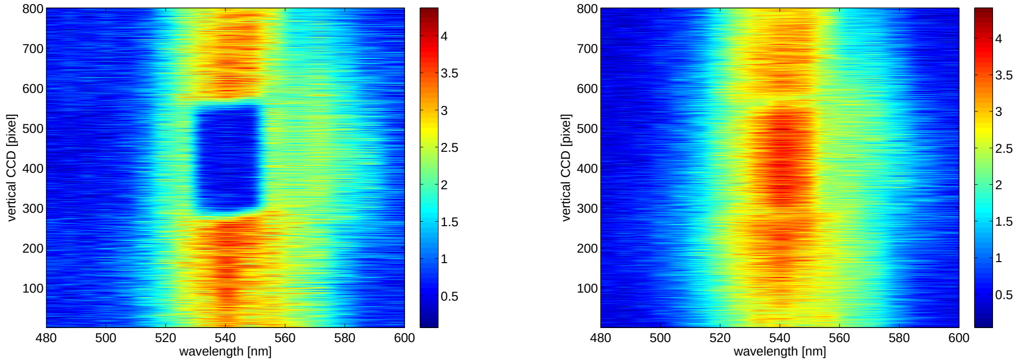

(c) Cross–spectral density image with the BG lamp off

(d) Cross–spectral density image with the BG lamp on

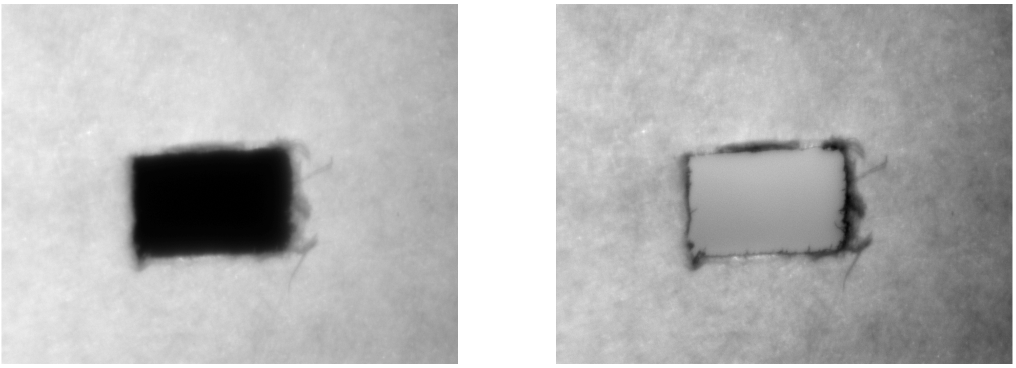

(e) regular intensity image with the BG lamp off

(f) Regular intensity image with the BG lamp on

Figure 3-18: Comparisons of regular intensity images and cross spectral density images. Note they have different magnifications.

white light sources were used to illuminate the two objects. Figure 3-18(c) and (e) are images when the BG lamp was off, and Fig. 3-18(d) and (f) are images when the BG lamp was on. The profiles of the regular intensity image and the cross spectral density image are plotted in Fig. 3-18(b). In the regular image, shown in Fig. 3-18(f), there is no sense of depth without prior knowledge of the spatial frequency of the paper texture. In the cross spectral density image, the BG region at the center yields slightly higher values in the cross spectral density image, shown in Fig. 3-18(d) although the intensity is slightly lower in the central region as shown in Fig. 3-18(b).

3.4 Conclusion and Discussion

For VHI systems, the partially coherent response has been formulated by using statistical optics. For a specific case, the VHI system with a slab–shape volume hologram is examined.

Then, a new passive depth detection method based on spatial coherence measurements was proposed. The system cascades a wavefront folding interferometer with a VHI system; the volume hologram separates light spatially and spectrally and the cross spectral density is measured by interferometric measurements. Assuming spatially incoherent objects, a spatial coherence change of the FG and BG object was detected and binary depth detection for flat featureless objects was demonstrated.

To extend the field of view and to improve the depth resolving capability by reducing spectral blur, the wavelength degeneracy of volume holograms was exploited. A diffraction grating and two lenses were inserted to compensate the dispersion caused by the volume hologram and the cross spectral density measurements were implemented. The new system operates under broadband illumination, and not only longitudinal but also lateral discrimination abilities were demonstrated.

The role of the volume hologram in this approach is understood as follows: 1) The volume hologram separates the light spectrally and spatially not only to improve the fringe visibility but also to encode the lateral spatial information. 2) The lateral point spread function becomes narrower, which yields better contrast.

One principal difference between the presented method and prior coherence imaging approaches is that by binarizing the problem the number of required measurements has been reduced. That is, we explicitly shy away from measuring the entire coherence function; rather we measure as few of its values as possible to obtain an answer to the binary detection problem.

The second major difference is the use of a volume holographic filter at the pupil plane of a telescope which precedes the wavefront folding interferometer. The entire concept appears to go against one of the motivations which has often been cited for coherence imaging, namely, lensless image formation; in return we obtain other benefits. The volume holographic pupil effectively acts as a dispersive slit [7] and thus reduces the background in the interference measurement. Since the proposed systems has a imaging configuration in the y–axis, the quality of images is better than the ones in coherence imaging.

By introducing these new concepts, depth detection of relatively uniform objects can be dealt with, i.e., case where lateral spatial frequency content is lacking. Such objects have been traditionally considered "difficult" in the fields of both coherence imaging, because of the background noise, and in computer vision, because of the lack of features to associate with depth. The foreground *vs.* background discrimination experiment of Sec. 3.3.3 is a good example of such an object.

An ultimate goal is definitely to discriminate multiple depths. Since our method relies on the difference in the degree of coherence, and the fact that the change in spatial coherence with depth is limited, detecting multiple depths is challenging. If the degree of coherence of objects are identical so that the spatial coherence changes monotonically or if they are *priori*–known, then multiple depth detection may be possible provided that we achieve accurate and sensitive enough measurements.

The same method is applicable if multiple objects and/or spatially non–uniform objects are present in the scene. As long as the degree of coherence of the light from non FG objects is higher than the degree of coherence of FG objects, it should be possible to order the objects by their distance from the entrance pupil. It would also be interesting to investigate the transition of the degree of coherence between FG and

BG, which is shown as Fig. 3-7. These topics are left as future research.

Chapter 4

Space–spatial frequency analysis of volume holographic pupils and axial imaging

While spatial frequency analysis is extremely useful, all local spatial information is lost due to the nature of the Fourier transform. Using local spatial frequency instead of the global spatial frequency could be useful because it contains both spatial and frequency information [5]. In this chapter, the Wigner distribution function (WDF) is introduced, which is a space–spatial frequency representation of light, and it is applied to volume holograms and VHI systems to characterize shift variant behavior. Axial imaging, which measures depth information from images, is a particularly interesting example of multi–dimensional imaging. Hence, the Wigner analysis is applied to axial imaging to explore the various axial imaging methods and characterize invariant/variant imaging kernels. Finally two main conditions for axial imaging capability are established.

4.1 Introduction

Although the Wigner distribution function (WDF) was originally introduced in quantum mechanics [75], it has been useful in optics because it describes simultaneous both the space domain and spatial frequency information of optical signals [76]. The WDF of an optical field $g(\mathbf{x})$ is defined as

$$\mathcal{W}(\mathbf{x},\mathbf{u}) = \int g(\mathbf{x}+\boldsymbol{\xi}/2)g^*(\mathbf{x}-\boldsymbol{\xi}/2)\exp\{-i2\pi\mathbf{u}\cdot\boldsymbol{\xi}\}\,\mathrm{d}\boldsymbol{\xi}, \tag{4.1}$$

where $g(\mathbf{x})$ is a scalar function of a position vector $\mathbf{x}$, $\boldsymbol{\xi}$ is a dummy variable for the integration (indeed, Fourier transform), and $\mathbf{u}$ is a local spatial frequency vector. Here, some of important properties of the WDF are summarized [77].

1. Frequency domain definition: if $G(\mathbf{u})$ is the Fourier transform of $g(\mathbf{x})$, then the WDF of $g(\mathbf{x})$ is equivalently defined as

$$\mathcal{W}(\mathbf{x},\mathbf{u}) = \int G\left(\mathbf{u}+\frac{\mathbf{u}'}{2}\right)G^*\left(\mathbf{u}-\frac{\mathbf{u}'}{2}\right)\exp\{i2\pi\mathbf{x}\cdot\mathbf{u}'\}\,\mathrm{d}\mathbf{u}'. \tag{4.2}$$

2. *Inversion:* The original function can be recovered from its WDF within a phase factor as

$$g(\mathbf{x}) = \frac{1}{g^*(0)}\int \mathcal{W}(\mathbf{x}/2,\mathbf{u})\exp\{i2\pi\mathbf{x}\cdot\mathbf{u}\}\,\mathrm{d}\mathbf{u}. \tag{4.3}$$

3. *Realness:* The WDF is a real function, but not always positive.

4. *Interference:* The WDF of the sum of two signals $f(\mathbf{x})+g(\mathbf{x})$ is expressed as

$$\mathcal{W}_{f+g}(\mathbf{x},\mathbf{u}) = \mathcal{W}_f(\mathbf{x},\mathbf{u}) + \mathcal{W}_g(\mathbf{x},\mathbf{u}) + 2Re\left[\mathcal{W}_{f,g}(\mathbf{x},\mathbf{u})\right], \tag{4.4}$$

where the last term is a *cross* term or interference term because of the bilinear nature of the WDF.

5. *Intensity:* The integral along the spatial frequency, equivalently the projection of the WDF along u, is the intensity of the signal as

$$I(\mathbf{x}) = \int \mathcal{W}(\mathbf{x},\mathbf{u})\mathrm{d}\mathbf{u}. \tag{4.5}$$

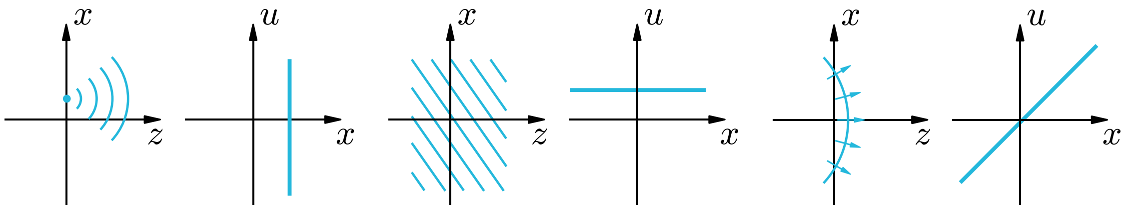

(a) point source (b) plane wave (c) spherical wave

Figure 4-1: Various optical waves in the space domain and their corresponding Wigner distribution functions

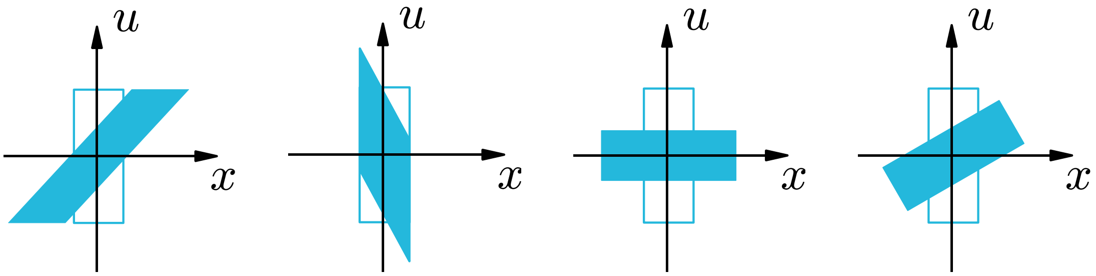

(a) Fresnel propagation (b) Chirp modulation (lens) (c) Fourier transform (d) Fractional Fourier transform

Figure 4-2: Representation of various optical transforms in optics in Wigner space, where the blank rectangles indicate input fields and solid rectangles represent transformed fields

The local spatial frequency corresponds to the angle of a ray in geometrical optics [5]; hence, the WDF may be thought of as a connection between ray and wave optics. More importantly, the WDF is extremely useful to analyze how light behaves as it propagates, because many optical fields and transforms are described as simple geometrical relations. Figures 4-1 and 4-2 show the WDFs of various optical fields and transforms. Note that the Fresnel propagation and chirp modulation correspond to x and u shear, respectively. Using these geometrical relations and knowledge of local spatial frequency, the WDF analysis allows us a better understanding and a different perspective of light phenomena.

It is worth mentioning that the ambiguity function, the 2D Fourier transform of the WDF, also exhibits similar properties and is useful for many applications such as optimization of wavefront coding systems for extended depth of field [1, 78]. Specifically, the WDF and the ambiguity function are related through the Fourier slice theorem. For example, in a linear shift invariant imaging system, the intensity PSF and the OTF are the Fourier transform pair, and they are decided by a pupil function. In Wigner space, the WDF of the pupil characterizes both. The intensity PSF is the projection of the WDF of the Fourier transformed pupil along u; this is equivalent to the projection of 90° rotated WDF of the pupil. Since the Fourier transform of the intensity PSF (projection of the WDF) is the OTF, the slice of the ambiguity function of the pupil is indeed the OTF. As mentioned, the free–space propagation corresponds to x–shear, the WDF and the ambiguity function describes with the intensity PSF and the OFT for different defocus at the same time.

The WDF also can deal with partially coherent light [79]. The Wigner analysis has been used in 3D display [77], digital holography [80, 81], the generalized sampling problem [81], and superresolution [82].

The WDF of a thin transparency such as a lens, phase mask, aperture, or grating can be found in [83–85]. However, the volume hologram has a finite longitudinal extent; because of that, it is not straightforward to express volume holograms in Wigner space. In the next section, Wigner representations of the volume hologram and VHI systems are derived.

4.2 Wigner distribution function of volume holograms

In a linear optical system, an output field $E(x_2, y_2)$ is a superposition of impulse responses weighted by an input field $E(x_1, y_1)$, written as

$$E(x_2, y_2) = \int E(x_1, y_1) h(x_2, y_2; x_1, y_1) \mathrm{d}x_1 \mathrm{d}y_1, \tag{4.6}$$

where $h(x_2, y_2; x_1, y_1)$ is the system response at the output plane (x_2, y_2) generated by an impulse input at (x_1, y_1). If the impulse response is laterally shift invariant, then the output field is a convolution of the impulse response and the input field. Using

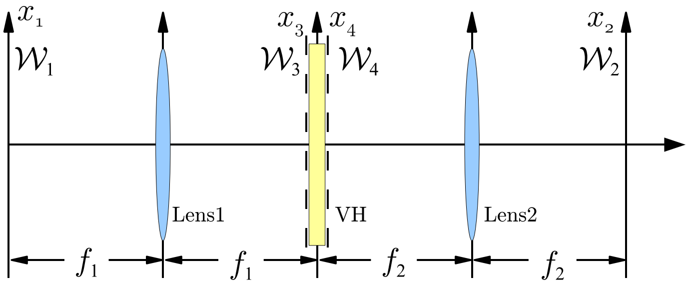

Figure 4-3: Geometry of the 4–f volume holographic imaging system. The focal length of the two lenses are f_1 and f_2, respectively.

eqs. (4.1) and (4.6), the input–output relation in the WDF space is written as [86]

$$\mathcal{W}_2(x_2,u_2,y_2,v_2)=\iiiint K_h(x_2,u_2,y_2,v_2;x_1,u_1,y_1,v_1)\mathcal{W}_1(x_1,u_1,y_1,v_1)\mathrm{d}x_1\mathrm{d}u_1\mathrm{d}y_1\mathrm{d}v_1 \tag{4.7}$$

where

$$\begin{aligned}K_h(x_2,u_2,y_2,v_2;x_1,u_1,y_1,v_1)&=\iiiint \mathrm{e}^{-i2\pi\left(u_2x_2'+v_2y_2'-u_1x_1'-v_1y_1'\right)}\mathrm{d}x_2'\mathrm{d}x_1'\mathrm{d}y_2'\mathrm{d}y_1'\\ \times\, h\left(x_2+\tfrac{x_2'}{2},y_2+\tfrac{y_2'}{2};x_1+\tfrac{x_1'}{2},y_1+\tfrac{y_1'}{2}\right)&h^*\left(x_2-\tfrac{x_2'}{2},y_2-\tfrac{y_2'}{2};x_1-\tfrac{x_1'}{2},y_1-\tfrac{y_1'}{2}\right),\end{aligned} \tag{4.8}$$

and u_i and v_i are the local spatial frequencies corresponding to the spatial coordinates x_i and y_i for $i=1$ and 2, and K_h is the double Wigner distribution function of the impulse response. Once the impulse response is known, the WDF representation can be computed by eq. (4.8); the space–spatial frequency characteristics are fully described by the Wigner presentation. Since the impulse response of the 4–f system is previously derived in Sec. 2.3, the Wigner representation is derived first. Then the Fourier transform relation is exploited to obtain the Wigner representation of volume holograms; in the 4–f volume holographic imaging system, shown in Fig. 4-3, the input and output planes are the front and back focal plane of the first and second lens, respectively.

A volume hologram is located at the Fourier plane. For a probe beam whose wavelength λ is the same as the wavelength of the reference and signal waves, the impulse response of the system is given by

$$h(x_2, y_2; x_1, y_1) = \mathcal{E}\left[\frac{1}{\lambda}\left(\frac{x_1}{f_1}+\frac{x_2}{f_2}\right), \frac{1}{\lambda}\left(\frac{y_1}{f_1}+\frac{y_2}{f_2}\right), \frac{1}{\lambda}\left(\frac{x_1^2+y_2^2}{2f_1^2}-\frac{x_2^2+y_2^2}{2f_2^2}\right)\right], \quad (4.9)$$

where $\mathcal{E}$ is the 3D Fourier transform of the 3D pupil. By substituting eq. (4.9) into eqs. (4.7) and (4.8), the Wigner representation of the 4–f VHI system is obtained as

$$\mathcal{W}_2(x_2, u_2, y_2, v_2) = \iiiint K_{\mathrm{VHI}}(x_2, u_2, y_2, v_2; x_1, u_1, y_1, v_1) \times \mathcal{W}_1(x_1, u_1; y_1, v_1)\mathrm{d}x_1\mathrm{d}u_1\mathrm{d}y_1\mathrm{d}v_1, \quad (4.10)$$

where

$$\begin{aligned}K_{\mathrm{VHI}}(x_2, u_2; x_1, u_1) = &\iiiint \mathrm{d}x_1'\mathrm{d}x_2'\mathrm{d}y_1'\mathrm{d}y_2'\mathrm{e}^{-i2\pi\left(u_2x_2'+v_2y_2'-u_1x_1'-v_1y_1'\right)}\\ &\times \mathcal{E}\left[\frac{1}{\lambda}\left(\frac{x_1+\frac{x_1'}{2}}{f_1}+\frac{x_2+\frac{x_2'}{2}}{f_2}\right), \frac{1}{\lambda}\left(\frac{y_1+\frac{y_1'}{2}}{f_1}+\frac{y_2+\frac{y_2'}{2}}{f_2}\right),\right.\\ &\left.\frac{1}{\lambda}\left(\frac{(x_1+\frac{x_1'}{2})^2+(y_1+\frac{y_1'}{2})^2}{2f_1^2}-\frac{(x_2+\frac{x_2'}{2})^2+(y_2+\frac{y_2'}{2})^2}{2f_2^2}\right)\right]\\ &\times \mathcal{E}^*\left[\frac{1}{\lambda}\left(\frac{x_1-\frac{x_1'}{2}}{f_1}+\frac{x_2-\frac{x_2'}{2}}{f_2}\right), \frac{1}{\lambda}\left(\frac{y_1-\frac{y_1'}{2}}{f_1}+\frac{y_2-\frac{y_2'}{2}}{f_2}\right),\right.\\ &\left.\frac{1}{\lambda}\left(\frac{(x_1-\frac{x_1'}{2})^2+(y_1-\frac{y_1'}{2})^2}{2f_1^2}-\frac{(x_2-\frac{x_2'}{2})^2+(y_2-\frac{y_2'}{2})^2}{2f_2^2}\right)\right]. \quad (4.11)\end{aligned}$$

Next, we compute the Wigner representation of the volume hologram. In the 4–f VHI system, the incident field onto and the diffracted field from the volume hologram are Fourier transform conjugates to the input and output field, respectively, as shown in Fig. 4-3. Although we treat the volume hologram as a thin transparency in this case, the longitudinal extent of the volume hologram is already taken into account when we compute eqs. (4.9) and (4.11). In the Wigner space, the Fourier transform of the field corresponds to 90° rotation of the WDF [82], which is equivalent to interchange of the space and spatial frequency variables [76]; the relations are

$$\begin{aligned} \mathcal{W}_3(x_3,u_3,y_3,v_3) &= \mathfrak{F}\left[\mathcal{W}_1(x_1,u_1,y_1,v_1)\right], \quad \text{and} \qquad (4.12) \\ \mathcal{W}_4(x_4,u_4,y_4,v_3) &= \mathfrak{F}^{-1}\left[\mathcal{W}_2(x_2,u_2,y_2,v_2)\right], \qquad (4.13) \end{aligned}$$

where (x_3, y_3) and (x_4, y_4) are the spatial coordinates just before and after the hologram, as shown in Fig. 4-3. Interchanging the variables $x_1 = -\lambda f_1 u_3$, $u_1 = x_3/(\lambda f_1)$, $x_2 = \lambda f_2 u_4$, $u_2 = -x_4/(\lambda f_2)$, $y_1 = -\lambda f_1 v_3$, $v_1 = y_3/(\lambda f_1)$, $y_2 = \lambda f_2 v_4$, and $v_2 = -y_4/(\lambda f_2)$ results in

$$\begin{aligned} \mathcal{W}_4\left(x_4,u_4,y_4,v_4\right) = \iiiint & K_{\mathrm{VH}}(x_4,u_4,y_4,v_4;x_3,u_3,y_3,v_3) \\ & \times \mathcal{W}_3\left(x_3,u_3,y_3,v_3\right) \mathrm{d}x_3 \mathrm{d}u_3 \mathrm{d}y_3 \mathrm{d}v_3, \qquad (4.14) \end{aligned}$$

where

$$\begin{aligned} & K_{\mathrm{VH}}(x_4,u_4,y_4,v_4;x_3,u_3,y_3,v_3) \\ & \quad = K_{\mathrm{VHI}}\left(\frac{u_4}{\lambda f_2}, -\lambda f_2 x_4, \frac{v_4}{\lambda f_2}, -\lambda f_2 y_4; -\frac{u_3}{\lambda f_1}, \lambda f_1 x_3, -\frac{v_3}{\lambda f_1}, \lambda f_1 y_3\right). \qquad (4.15) \end{aligned}$$

Using this procedure, once the refractive index modulation and physical dimensions of volume holograms are known, the Wigner representation of volume holograms can be derived.

In Sec. 4.2.1 and 4.2.2, we use the derived formulae to evaluate the Wigner representations of plane and spherical wave reference volume holograms [7], whose recording geometries are shown in Fig. 4-4. For simplicity, only one–dimensional geometry is considered throughout the derivation, but the extension to two–dimensional geometry is straightforward.

4.2.1 Plane wave reference volume hologram

A slab shape of volume hologram $(a \times L)$ recorded by two plane waves, shown in Fig. 4-4(a), is assumed. The 3D volume holographic pupil (albeit neglecting the

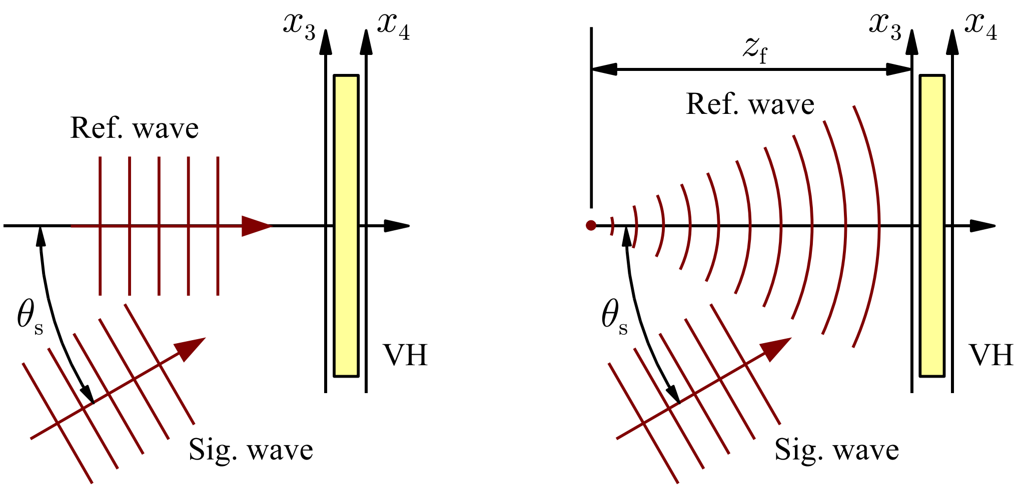

(a) plane wave reference hologram (b) spherical wave reference hologram

Figure 4-4: Recording geometries of volume holograms

second lateral dimension) is given by [27]

$$\epsilon(x'', z'') = \exp\left\{ i\frac{2\pi}{\lambda}\left(\theta_s x'' - \frac{\theta_s^2}{2} z''\right)\right\} \mathrm{rect}\left(\frac{x''}{a}\right) \mathrm{rect}\left(\frac{z''}{L}\right), \tag{4.16}$$

where x'' and z'' are the spatial coordinate inside of the volume hologram. By using the Fourier transform with the proper kernels as in eq. (4.9), the impulse response is

$$h(x_2, y_2; x_1, y_1) = \mathrm{sinc}\left\{\frac{a}{\lambda}\left(\frac{x_1}{f_1} + \frac{x_2}{f_2} - \theta_s\right)\right\} \mathrm{sinc}\left\{\frac{L}{2\lambda}\left(\frac{x_1^2}{f_1^2} - \frac{x_2^2}{f_2^2} + \theta_s^2\right)\right\}. \tag{4.17}$$

In practice, the lateral size of the volume hologram is much larger than the longitudinal extent ($a \gg L$); the first sinc function is approximated as a δ–function, which is equivalent to neglecting diffraction due to the lateral aperture of the hologram. However, the longitudinal extent of the hologram is still taken into account. Also for notational simplicity, $f_1 = f_2 = f$ are used. Then the impulse response is expressed as

$$h(x_2; x_1) \approx \delta\left(x_1 + x_2 - f\theta_s\right) \mathrm{sinc}\left\{\frac{L}{2\lambda f^2}\left(x_1^2 - x_2^2 + f^2\theta_s^2\right)\right\}. \tag{4.18}$$

By using eqs. (4.8) and (4.18), for the 4–f VHI system with the plane wave reference hologram, the double WDF of the impulse response is written as

$$
\begin{aligned}
&K_{\mathrm{VHI}}(x_2,u_2;x_1,u_1)=\iint \mathrm{d}x_2'\mathrm{d}x_1'\mathrm{e}^{-i2\pi\left(u_2x_2'-u_1x_1'\right)}\\
&\times\delta\left(\left[x_1+\tfrac{x_1'}{2}\right]+\left[x_2+\tfrac{x_2'}{2}\right]-f\theta_s\right)\mathrm{sinc}\left\{\frac{L}{2\lambda f^2}\left(\left[x_1+\tfrac{x_1'}{2}\right]^2-\left[x_2+\tfrac{x_2'}{2}\right]^2+f^2\theta_s^2\right)\right\}\\
&\times\delta\left(\left[x_1-\tfrac{x_1'}{2}\right]+\left[x_2-\tfrac{x_2'}{2}\right]-f\theta_s\right)\mathrm{sinc}\left\{\frac{L}{2\lambda f^2}\left(\left[x_1-\tfrac{x_1'}{2}\right]^2-\left[x_2-\tfrac{x_2'}{2}\right]^2+f^2\theta_s^2\right)\right\}.
\end{aligned}
\tag{4.19}
$$

In eq. (4.19), the two δ–functions can be rewritten as

$$
\begin{aligned}
&\delta\left(\left[x_1+\tfrac{x_1'}{2}\right]+\left[x_2+\tfrac{x_2'}{2}\right]-f\theta_s\right)\delta\left(\left[x_1-\tfrac{x_1'}{2}\right]+\left[x_2-\tfrac{x_2'}{2}\right]-f\theta_s\right)\\
&\qquad\qquad=\delta\left(x_1+x_2-f\theta_s\right)\delta\left(x_1'+x_2'\right).
\end{aligned}
\tag{4.20}
$$

By using eq. (4.20), eq. (4.19) is simplified to

$$
\begin{aligned}
K_{\mathrm{VHI}}(x_2,u_2;x_1,u_1)&=\iint \mathrm{d}x_1'\mathrm{d}x_2'\mathrm{e}^{-i2\pi\left(u_2x_2'-u_1x_1'\right)}\delta\left(x_1+x_2-f\theta_s\right)\delta\left(x_1'+x_2'\right)\\
&\quad\times\mathrm{sinc}\left\{\frac{L}{2\lambda f^2}\left[\left(x_1^2-x_2^2\right)+\left(x_1x_1'-x_2x_2'\right)+\left(\frac{x_1'^2}{4}-\frac{x_2'^2}{4}\right)+f^2\theta_{\mathrm{s}}^2\right]\right\}\\
&\quad\times\mathrm{sinc}\left\{\frac{L}{2\lambda f^2}\left[\left(x_1^2-x_2^2\right)-\left(x_1x_1'-x_2x_2'\right)+\left(\frac{x_1'^2}{4}-\frac{x_2'^2}{4}\right)+f^2\theta_{\mathrm{s}}^2\right]\right\}\\
&=\delta\left(x_1+x_2-f\theta_s\right)\int\mathrm{sinc}\left\{\frac{L}{2\lambda f^2}\left[\left(x_1^2-x_2^2\right)+(x_1+x_2)x'+f^2\theta_{\mathrm{s}}^2\right]\right\}\\
&\quad\times\mathrm{sinc}\left\{\frac{L}{2\lambda f^2}\left[\left(x_1^2-x_2^2\right)-(x_1+x_2)x'+f^2\theta_{\mathrm{s}}^2\right]\right\}\mathrm{e}^{-i2\pi(u_2+u_1)x'}\mathrm{d}x'.
\end{aligned}
\tag{4.21}
$$

Equation (4.21) is indeed the Fourier transform of the sinc x' with respect to (u_1+u_2);

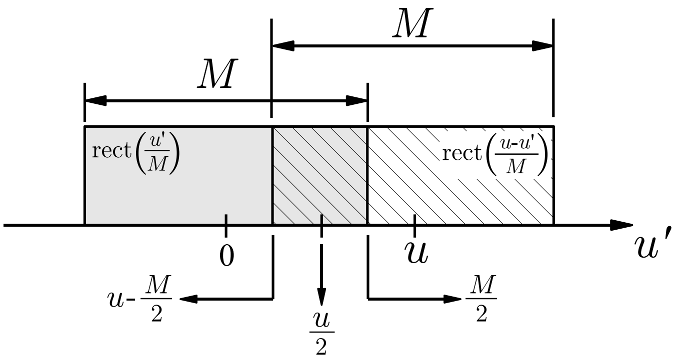

Figure 4-5: Geometrical representation of the two rect functions in eq. (4.23)

it can be expressed as

$$
\begin{aligned}
K_{\mathrm{VHI}}(x_2, u_2; x_1, u_1) &= \delta\left(x_1 + x_2 - f\theta_s\right) \int \operatorname{sinc}\left\{\frac{L}{2\lambda f^2}(x_1+x_2)\left(x' + \frac{x_1^2 - x_2^2 + f^2\theta_{\mathrm{s}}^2}{x_1+x_2}\right)\right\} \\
&\quad \times \operatorname{sinc}\left\{\frac{L}{2\lambda f^2}(x_1+x_2)\left(x' - \frac{x_1^2 - x_2^2 + f^2\theta_{\mathrm{s}}^2}{x_1+x_2}\right)\right\} \mathrm{e}^{-i2\pi(u_2+u_1)x'}\mathrm{d}x' \\
&= \delta\left(x_1 + x_2 - f\theta_s\right)\left(\frac{2\lambda f^2}{L(x_1+x_2)}\right)^2 \left[\operatorname{rect}\left\{\frac{u_1+u_2}{\frac{L}{2\lambda f^2}(x_1+x_2)}\right\}\mathrm{e}^{i2\pi\frac{(x_1^2-x_2^2)+f^2\theta_s^2}{x_1+x_2}(u_1+u_2)}\right] \\
&\quad \otimes\Big|_{(u_1+u_2)} \left[\operatorname{rect}\left\{\frac{u_1+u_2}{\frac{L}{2\lambda f^2}(x_1+x_2)}\right\}\mathrm{e}^{-i2\pi\frac{(x_1^2-x_2^2)+f^2\theta_s^2}{x_1+x_2}(u_1+u_2)}\right],
\end{aligned}
\tag{4.22}
$$

where $\otimes$ denotes convolution. By using $\delta(x_1+x_2-f\theta_{\mathrm{s}})$ and defining $M = L\theta_{\mathrm{s}}/\left(2\lambda f\right)$, $u = u_1 + u_2$, $g(u) = \operatorname{rect}\left(\frac{u}{M}\right)$, and $\phi = 2x_1$, a simpler expression for the convolution part of eq. (4.22) is obtained as

$$
\begin{aligned}
\left\{g(u)\mathrm{e}^{i2\pi\phi u}\right\} \otimes \left\{g(u)\mathrm{e}^{-i2\pi\phi u}\right\} &= \int g(u')\mathrm{e}^{i2\pi\phi u'} g(u-u')\mathrm{e}^{-i2\pi\phi(u-u')}\mathrm{d}u' \\
&= \int \operatorname{rect}\left(\frac{u'}{M}\right)\operatorname{rect}\left(\frac{u-u'}{M}\right)\mathrm{e}^{i2\pi\phi 2u'}\mathrm{e}^{-i2\pi\phi u}\mathrm{d}u' \\
&= \operatorname{rect}\left(\frac{u}{2M}\right)\mathrm{e}^{-i2\pi\phi u}\int \operatorname{rect}\left(\frac{u'-u/2}{M-|u|}\right)\mathrm{e}^{i2\pi\phi 2u'}\mathrm{d}u' \\
&= M\Lambda\left(\frac{u}{M}\right)\operatorname{sinc}\left\{\left(M-|u|\right)4x_1\right\},
\end{aligned}
\tag{4.23}
$$

where $\Lambda(x)$ is a triangle function [5]. Note that the geometrical relation as shown in Fig. 4-5 is used to simplify the two rect functions in eq. (4.23).

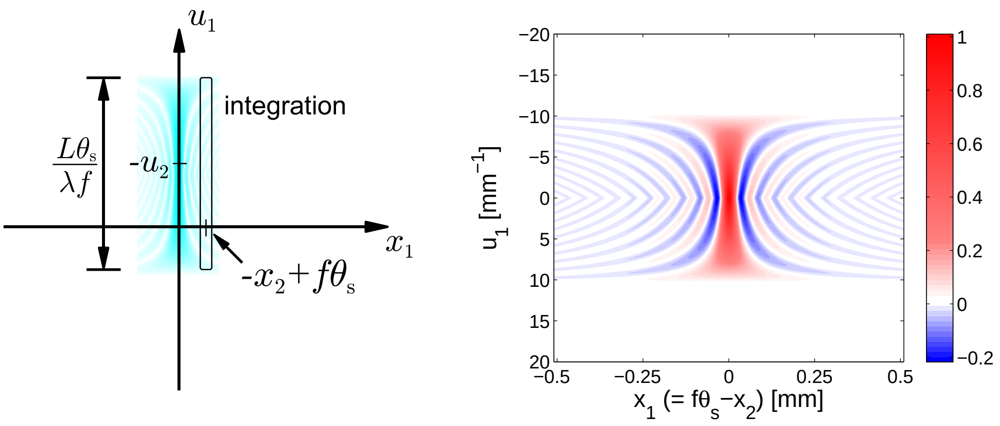

(a) An illustration of K_{VHI} in x_1 and u_2 at a particular x_2 and u_2.

(b) Integration kernel in eq. (4.25) at $x_2 = f\theta_{\mathrm{s}}$ and $u_2 = 0$.

Figure 4-6: Wigner representation of the VHI system with a plane wave reference hologram. In (b), $f = 50\,\mathrm{mm}$, $\lambda = 0.5\,\mu\mathrm{m}$, $\theta_{\mathrm{s}} = 30°$, and $L = 1\,\mathrm{mm}$.

By using eq. (4.23), the WDF representation of the VHI system is

$$K_{\mathrm{VHI}}(x_2,u_2;x_1,u_1) = \left(\frac{2\lambda f}{L\theta_{\mathrm{s}}}\right)\delta\left(x_1+x_2-f\theta_s\right)\Lambda\left(\frac{2\lambda f}{L\theta_{\mathrm{s}}}(u_1+u_2)\right) \times \mathrm{sinc}\left\{\left(\frac{L\theta_{\mathrm{s}}}{\lambda f}-2|u_1+u_2|\right)2x_1\right\}. \tag{4.24}$$

Finally, the WDF representation of the 4–f volume holographic imaging system is

$$\begin{aligned}\mathcal{W}_2(x_2,u_2) &= \iint K_{\mathrm{VHI}}(x_2,u_2;x_1,u_1)\mathcal{W}_1(x_1,u_1)\mathrm{d}x_1\mathrm{d}u_1\\ &= \frac{2\lambda f}{L\theta_{\mathrm{s}}}\int \Lambda\left(\frac{u_1+u_2}{L\theta/(2\lambda f)}\right)\mathrm{sinc}\left\{2\left(\frac{L\theta_{\mathrm{s}}}{\lambda f}-2|u_1+u_2|\right)x_1\right\}\mathcal{W}_1(x_1,u_1)\mathrm{d}u_1,\end{aligned} \tag{4.25}$$

where $x_2 = f\theta_{\mathrm{s}} - x_1$.

For a given x_2 and u_2, x_1 is equal to $-x_2 + f\theta_{\mathrm{s}}$. The triangle function limits the range of the integration of u_1 to $-u_2 - M < u_1 < -u_2 + M$ as shown in Fig. 4-6(a). If $u_1 + u_2 = 0$, the scale factor of the sinc is maximized and the width is minimized. Figure 4-6 shows the integration kernel of eq. (4.25) at $x_2 = f\theta_{\mathrm{s}}$ and $u_2 = 0$. Note that the sinc function is only dependent on x_1 not $x_2 - x_1$, which indicates the strongly shift variant nature of the system, and that some values of K_{VHI} are negative.

For the plane wave reference volume hologram, the Wigner representation of the

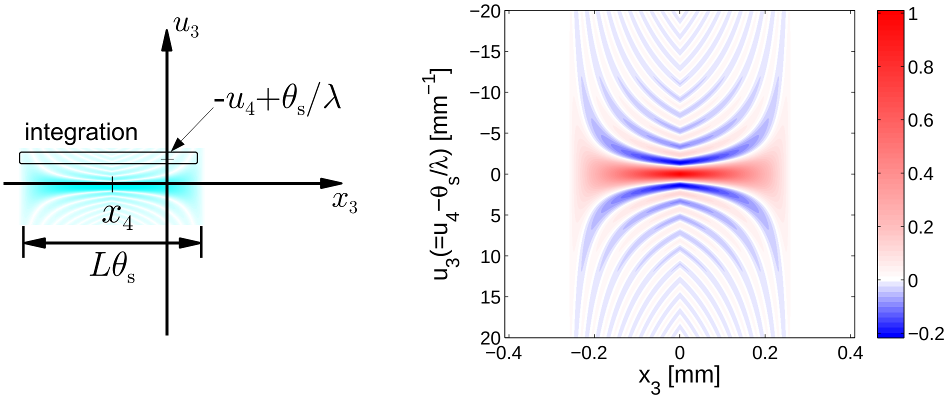

(a) An illustration of K_{VH} in x_3 and u_3 at a particular x_4 and u_4.

(b) Integration kernel in eq. (4.27) at $x_4 = 0$ and $u_4 = \theta_s/\lambda$.

Figure 4-7: Wigner representation the plane wave reference volume hologram. In (b), parameters are $\lambda = 0.5\,\mu$m, $\theta_s = 30°$, and $L = 1$ mm.

impulse response is obtained by using eq. (4.15) as

$$K_{\mathrm{VH}}(x_4, u_4; x_3, u_3) = \left(\frac{2}{L\theta_s}\right) \delta\left(u_4 - u_3 - \frac{\theta_s}{\lambda}\right) \Lambda\left(\frac{x_3 - x_4}{L\theta_s/2}\right) \operatorname{sinc}\left\{2\left(L\theta_s - 2|x_3 - x_4|\right) u_3\right\}. \tag{4.26}$$

Hence, the Wigner representation of the plane wave reference volume hologram is

$$\begin{aligned} \mathcal{W}_4(x_4, u_4) &= \iint K_{\mathrm{VH}}(x_4, u_4; x_3, u_3) \mathcal{W}_3(x_3, u_3) \mathrm{d}x_3 \mathrm{d}u_3 \\ &= \left(\frac{2\lambda f}{L\theta_s}\right) \int \Lambda\left(\frac{x_3 - x_4}{L\theta_s/2}\right) \operatorname{sinc}\left\{2\left(L\theta_s - 2|x_3 - x_4|\right)\left(u_4 - \frac{\theta_s}{\lambda}\right)\right\} \mathcal{W}_3\left(x_3, u_4 - \frac{\theta_s}{\lambda}\right) \mathrm{d}x_3. \end{aligned} \tag{4.27}$$

For a given x_4 and u_4, u_3 is equal to $u_4 - \theta_s/\lambda$ due to the δ–function. The triangular function limits the integration range of x_3 within $x_4 - L\theta_s/2 < x_3 < x_4 + L\theta_s/2$ as shown in Fig. 4-7(a). This range of integration is dependent on the hologram thickness L and the angle θ_s. Note that eq. (4.27) is a multiplication along u_4 but a convolution along x_4. Figure 4-7(b) shows the integration kernel of eq. (4.27), which describes the space–spatial frequency response of the plane wave reference volume hologram. Since the hologram is recorded by two plane waves, the double WDF of the hologram has high values near $u_3 = 0$ and $u_4 = \theta_s/\lambda$, as expected.

In the Wigner space, the intensity is the projection of the WDF along the u–axis [76]. Thus, the Bragg diffraction intensity image of the 4–f VHI system can be calculated from eqs. (4.25) and (4.24). Assuming the input wave is infinitely extended incoherent light ($\mathcal{W}(x_1, u_1) = 1$), then

$$\begin{aligned} I_2(x_2) &\sim \iint \Lambda\left(\frac{2\lambda f}{L\theta_{\mathrm{s}}}(u_1+u_2)\right) \mathrm{sinc}\left\{\left(\frac{L\theta_{\mathrm{s}}}{\lambda f} - 2|u_1+u_2|\right) 2(f\theta_{\mathrm{s}} - x_2)\right\} \mathrm{d}u_1 \mathrm{d}u_2 \\ &\sim \mathrm{sinc}^2\left\{\frac{L\theta_{\mathrm{s}}}{\lambda f}(f\theta_{\mathrm{s}} - x_2)\right\}, \end{aligned} \tag{4.28}$$

which agrees with the previously reported result [26]. A detailed derivation can be found in Appendix A.

4.2.2 Spherical wave reference volume hologram

A spherical wave reference volume hologram is recorded by a plane signal wave and spherical reference wave [7] as shown in Fig. 4-4(b). The signal wave is a plane wave propagating with an angle θ_{s} with respect to the optical axis, and the reference wave is a spherical wave originating from a point source. It is interesting that the grating vector of the spherical wave reference hologram is shift variant. Hence, the Wigner representation, which describes both spatial and frequency characteristics, provides detailed characteristics of the shift variant Bragg diffraction.

The 2D volume holographic pupil function of the spherical wave reference hologram is written as [7]

$$\begin{aligned} \epsilon(x'', z'') = \exp&\left\{-i\frac{\pi}{\lambda}\frac{x''^2}{z''-z_{\mathrm{f}}}\right\} \exp\left\{-i\frac{\pi}{\lambda}\theta_{\mathrm{s}}^2 z''\right\} \exp\left\{i\frac{2\pi}{\lambda}\theta_{\mathrm{s}} x''\right\} \\ &\times \mathrm{rect}\left(\frac{x''}{a}\right) \mathrm{rect}\left(\frac{z''}{L}\right), \end{aligned} \tag{4.29}$$

where z_{f} is the distance from the hologram and the point source radiating the spherical wave on the optical axis and other parameters are identical the plane wave reference hologram. Similar to the plane reference wave hologram, $f_1 = f_2 = f$ and large a are assumed, and the diffraction due to the lateral aperture of the hologram is ignored for convenience. For the 4–f VHI system with the spherical wave reference hologram, the impulse response is given by

$$h(x_2; x_1) = \exp\left\{-i\frac{\pi}{\lambda}\frac{z_f}{f^2}\left(x_1 + x_2 - f\theta_{\mathrm{s}}\right)^2\right\}\mathrm{sinc}\left\{\frac{L}{\lambda f^2}\left(x_1 + x_2\right)\left(x_2 - f\theta_{\mathrm{s}}\right)\right\}. \quad (4.30)$$

The double Wigner representation of the impulse response is computed as

$$\begin{aligned} K_{\mathrm{VHI}}(x_2, u_2; x_1, u_1) = & \iint \mathrm{d}x_2'\mathrm{d}x_1'\mathrm{e}^{-i2\pi(x_2'u_2 - x_1'u_1)} \\ & \times \exp\left\{-i\frac{2\pi}{\lambda}\frac{z_f}{f^2}\left(x_1' + x_2'\right)\left(x_1 + x_2 - f\theta_{\mathrm{s}}\right)\right\} \\ & \times \mathrm{sinc}\left\{\frac{L}{\lambda f^2}\left(x_1 + x_2 + \tfrac{x_1'+x_2'}{2}\right)\left(x_2 + \tfrac{x_2'}{2} - f\theta_{\mathrm{s}}\right)\right\} \\ & \times \mathrm{sinc}\left\{\frac{L}{\lambda f^2}\left(x_1 + x_2 - \tfrac{x_1'+x_2'}{2}\right)\left(x_2 - \tfrac{x_2'}{2} - f\theta_{\mathrm{s}}\right)\right\}. \quad (4.31) \end{aligned}$$

$K_{\mathrm{VHI}}(x_4 = 0, u_4 = \theta_{\mathrm{s}}/\lambda; x_3, u_3)$ is numerically integrated for the spherical wave reference hologram whose L=1 mm and $\theta_{\mathrm{s}} = 30°$ and plotted in Fig. 4-8(a).

Using eqs. (4.15) and (4.31), the double WDF of the volume hologram is obtained as

$$\begin{aligned} K_{\mathrm{VH}}(x_4, u_4; x_3, u_3) = & \iint \mathrm{d}x_3'\mathrm{d}x_4'\mathrm{e}^{-i2\pi(u_4'x_4 - u_3'x_3)} \\ & \times \exp\left\{-i2\pi\lambda z_f\left(u_3' + u_4'\right)\left(-u_3 + u_4 - \frac{\theta_{\mathrm{s}}}{\lambda}\right)\right\} \\ & \times \mathrm{sinc}\left\{L\lambda\left(-u_3 + u_4 + \frac{u_3' + u_4'}{2}\right)\left(u_4 + \frac{u_4'}{2} - \frac{\theta_{\mathrm{s}}}{\lambda}\right)\right\} \\ & \times \mathrm{sinc}\left\{L\lambda\left(-u_3 + u_4 - \frac{u_3' + u_4'}{2}\right)\left(u_4 - \frac{u_4'}{2} - \frac{\theta_{\mathrm{s}}}{\lambda}\right)\right\}. \quad (4.32) \end{aligned}$$

$K_{\mathrm{VH}}(x_4 = 0, u_4 = \theta_{\mathrm{s}}/\lambda; x_3, u_3)$ is numerically integrated with $z_{\mathrm{f}} = 50$ mm, $L = 1$, and $\theta_{\mathrm{s}} = 30°$. In Fig. 4-8(b), since $x_4 = 0$ and $u_4 = \theta_{\mathrm{s}}/\lambda$, strong Bragg diffraction is generated and x_3 and u_3 should be confined near $x_3 = u_3 = 0$. Note that the WDF is not horizontal, which indicates the incoming wave should be a spherical wave. Thus, this system requires a spherical wave to be Bragg matched, as expected.

Comparing the Wigner representation of the plane and spherical wave reference

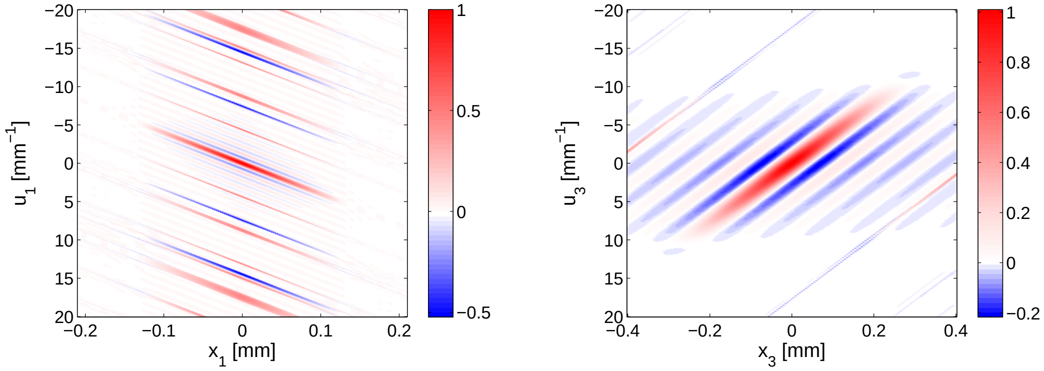

(a) $K_{\mathrm{VHI}}(x_2 = 0, u_2 = \theta_{\mathrm{s}}/\lambda, x_1, u_1)$.

(b) $K_{\mathrm{VH}}(x_4 = 0, u_4 = \theta_{\mathrm{s}}/\lambda, x_3, u_3)$.

Figure 4-8: Wigner representation of the spherical wave reference hologram and VHI system with $\lambda = 0.5\,\mu\mathrm{m}$, $\theta_{\mathrm{s}} = 30°$, $z_{\mathrm{f}} = 50\,\mathrm{mm}$, and $L = 1\,\mathrm{mm}$.

hologram, a few differences are noticed. As the WDF of both input and output field are 4D quantities of (x, u, y, v), the input–output relation is an 8D transform as in eq. (4.7). However, in the plane wave reference hologram, K_{VH} and K_{VHI} are related by a multiplication in one direction and convolution in the other direction, which ends up with a 6D transform. The spherical reference volume hologram is still an 8D transform as shown in eqs. (4.31) and (4.32).

4.3 Shift variance vs. axial imaging capability

In this section, the axial imaging process, i.e., imaging methods that are able to extract depth information of a scene, are explored with the Wigner analysis. In traditional imaging systems such as photographic cameras, the point spread functions are designed to be as shift invariant as possible. In other words, identical images are formed regardless of the lateral position of objects. Although many optical imaging systems in practice are not precisely shift invariant, they often are assumed to be shift invariant for easier analysis, which allows the use of linear shift invariant system approaches or frequency analysis, such as OTF.

Stein and Barbastathis conjectured that axial imaging requires a shift variant point spread function [87]. A few examples were presented to support their claim; confocal microscopes and stereo vision systems have strongly shift variant imaging

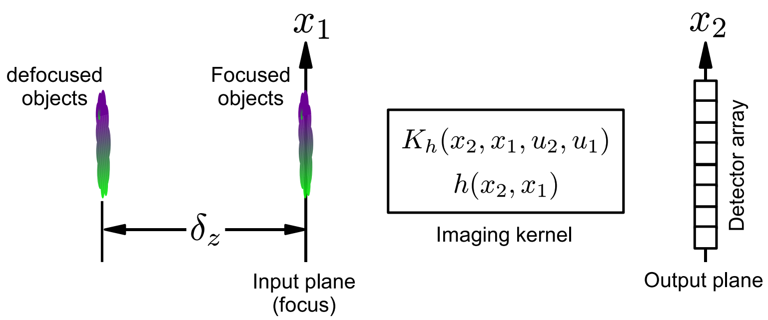

Figure 4-9: Axial imaging scenario. At the input plane, the defocus δ_z produces x–shear of the WDF. At the output plane, a array of photodetectors are placed.

kernels with respect to defocus. While the claim is reasonable, it was not proven in that early work. In this section, the Wigner analysis is applied to the axial imaging process and the Stein–Barbastathis claim is rigorously proven. Although only one–dimensional lateral geometry is considered throughout the analysis, the extension to two–dimensional geometry is straightforward. Incoherent incoming light is also assumed because most conventional imaging systems, especially passive imaging systems, work under incoherent light.

First an imaging scenario as shown in Fig. 4-9 is considered. The imaging system is given by $K_h(x_2, u_2; x_1, u_1)$, which is the double Wigner distribution function of the impulse response $h(x_2; x_1)$ [86]. Since shift variance/invariance are being investigated, a photodetector array camera is presumably located at the output plane to measure intensity. At the input plane, the defocus produces the x–shear of the WDF; hence, the goal of axial imaging is to measure the slope of the sheared WDF from intensity measurements at the output plane.

Next it is investigated how differently the shift invariant/variant kernels affect the imaging process. Detailed derivations can be found in Appendix B.

4.3.1 Shift invariant system

If the system is shift invariant, then the output field is a convolution of the input field and the impulse response as

$$E_2(x_2) = \int E_1(x_1)h(x_2 - x_1)\mathrm{d}x_1. \tag{4.33}$$

By applying the definition of the WDF to both sides of eq. (4.33), the input–output relation is expressed in Wigner space as

$$\mathcal{W}_2(x_2, u_2) = \int K_{\mathrm{si}}(x_2 - x_1, u_2)\mathcal{W}_1(x_1, u_2)\mathrm{d}x_1, \tag{4.34}$$

where

$$K_{\mathrm{si}}(x_2 - p, u_2) = \int h(x_2 - p + \tfrac{t}{2})h^*(x_2 - p - \tfrac{t}{2})\mathrm{e}^{-i2\pi u_2 t}\mathrm{d}t. \tag{4.35}$$

Note that the WDF of the output field is a convolution of K_{si} and $\mathcal{W}_1$ in x and a multiplication in u. The intensity of the output field is computed as

$$I_2(x_2) = \int \mathcal{W}_2(x_2, u_2)\mathrm{d}u_2 = \iint K_{\mathrm{si}}(x_2 - x_1, u_2)\mathcal{W}_1(x_1, u_2)\mathrm{d}x_1\mathrm{d}u_2. \tag{4.36}$$

4.3.2 Shift variant system

For a shift variant system, the input–output relation is represented as an integral with a shift variant impulse response as

$$E_2(x_2) = \int E_1(x_1)h(x_2; x_1)\mathrm{d}x_1. \tag{4.37}$$

By applying the definition of the WDF to both sides of eq. (4.37) as in Sec. 4.3.1, the input–output relation in Wigner space is obtained as

$$\mathcal{W}_2(x_2, u_2) = \iint K_{\mathrm{sv}}(x_2, u_2; x_1, u_1)\mathcal{W}_1(x_1, u_1)\mathrm{d}x_1\mathrm{d}u_1, \tag{4.38}$$

where

$$K_{\rm sv}(x_2,u_2;x_1,u_1)=\iint h(x_2+\tfrac{\xi}{2};x_1+\tfrac{\eta}{2})h^*(x_2-\tfrac{\xi}{2};x_1-\tfrac{\eta}{2})\mathrm{e}^{-i2\pi(u_2\xi-u_1\eta)}\mathrm{d}\xi\mathrm{d}\eta. \quad (4.39)$$

The WDF of the output field is computed by the double integrations of $K_{\rm sv}$ and $\mathcal{W}_1$. The intensity of the output field is

$$I_2(x_2)=\int \mathcal{W}_2(x_2,u_2)\mathrm{d}u_2=\iiint K_{\rm sv}(x_2,u_2,x_1,u_1)\mathcal{W}_1(x_1,u_1)\mathrm{d}x_1\mathrm{d}u_1\mathrm{d}u_2. \quad (4.40)$$

4.3.3 Comparison in the WDF space

Comparing eqs. (4.34) and (4.38), two main differences are noticed: 1) $K_{\rm sv}$ is the double WDF whereas $K_{\rm si}$ is a single WDF. 2) In eq. (4.34), there is no dependency on u_1. In other words, the variation of $\mathcal{W}_1$ along u appears directly in $\mathcal{W}_2$ for shift invariant systems. However, in eq. (4.38), $K_{\rm sv}$ is dependent on both u_1 and u_2.

To clearly understand these differences, the concept of the forward/backward imaging process is brought up, as shown in Fig. 4-10. In forward imaging, the input WDF is transformed by the imaging system and mapped to the output plane. In our imaging scenario, an array of photodetectors at the output plane measures intensity, which corresponds to the projection of the output WDF along the u direction. Depending on the size and spacing between the photodetector pixels, integration kernels corresponding to each photodetector pixel are constructed. Now the backward imaging process, where the integration kernels are back–projected onto the input plane, is considered. Depending on the characteristics of the imaging system, the integration kernels at the input plane could have arbitrary shapes or even multiple segments.

In the context of this forward/backward imaging, the difference between the shift variant and invariant imaging kernels can be visualized as Fig. 4-10. Since $K_{\rm si}$ is independent on u_1, at the input plane the integration kernels of every photodetector pixel are all identical except for a lateral shift along x_1. Even though each kernel may have variations along u_1, all kernels have the same variation and identical extent along u_1 as shown in Fig. 4-11(a). On the contrary, in shift variant systems, $K_{\rm sv}$ is

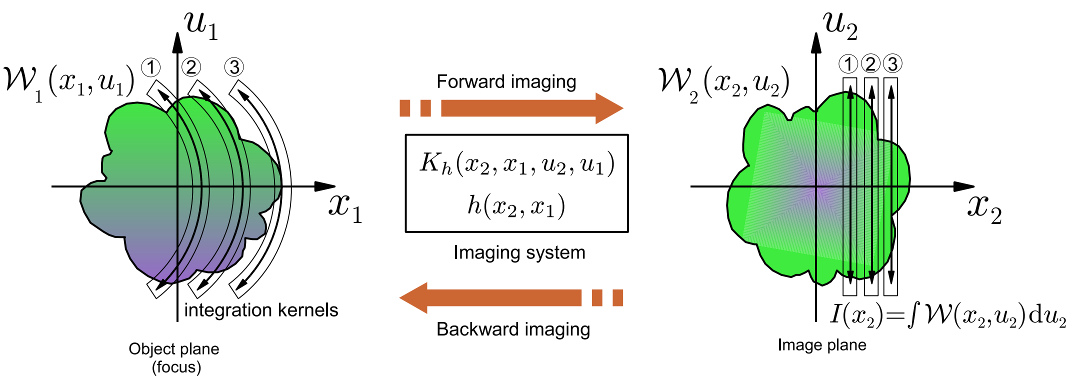

Figure 4-10: Forward/Backward imaging in Wigner space. The intensity integration kernels at the output plane are back–projected onto the input plane.

dependent on u_1, which implies that the integration kernel at the input plane also depends on u_1 (and x_1). Every integration kernel may be different from each other as shown in Fig. 4-11(b).

4.3.4 Axial imaging conditions in the WDF space

In this section, we investigate axial imaging systems, which estimate the depth information from intensity measurements; two conditions for axial imaging are established. In the backward imaging process, the shape and configuration of the integration kernels are particularly interesting. In computer vision and graphics, a concept similar to the Wigner distribution function has been used, referred to as *light field*. Levin *et al.* used the light field concept to analyze the trade–off of various camera systems [88], which is identical to the integration kernels appeared at the input plane in the backward imaging process. Figure 4-12 shows the light field analysis for various camera systems. In the light fields formulation, the vertical axis is the second plane, which corresponds to u in Wigner space.

In the same context of the backward imaging, the color coded rectangles indicate the integration kernels of the individual photodetector arrays at the input plane. In the object space, three objects are assumed (Fig. 4-12(a)): one in focus, one behind the focus and one in front. The light fields of the three objects are shown in Fig. 4-12(b), where three different strips with different slopes exist. The integration kernels

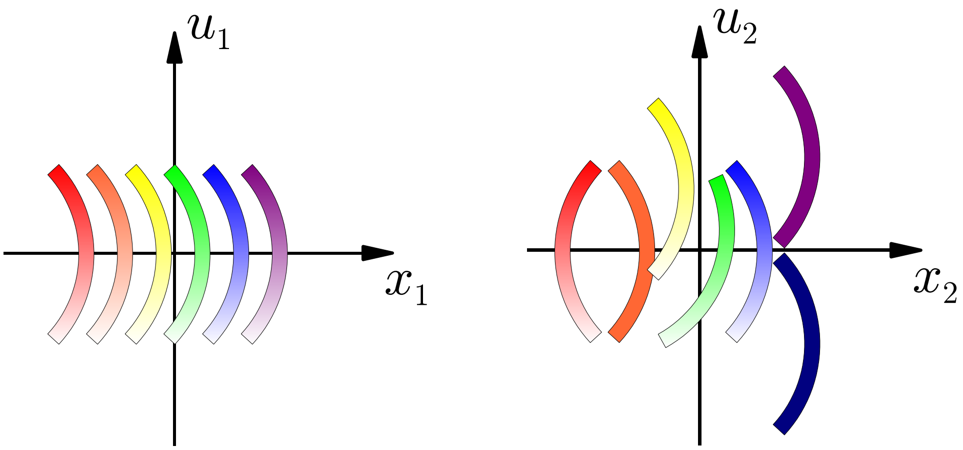

(a) shift invariant (b) shift variant

Figure 4-11: Comparison of shift invariant and variant kernels. In shift invariant systems, (a), the integration kernels are all identical. In shift variant system, (b), the kernels could be different in shape, offset, weighting, and size.

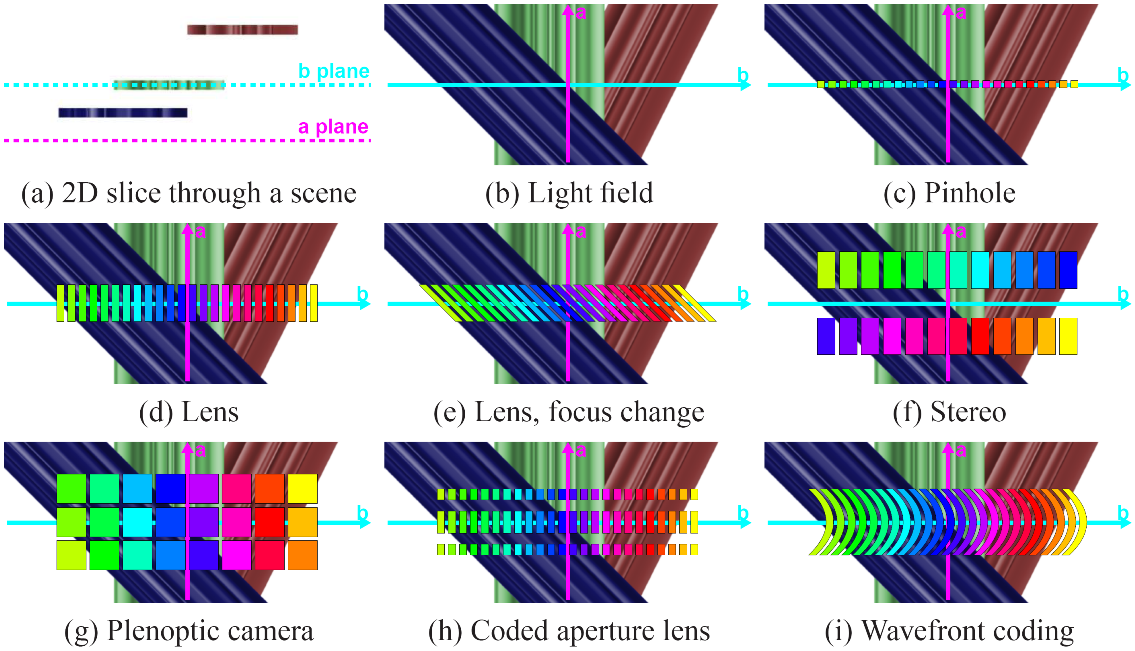

(a) 2D slice through a scene (b) Light field (c) Pinhole (d) Lens (e) Lens, focus change (f) Stereo (g) Plenoptic camera (h) Coded aperture lens (i) Wavefront coding

Figure 4-12: Light field analysis of various axial imaging methods for three depths [88] for a pin–hole camera are shown in Fig. 4-12(c). Vertical extent of the kernel is very limited; it explains why pin–hole cameras have infinite depth of field because the shear of the WDF does not affect intensity patterns. Figure 4-12(d) shows the integration kernels of traditional cameras. All the kernels are vertically straight and equally spaced. Due to the finite aperture, each integration kernel has a limited range in the u–direction. Figure 4-12(e) shows the integration kernels of traditional cameras with focus change. Since the defocus corresponds to x–shear in the WDF domain, the integration kernels get sheared. Fig. 4-12(f) corresponds to a stereo vision system [46], in which two cameras have different perspectives. Since the integration kernels sample different u–components, the stereo vision cameras can estimate the slope of the WDF. Figure 4-12(g) shows the integration kernels of the plenoptic cameras [89, 90], in which the system sacrifices spatial resolution and acquires more angular information of incoming rays. Similar to the stereo vision system, the plenoptic camera is also able to measure the slope of the WDF. Figure 4-12(h) shows the integration kernels of a coded aperture system [91, 92]. The idea is to produce different scale of blurs depending on the defocus (the slope of the WDF), where the depth could be inferred for *priori*–known objects; for example, particle imaging. Figure 4-12(i) shows the integration kernels of the cubic phase mask system [1, 93], where the cubic phase mask produces curved integration kernels so that the intensity change is less sensitive to the shear of the WDF.

As explained in Fig. 4-9, to achieve axial imaging, the system should be able to estimate the slope of the WDF. The stereo vision system shown in Fig. 4-12(f) and the plenoptic camera in Fig. 4-12(g) have axial imaging capability for extended objects. The coded aperture camera shown in Fig. 4-12(h) may be used for inferring depth, but it inherently has an ambiguity between depth and objects with specific patterns. Hence, the integration kernels should be distributed along the u axis in Wigner space to implement axial imaging. One typical arrangement is, as demonstrated by stereo vision and plenoptic cameras, that at least two integration kernels should exist at a given x position.

Based on this analysis, two major conditions are established for achieving axial imaging:

1. Objects must be either shift variant or localized.

2. Shift variant imaging kernels must be properly located in Wigner space.

The first condition is obvious; if the object is featureless, then the sheared WDF cannot be traced, where intensity based passive axial imaging fails. To create shift variance (or localization) of objects, active illumination can be used as in confocal microscopes [43] or laser triangulation [94], or objects are assumed to have some features, patterns, or structures in passive vision methods. The second condition is described in the earlier discussion. The imaging kernels should be properly distributed along u direction in Wigner space to estimate the slope of the sheared WDF, which requires shift variant imaging kernels because integration kernels should have different variation along u. Note that the shift variant imaging kernel is just a necessary condition; not all shift variant systems are able to achieve axial imaging.

4.4 Conclusion

In this chapter, Winger analysis, which describes both space and spatial frequency information of light, is introduced. The Wigner representation for VHI systems and volume holograms are derived. The Wigner analysis fully describes the shift variant Bragg diffraction property of volume holograms. Then, the Wigner analysis was extended to axial imaging. Since defocus introduces the x–shear in Wigner space, on axial imaging capability requires estimating of the slope of the sheared WDF. The concept of the backward imaging was introduced and the imaging kernels of various imaging systems were investigated. It turned out that axial imaging requires two conditions: 1) shift variant objects and 2) properly designed shift variant imaging kernels. Hence, axial imaging necessitates the shift variant imaging kernels.

The shift variance property of volume holograms can be tuned by recording process, which is a posteriori motivation for their use in axial imaging. In the context of backward imaging, there are two interesting future research topics: 1) how to determine desired integration kernels for a given imaging scenario, and 2) how to design imaging kernels to achieve the desired integration kernels.

Chapter 5

Conclusion

As semiconductor fabrication technology progresses, a variety of sensors and cameras with different formats, spectral ranges, and space–bandwidth products are available in commercial markets. Powerful computational resources enable various complicated post–processing methods. This progress will be exploited in multi–dimensional imaging; smart sensors and computational cameras are representative examples.

Shift variant and multiplexed imaging are efficient ways to implement multi–dimensional imaging because multi–dimensional information can be transformed and compressed in a way that post–processing can decode the captured information. Since volume holograms exhibit both properties, it is interesting to analyze the behavior of volume holograms as they are exploited in different imaging platforms. In this thesis, various aspects of volume holograms have been explored. Traditionally, volume holograms have been used in holographic data storage [8–11], optical interconnects [12], and artificial neural networks [13]. However, as shown in our earlier research, volume holograms can be used as 3D optical elements as well. By specifically engineering the shift variance and multiplexing, novel multi–dimensional imaging systems have been implemented [7, 15–25]. Based on the analysis and implementation as presented, we hope that volume holograms can be used more actively in various multi–dimensional imaging systems: computational cameras, computational imaging, and space imaging.

To conclude this thesis, all the presented topics are summarized and intended future research directions are presented.

5.1 Summary

5.1.1 Volume diffraction formulation

Two formulations of analyzing volume diffraction were presented: the k–sphere method and wave optics approach. The k–sphere method is a geometrical construction of the Bragg match/mismatch, which is a fast and intuitive method. The k–sphere method was integrated with the ray tracing software ZEMAX®. The built–in analysis tools and optimization routines provide a greater versatility and flexibility in the design process. Three examples were demonstrated: reproducing a longitudinal PSF of the 4–f VHI system, analyzing the effect of aberration, and optimizing an objective lens to exhibit stronger Bragg diffraction. The implementation can handle both transmission and reflection holograms as well as slanted and unslanted holograms. More importantly, the integrated k-sphere model computes Bragg diffraction efficiently for shift variant holograms, which is not easy for the wave optics based formulations.

The k–sphere formulation was examined in 3D space to understand why the Bragg diffraction images are curved. By solving the k–sphere method analytically, the equation of the curved Bragg diffraction images were derived; generally, the form is distorted ellipses, depending on the optical system parameters.

The scalar diffraction theory was revisited. By using this formulation, a general form of the shift variant impulse response of VHI systems was derived. The result clearly explains the difference between traditional and VHI systems, in which the volume holographic element behaves as a 3D pupil and the additional dimension introduces a strong shift variant response to the VHI systems.

5.1.2 Passive binary depth detection

For VHI systems, by extending the scalar diffraction theory into statistical optics, the partially coherent response was derived. Specifically, the VHI system with a slab–shaped hologram was examined in detail. As an application of the partially coherent responses of VHI systems, a new passive depth detection method was proposed, based on spatial coherence measurements. If objects are spatially incoherent, the degree of coherence increases as light propagates. Our method detects the spatial coherence change due to defocus. The imaging scenario was binarized with the intention of discriminating two depths, foreground and background. The volume hologram imposes a spatially variant wavelength filter on the input plane and separates light spatially and spectrally. From an experimental setup with a volume holographic interferometer, spatial coherence measurements were implemented for quasi–monochromatic light. For broadband light, the system was modified to improve the field of view and spectral blur by inserting a diffraction grating. Then the cross spectral density was recovered by taking the Fourier transform. The cross spectral density of the field diffracted by the volume hologram encodes both depth and lateral information of a scene. The binary depth discrimination capability has been demonstrated for flat uniform featureless objects under both quasi–monochromatic and broadband illumination.

5.1.3 Wigner analysis

The Wigner distribution function for volume holograms was introduced. Basic properties and advantages of using the Wigner analysis were presented. While the Wigner representations of thin transparencies such as lenses, gratings, apertures, and phase masks have already been reported, the Wigner representation of volume holograms has not been derived because the volume holograms are volumetric optical elements. Using a linear system approach, we established how to derive the Wigner representation of volume holograms and VHI systems. The WDF of volume holograms describes well the shift variant nature of volume holograms in Wigner space.

The Wigner analysis was applied to explore the axial imaging process, in which depth information of a scene is obtained from captured intensity images. We explored the shift variant/invariant imaging kernels in Wigner space. The backward imaging and integration kernels are introduced; the shift invariant systems have identical integration kernels at the input plane whereas the shift variant systems have shift variant integration kennels, especially along the spatial frequency axis. By using the same analysis, various imaging systems were examined and two important conditions for achieving the axial imaging were established: 1) shift variant (or localized) objects and 2) properly designed shift variant imaging kernels. The previously reported conjecture, that axial imaging necessitates the loss of shift invariance, was proved rigorously.

5.2 Future work

5.2.1 Volume diffraction formulation

- **Absolute efficiency in the k–sphere method**: Although the current computational module can handle many different holograms including the ones with shift variant grating vectors, the diffraction efficiency is still a relative quantity. To include the absolute efficiency, more rigorous analysis such as coupled wave theory [39] which computes the absolute diffraction efficiency from material parameters and hologram specifications should be integrated.

- **Crosstalk between multiplexed holograms in the k–sphere method**: The current module handles multiplexed holograms independently; in practice crosstalk between holograms exists. The crosstalk should be taken into account in a way that all the multiplexed holograms are probed by a probe beam simultaneously. Optimization routines can then utilize optical design tools to minimize crosstalk.

- **WDF representation in the k–sphere method**: Using the WDF representation of the volume hologram, the WDF potentially can be integrated in ray tracing software as well.

- **Faster computation of the 3D Fourier transform approach**: As pointed out, the 3D Fourier transform method described in Sec. 2.3 is a straightforward method; however, enormous computational resources are required. To reduce the computational complexity, some constraints such as symmetry of the refractive index modulation may be exploited.

5.2.2 Passive binary depth detection

- **More rigorous system performance characterization**: Even though the passive binary depth detection was demonstrated, the effect of system parameters still has not been well characterized. The depth resolving capability depends on many parameters such as the degree of coherence of imaged objects, defocus distance, object size, the size of the aperture, focal lengths of the lenses, and the noise characteristics of the interferometric measurements. Also it depends on the current detection method, which measures spatial coherence at the shear center $\Delta x = 0$. A full-blown design methodology and optimization has been outside the scope of the thesis; the topic itself is very rich and can form the basis of several graduate theses in the future.

- **Better dispersion matching**: Currently, an off the shelf diffraction grating and two additional lenses were used to compensate the dispersion caused by the volume hologram; it is not perfectly matched. To achieve better dispersion matching, either the volume hologram or the diffraction grating should be customized, including joint maximization of their diffraction efficiencies.

- **Non–uniform/multiple objects**: Although the depth resolving capability was demonstrated for featureless objects, many objects in real world have features. It is worthwhile to explore how the system performs differently for non–uniform scene including scenes with multiple objects.

- **Spectra of objects**: In the experiments, the FG and BG objects had identical spectra. If they have different spectra then the spectrum of the each object should be measured for calibration as pointed in Sec. 3.3.2.

- **Robust design and hybrid system**: The cross spectral density measurements are inherently interferometric measurements. In field applications, this limits the practicability because the interferometer is very sensitive to environmental factors: vibrations, temperature changes, air flows, *etc.* Thus, there needs be a smarter structure which is more robust to disturbances or a completely different system configuration. To bring more practicability and versatility into applications, we might consider hybrid systems, in which traditional imaging systems are combined with the proposed depth sensitive measurement. Another possibility is to use the zeroth diffraction order. Currently, the zeroth order diffraction is not used at all and the space bandwidth product of the CCD is not fully used, and it could be utilized to measure regular intensity images or spectrum of light with the zeroth order or CCD pixels not being used.

5.2.3 Wigner analysis

- **Wigner representation of multiplexed holograms**: The current representation does not include multiplexed holograms. If multiplexed holograms are described in Wigner space, the space–spatial frequency characteristics of crosstalk can be investigated.

- **New applications**: The WDF can be used for analyzing and designing new optical systems such as 3D displays or digital holographic particle imaging. It would be interesting to explore the wavefront coding systems with both amplitude and phase masks, in which the WDF and the ambiguity function could be exploited.

- **Analysis of partially coherent light**: The current formulation only deals with coherent light. Since the WDF can be used with partially coherent light, it would be very interesting to explore the spatial coherence change in various imaging systems.

- **Depth resolution in Wigner space**: The depth resolution in Wigner space may be defined as the minimum slope change of the WDF that the system can resolve. It would be interesting to investigate the depth resolution of various axial imaging systems in Wigner space, especially in connection with their respective amount of shift variance.

Appendix A

Derivation of Eq. (4.28)

This derivation demonstrates how the intensity of the Bragg diffraction image is obtained from the Wigner analysis in the 4–f VHI system.

$$\begin{aligned}
I(x_2) = \int \mathcal{W}(x_2, u_2)\mathrm{d}u_2 &= \iint \Lambda\left(\frac{u_1+u_2}{M}\right) \operatorname{sinc}\left\{(M - |u_1+u_2|)\, 4x_1\right\} \mathrm{d}u_1 \mathrm{d}u_2 \\
&= \int \Bigg[\int_{-u_1-M}^{-u_1} (M+u_1+u_2) \operatorname{sinc}\left\{(M+u_1+u_2)\, 4x_1\right\} \mathrm{d}u_2 \\
&\qquad + \int_{-u_1}^{-u_1+M} (M-u_1-u_2) \operatorname{sinc}\left\{(M-u_1-u_2)\, 4x_1\right\} \mathrm{d}u_2 \Bigg] \mathrm{d}u_1 \\
&= \int \Bigg[\frac{1}{4\pi x_1} \int_{-u_1-M}^{-u_1} \sin\left\{4\pi x_1 (u_1+u_2+M)\right\} \mathrm{d}u_2 \\
&\qquad - \frac{1}{4\pi x_1} \int_{-u_1}^{-u_1+M} \sin\left\{4\pi x_1 (u_1+u_2-M)\right\} \Bigg] \mathrm{d}u_1 \\
&= \int \frac{1}{16\pi^2 x_1^2} \left\{2 - 2\cos\left(4\pi x_1 M\right)\right\} \mathrm{d}u_1 \\
&= M^2 \operatorname{sinc}^2 (2x_1 M) \int \mathrm{d}u_1 \sim \operatorname{sinc}^2\left(\frac{L\theta_\mathrm{s}}{\lambda f} x_1\right),
\end{aligned} \tag{A.1}$$

where $\int \mathrm{d}u_1$ is a constant because of the finite aperture of the system.

Appendix B

Wigner representation of shift variant/invariant systems

B.1 Shift invariant system

If the system is shift invariant, then the output field is computed by a convolution of the input field and the impulse response as

$$E_2(x_2) = \int E_1(x_1) h(x_2 - x_1) \mathrm{d}x_1. \tag{B.1}$$

Then, the WDF of the output field is computed as

$$\begin{aligned} \mathcal{W}_2(x_2, u_2) &= \int E_2(x_2 + \tfrac{\xi}{2}) E_2^*(x_2 - \tfrac{\xi}{2}) \mathrm{e}^{-j2\pi u_2 \xi} \mathrm{d}\xi \\ &= \int \left[\int E_1(x_1) h(x_2 + \tfrac{\xi}{2} - x_1) \mathrm{d}x_1 \right] \left[\int E_1^*(x_1') h^*(x_2 - \tfrac{\xi}{2} - x_1') \mathrm{d}x_1' \right] \mathrm{e}^{-i2\pi u_2 \xi} \mathrm{d}\xi \\ &= \iint \left[\int h(x_2 + \tfrac{\xi}{2} - x_1) h^*(x_2 - \tfrac{\xi}{2} - x_1') \mathrm{e}^{-i2\pi u_2 \xi} \mathrm{d}\xi \right] E_1(x_1) E_1^*(x_1') \mathrm{d}x_1 \mathrm{d}x_1', \end{aligned} \tag{B.2}$$

where ξ is a dummy variable to compute the WDF, and x_1 and x_1' are dummy variables from eq. (B.1). By defining new variables as

$$x_1 = p + \frac{q}{2}, \quad \text{and} \tag{B.3}$$

$$x_1' = p - \frac{q}{2}, \tag{B.4}$$

x_1 and x_1' are substituted to p and q:

$$\begin{aligned}\mathcal{W}_2(x_2, u_2) &= \iint \left[\int h(x_2 + \tfrac{\xi}{2} - p - \tfrac{q}{2}) h^*(x_2 - \tfrac{\xi}{2} - p + \tfrac{q}{2}) \mathrm{e}^{-i2\pi u_2 \xi} \mathrm{d}\xi \right] \\ &\quad \times E_1(p + \tfrac{q}{2}) E_1^*(p - \tfrac{q}{2}) \mathrm{d}p \mathrm{d}q \\ &= \iint \left[\int h(x_2 - p + \tfrac{\xi+q}{2}) h^*(x_2 - p - \tfrac{\xi-q}{2}) \mathrm{e}^{-i2\pi u_2 \xi} \mathrm{d}\xi \right] E_1(p + \tfrac{q}{2}) E_1^*(p - \tfrac{q}{2}) \mathrm{d}p \mathrm{d}q \\ &= \iint \left[\int h(x_2 - p + \tfrac{\xi+q}{2}) h^*(x_2 - p - \tfrac{\xi-q}{2}) \mathrm{e}^{-i2\pi u_2 (\xi - q)} \mathrm{d}\xi \right] E_1(p+\tfrac{q}{2}) E_1^*(p-\tfrac{q}{2}) \mathrm{e}^{-i2\pi u_2 q} \mathrm{d}p \mathrm{d}q.\end{aligned} \tag{B.5}$$

In the first integration, ξ is integrated from $-\infty$ to ∞ for a given q in the third integral. A new variable $t = \xi - q$ is used, where the integration with respect to t is still from $-\infty$ to ∞. Then, eq. (B.5) is simplified as

$$\begin{aligned}\mathcal{W}_2(x_2, u_2) = \iint & E_1(p + \tfrac{q}{2}) E_1^*(p - \tfrac{q}{2}) \mathrm{e}^{-i2\pi u_2 q} \mathrm{d}p \mathrm{d}q \\ & \left[\int h(x_2 - p + \tfrac{t}{2}) h^*(x_2 - p - \tfrac{t}{2}) \mathrm{e}^{-i2\pi u_2 t} \mathrm{d}t \right] \\ & = \iint K_{\mathrm{si}}(x_2 - p) E_1(p + \tfrac{q}{2}) E_1^*(p - \tfrac{q}{2}) \mathrm{e}^{-i2\pi u_2 q} \mathrm{d}p \mathrm{d}q,\end{aligned} \tag{B.6}$$

where

$$K_{\mathrm{si}}(x_2 - p, u_2) = \int h(x_2 - p + \tfrac{t}{2}) h^*(x_2 - p - \tfrac{t}{2}) \mathrm{e}^{-i2\pi u_2 t} \mathrm{d}t. \tag{B.7}$$

Note that K_{si} is the WDF of the impulse response. Since one integral is the WDF of the input field, we obtain

$$\begin{aligned}\mathcal{W}_2(x_2, u_2) &= \int K_{\mathrm{si}}(x_2 - p) \left[\int E_1(p + \tfrac{q}{2}) E_1^*(p - \tfrac{q}{2}) \mathrm{e}^{-i2\pi u_2 q} \mathrm{d}q \right] \mathrm{d}p, \\ &= \int K_{\mathrm{si}}(x_2 - p, u_2) \mathcal{W}_1(p, u_2) \mathrm{d}p. \quad \text{(B.8)}\end{aligned}$$

Since p is dummy variable, replacing p with x_1 leads to the final equation.

$$\mathcal{W}_2(x_2, u_2) = \int K_{\mathrm{si}}(x_2 - x_1, u_2) \mathcal{W}_1(x_1, u_2) \mathrm{d}x_1. \quad \text{(B.9)}$$

B.2 Shift variant system

For a shift variant system, the input and output are represented as integrals with a shift variant impulse response as

$$E_2(x_2) = \int E_1(x_1) h(x_2; x_1) \mathrm{d}x_1. \quad \text{(B.10)}$$

Applying the definition of the WDF to the output field and substituting x_1 and x_1' into p and q gives

$$\begin{aligned}\mathcal{W}_2(x_2, u_2) &= \int E_2(x_2 + \tfrac{\xi}{2}) E_2^*(x_2 - \tfrac{\xi}{2}) \mathrm{e}^{-i2\pi u_2 \xi} \mathrm{d}\xi \\ &= \int \left[\int E_1(x_1) h(x_2 + \tfrac{\xi}{2}; x_1) \mathrm{d}x_1 \right] \left[\int E_1(x_1') h(x_2 - \tfrac{\xi}{2}; x_1') \mathrm{d}x_1' \right] \mathrm{e}^{-i2\pi u_2 \xi} \mathrm{d}\xi \\ &= \iint \left[\int h(x_2 + \tfrac{\xi}{2}; p + \tfrac{q}{2}) h^*(x_2 - \tfrac{\xi}{2}; p - \tfrac{q}{2}) \mathrm{e}^{-i2\pi u_2 \xi} \mathrm{d}\xi \right] E_1(p + \tfrac{q}{2}) E_1^*(p - \tfrac{q}{2}) \mathrm{d}p \mathrm{d}q.\end{aligned} \quad \text{(B.11)}$$

Since $h(x_2; x_1)$ is a function of two input arguments, the double Wigner distribution function of the impulse response [86] is defined as

$$K_{\mathrm{sv}}(x_2, u_2; x_1, u_1) = \iint h(x_2 + \tfrac{\xi}{2}; x_1 + \tfrac{\eta}{2}) h^*(x_2 - \tfrac{\xi}{2}; x_1 - \tfrac{\eta}{2}) \mathrm{e}^{-i2\pi(u_2 \xi - u_1 \eta)} \mathrm{d}\xi \mathrm{d}\eta, \quad \text{(B.12)}$$

and equivalently we have

$$\int h(x_2+\tfrac{\xi}{2};p+\tfrac{q}{2})h^*(x_2-\tfrac{\xi}{2};p-\tfrac{q}{2})\mathrm{e}^{-i2\pi u_2\xi}\mathrm{d}\xi \\ =\int K_{\mathrm{sv}}(x_2,u_2;p,u_1)\mathrm{e}^{-i2\pi u_1 q}\mathrm{d}u_1. \quad \text{(B.13)}$$

Note that the inverse Fourier transform with respect to η in eq. (B.12) moves to the right hand side in eq. (B.13). Substituting eq. (B.13) into eq. (B.11), we finally have

$$\begin{aligned}\mathcal{W}_2(x_2,u_2) &= \iint\left[\int K_{\mathrm{sv}}(x_2,u_2;p,u_1)\mathrm{e}^{-i2\pi u_1 q}\mathrm{d}u_1\right]E_1(p+\tfrac{q}{2})E_1^*(p-\tfrac{q}{2})\mathrm{d}p\mathrm{d}q \\ &= \iint K_{\mathrm{sv}}(x_2,u_2;p,u_1)\left[\int E_1(p+\tfrac{q}{2})E_1^*(p-\tfrac{q}{2})\mathrm{e}^{-i2\pi u_1 q}\mathrm{d}q\right]\mathrm{d}u_1\mathrm{d}p \\ &= \iint K_{\mathrm{sv}}(x_2,u_2;p,u_1)\mathcal{W}_1(p,u_1)\mathrm{d}p\mathrm{d}u_1. \quad \text{(B.14)}\end{aligned}$$

Replacing the dummy variable p with x_1 leads to the final equation.

$$\mathcal{W}_2(x_2,u_2)=\iint K_{\mathrm{sv}}(x_2,u_2;x_1,u_1)\mathcal{W}_1(x_1,u_1)\mathrm{d}x_1\mathrm{d}u_1. \quad \text{(B.15)}$$

Bibliography

[1] W. Thomas Cathey and Edward R. Dowski. New paradigm for imaging systems. *Applied Optics*, 41(29):6080–6092, 2002.

[2] Ramesh Raskar and Jack Tumblin. *Computational Photography.* A K Peters, 2008.

[3] Berthold Horn. Computational Imaging. *MIT EECS 6.881 lecture note*, 2006.

[4] D. J. Brady. Computational imaging. *IMA Tuturial on optical imaging*, 2005.

[5] Joseph W. Goodman. *Introduction to Fourier optics.* Roberts & Co., Englewood, Colo., 3rd edition, 2005.

[6] R. R. A. Syms. *Practical volume holography.* Oxford engineering science series ; 24. Oxford University Press, Oxford, 1990.

[7] A. Sinha, W. Y. Sun, T. Shih, and G. Barbastathis. Volume holographic imaging in transmission geometry. *Applied Optics*, 43(7):1533–1551, 2004.

[8] H. Coufal, Demetri Psaltis, and Glenn T. Sincerbox. *Holographic data storage.* Springer, Berlin, 2000.

[9] E. N. Leith, A. Kozma, J. Upatnieks, J. Marks, and N. Massey. Holographic data storage in three-dimensional media. *Applied Optics*, 5:1303–1311, 1966.

[10] J. F. Heanue, M. C. Bashaw, and L Hesselink. Volume hologrpahic storage and retrieval of digital data. *Science*, 265:749–752, 1994.

[11] D. Psaltis and F. Mok. Holographic Memories. *Scientific American*, 273(5):70–76, 1995.

[12] H. Lee, X. G. Gu, and D. Psaltis. Volume Holographic Interconnections with Maximal Capacity and Minimal Cross Talk. *Journal of Applied Physics*, 65(6):2191–2194, 1989.

[13] D. Psaltis, D. Brady, X. G. Gu, and S. Lin. Holography in Artificial Neural Networks. *Nature*, 343(6256):325–330, 1990.

[14] George Barbastathis and Demetri Psaltis. Volume Holographic Multiplexing Methods. In Hans J. Coufal, Demetri Psaltis, and Glenn T. Sincerbox, editors, *Holographic Data Storage*, volume 76 of *Springer Series in Optical Sciences*, pages xxvi, 486. Springer, 1 edition, 2000.

[15] G. Barbastathis, M. Balberg, and D. J. Brady. Confocal microscopy with a volume holographic filter. *Optics Letters*, 24(12):811–813, 1999.

[16] W. H. Liu, G. Barbastathis, and D. Psaltis. Volume holographic hyperspectral imaging. *Applied Optics*, 43(18):3581–3599, 2004.

[17] W. H. Liu, D. Psaltis, and G. Barbastathis. Real-time spectral imaging in three spatial dimensions. *Optics Letters*, 27(10):854–856, 2002.

[18] A. Sinha and G. Barbastathis. Broadband volume holographic imaging. *Applied Optics*, 43(27):5214–5221, 2004.

[19] A. Sinha, G. Barbastathis, W. H. Liu, and D. Psaltis. Imaging using volume holograms. *Optical Engineering*, 43(9):1959–1972, 2004.

[20] A. Sinha and G. Barbastathis. Volume holographic imaging for surface metrology at long working distances. *Optics Express*, 11(24):3202–3209, 2003.

[21] A. Sinha and G. Barbastathis. N-ocular volume holographic imaging. *Applied Optics*, 43(31):5784–5795, 2004.

[22] A. Sinha and G. Barbastathis. Volume holographic telescope. *Optics Letters*, 27(19):1690–1692, 2002.

[23] Wenyang Sun, Kehan Tian, and George Barbastathis. Hyper-Spectral Imaging with Volume Holograpahic Lenses. In *Conference on Lasers and Electro-Optics (CLEO)*, volume CFP2, Baltimore, Maryland, 2005.

[24] W. Sun and G. Barbastathis. Rainbow volume holographic imaging. *Optics Letters*, 30(9):976–978, 2005.

[25] Yuan Luo, P. J. Gelsinger-Austin, J. M. Watson, G. Barbastathis, J. K. Barton, and R. K. Kostuk. Laser induced fluorescence imaging of sub-surface tissue structures with a volume holographic spatial-spectral imaging system. *Optics Letters*, 33(18):2098–2100, 2008.

[26] George Barbastathis. Imaging Properties of Three-Dimensional Pupils. In *Computational Optical Sensing and Imaging (COSI)*, volume paper CMC4, page paper CMC4, Charlotte, North Carolina, 2005. Optical Society of America.

[27] George Barbastathis. The transfer funciton of volume hologrpahic optical systems. In Jean Pierre Huignard Peter Gnter, editor, *Photorefractive Materials and Their Applications*, volume 3 of *Springer Series in Optical Science*. Springer-Verlag, 2006.

[28] Charles Kittel. *Introduction to solid state physics*. Wiley, Hoboken, NJ, 8th edition, 2005.

[29] Raymond K. Kostuk. *Multiple grating reflection volume holograms with application to optical interconnects*. Ph. D. Thesis, Stanford University, 1986.

[30] R. R. A. Syms and L. Solymar. Analysis of Volume Holographic Cylindrical Lenses. *Journal of the Optical Society of America*, 72(2):179–186, 1982.

[31] Francis A. Jenkins and Harvey Elliott White. *Fundamentals of optics*. McGraw-Hill, New York, 4th edition, 1976.

[32] P. Wissmann, S. B. Oh, and G. Barbastathis. Simulation and optimization of volume holographic imaging systems in Zemax (R). *Optics Express*, 16(10):7516–7524, 2008.

[33] Jurgen R. Meyer-Arendt. *Introduction to classical and modern optics.* Prentice Hall, Englewood Cliffs, N.J., 4th edition, 1995.

[34] O. Momtahan, C. R. Hsieh, A. Karbaschi, A. Adibi, M. E. Sullivan, and D. J. Brady. Spherical beam volume holograms for spectroscopic applications: modeling and implementation. *Applied Optics*, 43(36):6557–6567, 2004.

[35] O. Momtahan, C. R. Hsieh, A. Adibi, and D. J. Brady. Analysis of slitless holographic spectrometers implemented by spherical beam volume holograms. *Applied Optics*, 45(13):2955–2964, 2006.

[36] Jonathan M. Watson. *Evaluation of Spatial-Spectral Filtering in Non-Paraxial Volume Holographic Imaging Systems.* M.S. Thesis, Massachusetts Institute of Technology, 2008.

[37] Max Born and Emil Wolf. *Principles of optics : electromagnetic theory of propagation, interference and diffraction of light.* Cambridge University Press, Cambridge [England], New York, 7th (expanded) edition, 1999.

[38] Patrick Wissmann. *Simulation and Optimization of Active and Passive Holographic Imaging Systems for Shape and Surface Metrology.* Diploma Thesis, RWTH Aachen University, 2007.

[39] H. Kogelnik. Coupled wave theory for thick hologram gratings. *Bell. Syst. Tech. J.*, 48:2909–2947, 1969.

[40] Joseph W. Goodman. *Statistical Optics.* John Wiley and Sons, Inc., 2000.

[41] Brian Curless. Overview of Active Vision Techniques. In *SIGGRAPH 99*, Course on 3D Photography, 1999.

[42] Arthur P. Cracknell and Ladson Hayes. *Introduction to Remote Sensing*. Taylor and Francis, London, 2007.

[43] Colin J. R. Sheppard and David M. Shotton. *Confocal laser scanning microscopy*. Springer, Oxford, 1997.

[44] Berthold Horn. *Robot vision*. MIT electrical engineering and computer science series. MIT Press, Cambridge, 1986.

[45] J. Y. Bouguet and P. Perona. 3D photography using shadows in dual-space geometry. *International Journal of Computer Vision*, 35(2):129–149, 1999.

[46] D. Marr and T. Poggio. A Theory of Human Stereo Vision. Technical Report 451, MIT, 1977.

[47] Neel Joshi, Wojciech Matusik, and Shai Avidan. Natural Video Matting using Camera Arrays. In *SIGGRAPH*, volume 25 (3) of *ACM Transactions on Graphics*, 2006.

[48] J. Ens and P. Lawrence. An investigation of methods for determining depth from focus. In *IEEE Transactions on Pattern Analysis and Machine Intelligence*, volume 15, pages 97–108, 1993.

[49] Subhasis Chaudhuri and A.N. Rajagopalan. *Depth from Defocus: A Real Aperture Imaging Approach*. Springer, 1999.

[50] Edward R. Dowski and W. Thomas Cathey. Single-lens single-image incoherent passive-ranging systems. *Applied Optics*, 33(29):6762–6773, 1994.

[51] G. Barbastathis and D. J. Brady. Multidimensional tomographic imaging using volume holography. *Proceedings of the Ieee*, 87(12):2098–2120, 1999.

[52] J. Rosen and A. Yariv. Three-dimensional imaging of random radiation sources. *Optics Letters*, 21(14):1011–1013, 1996.

[53] J. Rosen and A. Yariv. General theorem of spatial coherence: Application to three-dimensional imaging. *Journal of the Optical Society of America A*, 13(10):2091–2095, 1996.

[54] J. Rosen and A. Yariv. Reconstruction of longitudinal distributed incoherent sources. *Optics Letters*, 21(22):1803–1805, 1996.

[55] D. L. Marks, R. A. Stack, and D. J. Brady. Three-dimensional coherence imaging in the Fresnel domain. *Applied Optics*, 38(8):1332–1342, 1999.

[56] H. Arimoto, K. Yoshimori, and K. Itoh. Retrieval of the cross-spectral density propagating in free space. *Journal of the Optical Society of America A*, 16(10):2447–2452, 1999.

[57] P H Van Cittert. Die wahrscheinliche Schwingungsverteilung in einer von einer Lichtquelle direkt oder mittels einer Linse beleuchteten Ebene. *Physica*, 1:201–210, 1934.

[58] Frederik Zernike. The concept of degree of coherence and its applications to optical problems. *Physica*, 5:785–795, 1938.

[59] Daniel Lawrence Marks. *Four-dimensional coherence sensing.* Ph.D. Thesis, University of Illinois at Urbana-Champaign, 2001.

[60] Alvy Ray Smith and James F. Blinn. Blue screen matting. In *International Conference on Computer Graphics and Interactive Techniques*, Proceedings of the 23rd annual conference on Computer graphics and interactive techniques, pages 259–268, 1996.

[61] P. Vlahos. Comprehensive Electronic Compositing System. U. S. Patent 4,344,085, 1982.

[62] P. Vlahos. Encoded Signal Color Image Compositing. U. S. Patent 4,409,611, 1983.

[63] P. Vlahos, P. Vlahos, and D. F. Fellinger. Automated encoded signal color image compositing . U. S. Patent 4,589,013, 1986.

[64] P Vlahos. Comprehensive Electronic Compositing System. U. S. Patent 4,625,231, 1986.

[65] B. J. Thompson and R. Sudol. Finite-aperture effects in the measurement of the degree of coherence. *Journal of the Optical Society of America A*, 1(6):598–604, 1984.

[66] A. S. Marathay and D. B. Pollock. Young's interferencce fringes with finite-sized sampling apertures. *Journal of the Optical Society of America A*, 1(10):1057–1059, 1984.

[67] James O. Berger. *Statistical decision theory and Bayesian analysis.* Springer series in statistics. Springer-Verlag, New York, 2nd edition, 1985.

[68] Leonard Mandel and Emil Wolf. *Optical coherence and quantum optics.* Cambridge University Press, Cambridge [England] ; New York, NY, USA, 1995.

[69] E. Wolf and W. H. Carter. Angular-Distribution of Radiant Intensity from Sources of Different Degrees of Spatial Coherence. *Optics Communications*, 13(3):205–209, 1975.

[70] E. Wolf and W. H. Carter. Radiometric Generalization of Van Cittert-Zernike Theorem for Fields Generated by Sources of Arbitrary State of Coherence. *Optics Communications*, 16(3):297–302, 1976.

[71] L. Mandel and E. Wolf. Spectral Coherence and Concept of Cross-Spectral Purity. *Journal of the Optical Society of America*, 66(6):529–535, 1976.

[72] M. J. Bastiaans. Frequency-Domain Treatment of Partial Coherence. *Optica Acta*, 24(3):261–274, 1977.

[73] Vidi Saptari. *Fourier transform spectroscopy instrumentation engineering.* SPIE Optical Engineering Press, Bellingham, WA, 2004.

[74] Eugene Hecht. *Optics*. Addison-Wesley, Reading, Mass., 4th edition, 2002.

[75] Eugene Wigner. On the quantum correction for thermodynamic equilibrium. *Physics Review*, 40:749–759, 1932.

[76] Martin J. Bastiaans. Application of the Wigner distribution function in optics. In W. Mecklenbruker; F. Hlawatsch, editor, *The Wigner Distribution - Theory and Applications in Signal Processing*, pages 375–426. Elsevier Science, Amsterdam, 1997.

[77] Walter D. Furlan, Manuel Martnez-Corral, Bahram Javidi, and Genaro Saavedra. Analysis of 3-D Integral Imaging Displays Using the Wigner Distribution. *Journal of Display Technology*, 2(2):180–185, 2006.

[78] Q. G. Yang, L. R. Liu, J. F. Sun, Y. J. Zhu, and W. Lu. Analysis of optical systems with extended depth of field using the Wigner distribution function. *Applied Optics*, 45(34):8586–8595, 2006.

[79] M. J. Bastiaans. Application of the Wigner Distribution Function to Partially Coherent-Light. *Journal of the Optical Society of America A*, 3(8):1227–1238, 1986.

[80] J. Maycock, C. P. McElhinney, B. M. Hennelly, T. J. Naughton, J. B. McDonald, and B. Javidi. Reconstruction of partially occluded objects encoded in three-dimensional scenes by using digital holograms. *Applied Optics*, 45(13):2975–2985, 2006.

[81] A. Stern and B. Javidi. Sampling in the light of Wigner distribution. *Journal of the Optical Society of America A*, 21(3):360–366, 2004.

[82] K. B. Wolf, D. Mendlovic, and Z. Zalevsky. Generalized Wigner function for the analysis of superresolution systems. *Applied Optics*, 37(20):4374–4379, 1998.

[83] M. J. Bastiaans. Wigner Distribution Function and Its Application to 1st-order Optics. *Journal of the Optical Society of America*, 69(12):1710–1716, 1979.

[84] M. J. Bastiaans and P. G. J. van de Mortel. Wigner distribution function of a circular aperture. *Journal of the Optical Society of America A*, 13(8):1698–1703, 1996.

[85] V. Arrizón and J. Ojeda-castañeda. Irradiance at Fresnel Planes of a Phase Grating. *Journal of the Optical Society of America A*, 9(10):1801–1806, 1992.

[86] Weiqing Pan. Double Wigner distribution function of a first-order optical system with a hard-edge aperture. *Applied Optics*, 47(1):45–51, 2008.

[87] A. Stein and G. Barbastathis. Axial imaging necessitates loss of lateral shift invariance. *Applied Optics*, 41(29):6055–6061, 2002.

[88] Anat Levin, William T. Freeman, and Frédo Durand. Understanding camera trade-offs through a Bayesian analysis of light field projections. Technical Report MIT-CSAIL-TR-2008-049, Massachusetts Institute of Technology, 2008.

[89] E. H. Adelson and J. Y. A. Wang. Single lens stereo with a plenoptic camera. *IEEE Transactions on Pattern Analysis and Machine Intelligence*, 14:99–106, 1992.

[90] Ren Ng, Marc Levoy, Mathieu Bredif, Gene Duval, Mark Horowitz, and Pat Hanrahan. Light Field Photography with a Hand-held Plenoptic Camera. Technical report, Standford University, 2005.

[91] Anat Levin, Rob Fergus, Frédo Durand, and William T. Freeman. Image and depth from a conventional camera with a coded aperture. *SIGGRAPH*, 2007.

[92] A. Veeraraghavan, Ramesh Raskar, A. Agrawal, A. Mohan, and J. Tumblin. Dappled photography: Mask-enhanced cameras for heterodyned light fields and coded aperture refocusing. *SIGGRAPH*, 2007.

[93] E. R. Dowski and W. T. Cathey. Extended Depth of Field through Wave-Front Coding. *Applied Optics*, 34(11):1859–1866, 1995.

[94] Kjell J. Gåvik. *Optical metrology.* J. Wiley & Sons, West Sussex, Eng. ; Hoboken, N.J., 3rd edition, 2002.